

The *Gaia* Ultracool Dwarf Sample – VI. Spectral Types and Properties of 51 Ultracool Dwarfs

Gemma Cheng,^{1*} H.R.A. Jones,¹ R.L. Smart,^{1,2} Federico Marocco,³ W.J. Cooper,^{1,2} Adam Burgasser,⁴ Juan Carlos Beamin,⁵ D.J. Pinfield,¹ Jonathan Gagné,^{6,7} and Leslie Moranta^{6,7,8}

¹*School of Physics, Astronomy and Mathematics, University of Hertfordshire, College Lane, Hatfield AL10 9AB, UK*

²*Istituto Nazionale di Astrofisica, Osservatorio Astrofisico di Torino, Strada Osservatorio 20, I-10025 Pino Torinese, Italy*

³*IPAC, Mail Code 100-22, Caltech, 1200 E. California Blvd., Pasadena, CA 91125, USA*

⁴*Department of Astronomy & Astrophysics, UC San Diego, 9500 Gilman Drive, La Jolla, CA 92093*

⁵*Fundación Chilena de Astronomía, El Vergel 2252, Santiago, Chile*

⁶*Planétarium Rio Tinto Alcan, Espace pour la Vie, 4801 av. Pierre-de Coubertin, Montréal, Québec, Canada*

⁷*Institute for Research on Exoplanets, Université de Montréal, Département de Physique, C.P. 6128 Succ. Centre-ville, Montréal, QC H3C 3J7, Canada*

⁸*Department of Astrophysics, American Museum of Natural History, Central Park West at 79th St, New York, NY 10024, USA*

Accepted XXX. Received YYY; in original form ZZZ

ABSTRACT

Near-infrared spectra from the IRTF/SpeX and Blanco/ARCoIRIS telescope/instrument combinations are used for spectroscopic classification, to measure radial velocities and for the inference of astrophysical properties of 51 *Gaia*-selected nearby ultracool dwarfs. In this sample, 44 are newly classified in the near infrared. All but one of the UCDs are within 100 pc, and 37 lie within 50 pc. We find a total of 26 M-types, 24 L-types and one T-type in our sample. The positions of the majority of the UCDs on colour-magnitude diagrams and with evolutionary cooling track plots indicate that they are largely old and stellar in nature. There are a few UCDs of particular interest which lie away from expected trends, highlighting potential young, binary and thick disc/subdwarf UCDs. From spectral and kinematic analyses, we identify UCDs of particular interest for further investigation, including seven potentially young UCDs, three thick disc UCDs, one subdwarf, six wide binaries, and six unresolved binaries.

Key words: brown dwarfs – stars: late-type – stars: low mass

1 INTRODUCTION

The *Gaia* third data release (hereafter DR3; [Gaia Collaboration et al. \(2022\)](#)) was released on 13 June 2022, and contains five-parameter astrometric solutions for over 1.46 billion (1.46×10^9) sources. Ultracool dwarfs (hereafter UCDs) are defined as having spectral types of M7 or later ([Kirkpatrick et al. 1997](#)). UCDs therefore straddle the boundary between stars and sub-stellar objects – by studying such objects, we can learn more about the characteristics of, and physical processes in, UCDs.

The *Gaia* Ultracool Dwarf Sample (hereafter GUCDS) was introduced by [Smart et al. \(2017\)](#). The current GUCDS contains more than 8800 UCDs which have spectroscopic spectral type classifications and their associated photometric data from a number of infrared and optical surveys. Previous papers in this series have explored the known UCDs in the *Gaia* data releases ([Smart et al. 2017](#)); improved upon main sequence modelling for UCDs ([Smart et al. 2019](#)); identified new benchmark binary systems containing *Gaia*-detected UCDs ([Marocco et al. 2020](#)); used GTC/OSIRIS optical spectra to determine astrophysical properties of 53 UCDs ([Cooper et al. 2024](#)), and collated a catalogue of 278 multiple

systems in the GUCDS with at least one spectroscopically confirmed UCD ([Baig et al. 2024](#)).

Near-infrared (hereafter NIR) spectra are a valuable tool to determine the characteristics of UCDs, since they typically provide much better signal-to-noise ratio than optical observations due to the low temperatures and luminosities of UCDs ([Patience et al. 2012](#)). In particular, NIR spectroscopy allows for the spectral type classification of UCDs, since many of the defining characteristics of L and T-dwarfs are features in their NIR spectra (e.g. methane in the *J*-band of T-dwarfs; see [McLean et al. 2001](#); [Burgasser et al. 2002](#); [Geballe et al. 2002](#); [Kirkpatrick 2005](#) among others).

This work targets UCDs in the GUCDS which have only photometrically determined spectral types, obtaining spectroscopic classifications and further investigating UCDs which have unusual characteristics. Although *Gaia* DR3 contains BP and RP low-resolution spectra, the faint and red nature of UCDs means that BP spectra are only of use for the brightest and hottest UCDs. [Sarro et al. \(2023\)](#) outline the difficulties in using RP spectra for UCD characterisation – primarily these difficulties are the fairly bright *Gaia* *G*-band limit of 15 mag and the low resolution of the instrument results in spectral features which are blended and merged.

This paper is presented as follows: Section 2 outlines the candidate selection and spectral observations used for this work.

* E-mail: g.j.cheng@herts.ac.uk

Section 3 presents the spectral type classification methods used for the UCDs in this work. Properties of the UCDs are derived from their spectra in Section 4, and further properties of the sample are derived in Sections 5–8. UCDs of potential interest (such as young UCDs and subdwarfs) are identified in Section 9. Finally, Section 10 investigates these UCDs in further detail, and the conclusions of this work are presented in Section 11.

2 DATA COLLECTION AND REDUCTION

2.1 Candidate Selection

The UCDs selected for this investigation were initially found using *Gaia* DR1 and DR2. The selection criteria were determined empirically from known UCDs and exploited the following external photometric datasets:

- Panoramic Survey Telescope and Rapid Response System i , z and y magnitudes (hereafter Pan-STARRS; Chambers et al. 2016).
- Two Micron All Sky Survey J , H and K_s magnitudes (hereafter 2MASS; Skrutskie et al. 2006).
- AllWISE or CatWISE2020 $W1$ and $W2$ magnitudes, depending on availability at time of candidate selection (AllWISE is a combination of *Wide-field Infrared Survey Explorer*, hereafter WISE, and NEOWISE data; Wright et al. 2010; Mainzer et al. 2011; and CatWISE2020 expands the baseline to six years, improving accuracy and precision; Marocco et al. 2021).

The selection process was conservative enough to retain all real UCDs, but also results in a number of false positives. To remove false positives, each target was visually checked in different sky surveys for inconsistencies, e.g. colour, proper motion, crowding.

The *Gaia* data releases within 100 pc have significant numbers of objects with incorrect parallaxes (e.g. for DR3; Lindegren et al. 2018; Smart et al. 2019), and many of the UCDs in this sample are faint, thus quality assurance flags are not used since they are unreliable. The final selection criteria for the UCDs in the GUCDS selection therefore do not rely solely on absolute G -band magnitude and instead use estimated spectral types and colour relations. In order to estimate the spectral types, we used known literature UCDs to find relations between median absolute G magnitude and various colour relations.

The adopted selection criteria are:

- No published spectroscopic spectral classification.
- Has parallax, G , G_{RP} and at least one 2MASS magnitude.
- M_G -based spectral type later than M6 (nearest subclass rounded to 0.5).
- Median colour-derived spectral type later than M6 (median of nearest subclasses for available colours).

Table 1 contains *Gaia* DR3 data for the UCDs, including their G - and J -band magnitudes and parallaxes. The *Gaia* source ID for each UCD is cross-referenced with SIMBAD (Wenger et al. 2000), in order to find any published classifications for the UCDs.

Many of the sources of interest have SIMBAD entries, and we included some additional sources with spectroscopic spectral type classifications (Table 2; Wenger et al. 2000). This is useful for the purposes of this paper, since we can check that our derived spectral types are consistent with those published, and thus we can gauge the reliability of our spectral type classifications. We included these UCDs with literature spectral types (such as J0817–6155) to use as comparison objects. We also included J1243+6001 in our sample – although this UCD does not have a published *Gaia* parallax, Faherty

et al. (2021) ascertain it is in a wide binary system with BD+60 1417. We therefore adopt the parallax of the primary for the UCD.

2.2 Observations of UCDs

The UCDs selected for investigation in this work were observed with the Astronomy Research using the Cornell Infra Red Imaging Spectrograph instrument (hereafter ARCoIRIS; Schlawin et al. 2014) at the Blanco 4 m telescope in Chile and the SpeX instrument at the NASA Infrared Telescope Facility in Hawaii (hereafter IRTF; Rayner et al. 2003).

We used A-B-B-A observing patterns with both telescopes, so that sky subtraction could be carried out in order to optimise the signal from the UCDs. For most observations, the slit was aligned to the parallactic angle, in order to keep the effects of atmospheric distortion to a minimum. After each candidate observation, we observed a nearby A0V star to use for telluric corrections, taken from the Tycho-2 Catalogue (Høg et al. 2000). The standards used for telluric correction in the reduction process were cross-referenced with SIMBAD to check the spectral types used for the telluric correction of the spectral data. No uncertainties for the standards' spectral classifications are published, so an uncertainty of ± 1 subtype is applied – all of the telluric correction standard stars used in this work are within the uncertainties of an A0V-type. Appendix A contains the observation log, which also includes details of the standard stars used for the telluric corrections of each candidate.

During some of the observing runs, the conditions were too poor for UCDs to be observed (e.g. poor seeing or excessive cloud cover), so non-UCDs were observed instead. Appendix B discusses these UCDs, along with the objects that were observed and classified as non-UCDs.

2.2.1 Blanco Observations

We observed 13 UCDs in 2018 using the Blanco ARCoIRIS instrument under program 2018A-0910 (PI: Beamin). ARCoIRIS is composed of a cross-dispersed spectrograph, producing six spectral orders between the wavelengths of 0.8–2.4 μm (James et al. 2015). The instrument has a resolution of $R \approx 3000$, making the spectra obtained using ARCoIRIS the highest resolution spectra in our sample.

2.2.2 IRTF Observations

Between 2018 and 2021, 38 UCDs were observed using the IRTF SpeX instrument under programs 2018A067, 2020A069, 2020B057 and 2021A023 (PI: Smart), with a total of eight observations using the prism configuration and 30 observations using the short-wavelength cross-dispersion (hereafter SXD) configuration. The prism configuration creates one order of spectral data between the wavelengths of 0.70–2.52 μm , while the SXD grating covers spectral orders 3–9 between the wavelengths of 0.70–2.55 μm (Rayner et al. 2003). The resolutions of the prism and SXD configurations are $R \approx 200$ and $R \approx 2000$, respectively. Due to the low resolution of the prism, this configuration was only used when observing conditions were poor (e.g. clouds, wind).

2.3 Data Reduction with SPEXTOOL

The data reduction process was completed with the SPEXTOOL program (Cushing et al. 2004). The reduction process for the SpeX

Table 1. Entries for this table have been taken from the GUCDS input list and the *Gaia* archive. UCDS marked with a dagger † are those observed with SpeX Prism, those marked with a double dagger ‡ are observed with SpeX SXD, and those marked with an asterisk * are observed with ARCoIRIS. This data is also contained within the collated data table in Appendix D.

Object Short Name	RA (degrees)	Dec (degrees)	<i>Gaia</i> DR3 Source ID	2MASS <i>J</i> (mag)	<i>Gaia</i> DR3 <i>G</i> (mag)	Parallax (mas)	Absolute M_G (mag)
J0508+3319 ‡	77.2282625	33.3214494	181724125038647040	14.217 ± 0.032	19.141 ± 0.003	53.026 ± 0.461	17.763 ± 0.019
J0515+0613 ‡	78.7951672	6.2331569	3240769806581623296	15.649 ± 0.064	20.312 ± 0.005	15.631 ± 0.806	16.282 ± 0.112
J0526–5026 *	81.7491063	-50.4383390	4796425760263724800	15.412 ± 0.066	20.685 ± 0.011	37.920 ± 0.859	18.579 ± 0.050
J0542+0041 ‡	85.6038451	0.6838717	3219457457305021568	15.418 ± 0.056	20.627 ± 0.008	41.525 ± 1.041	18.718 ± 0.055
J0723+4622 ‡	110.8896758	46.3784540	974639306231785344	16.027 ± 0.083	20.695 ± 0.012	17.906 ± 1.575	16.959 ± 0.191
J0808+3157 ‡	122.0077516	31.950797	901922932930351872	12.722 ± 0.019	16.743 ± 0.001	38.819 ± 0.086	14.689 ± 0.005
J0811+1855 ‡	122.7928110	18.9243897	669399515262792320	14.478 ± 0.027	19.220 ± 0.003	33.589 ± 0.414	16.851 ± 0.027
J0817–6155 *	124.3735181	-61.9161302	5278042880077383040	13.613 ± 0.024	20.035 ± 0.007	191.836 ± 0.419	21.450 ± 0.008
J0832+3538 †	128.1977645	35.6477292	903765920576713856	12.522 ± 0.019	16.340 ± 0.001	32.328 ± 0.095	13.887 ± 0.006
J0850–0318 †	132.5371964	-3.3084429	5762038930728469888	14.247 ± 0.078	18.981 ± 0.002	28.433 ± 0.259	16.250 ± 0.020
J0900+5205 ‡	135.2161087	52.0862476	1017310351779243392	16.100 ± 0.108	20.817 ± 0.009	11.056 ± 1.126	16.035 ± 0.221
J0911+1432 ‡	137.9024998	14.5454833	606673098451745920	15.447 ± 0.048	20.339 ± 0.005	14.914 ± 0.767	16.207 ± 0.112
J0916–1121 ‡	139.2384596	-11.3519579	5739240415392701440	14.095 ± 0.029	18.726 ± 0.002	32.950 ± 0.250	16.315 ± 0.017
J0941+3315A ‡	145.3006199	33.2519852	794031395948224640	13.622 ± 0.029	17.968 ± 0.001	30.3279 ± 0.163	15.377 ± 0.012
J0942–2551 ‡	145.6348537	-25.8604361	5658599213249509120	15.860 ± 0.080	20.711 ± 0.008	20.006 ± 1.151	17.217 ± 0.125
J0948+5300 ‡	147.0526299	53.0102651	1020273539910037504	15.585 ± 0.064	20.465 ± 0.006	21.192 ± 0.798	17.096 ± 0.082
J1036–3441 *	159.2208579	-34.6960172	5444217638657849856	15.622 ± 0.048	20.850 ± 0.011	67.961 ± 1.595	20.012 ± 0.052
J1048–5254 *	162.1143606	-52.9048224	5353652721316104832	14.016 ± 0.030	18.887 ± 0.002	36.391 ± 0.183	16.692 ± 0.011
J1126–2706 ‡	171.6545247	-27.1126095	3533077004345702656	14.253 ± 0.028	18.924 ± 0.002	30.016 ± 0.273	16.311 ± 0.020
J1143+5324 †	175.8371376	53.4118116	840382713073253760	15.928 ± 0.075	20.620 ± 0.006	17.858 ± 0.772	16.879 ± 0.094
J1150–2914 ‡	177.6785418	-29.2469265	3480771277705948928	15.040 ± 0.042	19.955 ± 0.004	23.338 ± 0.450	16.795 ± 0.042
J1152+5901 ‡	178.2461013	59.0185278	846350351086394752	15.886 ± 0.070	20.637 ± 0.008	18.609 ± 0.750	16.985 ± 0.088
J1158–0008 *	179.6297159	-0.1476202	3795026681770171264	16.149 ± 0.079	20.711 ± 0.009	13.644 ± 1.405	16.386 ± 0.224
J1158+3817 ‡	179.5707516	38.2877118	4034251549793554176	14.657 ± 0.035	18.930 ± 0.003	21.719 ± 0.241	15.614 ± 0.024
J1212+0206 *	183.1413863	2.1072730	3699683699198329600	16.128 ± 0.128	20.715 ± 0.011	17.303 ± 1.668	16.906 ± 0.210
J1215+0042 *	183.8261119	0.7156115	3698542165611096064	15.533 ± 0.073	20.486 ± 0.011	22.557 ± 1.135	17.252 ± 0.110
J1243+6001 †	190.8838648	60.0239567	–	18.37 ± 0.22 ^a	>23.233	–	–
J1250+0455 ‡	192.5644993	4.9186159	3705763723623660416	15.158 ± 0.060	20.460 ± 0.007	13.938 ± 1.140	16.181 ± 0.178
J1252+0347 *	193.1586252	3.7929674	3704616555037021056	15.988 ± 0.081	20.709 ± 0.008	14.864 ± 1.427	16.570 ± 0.209
J1307+0246 *	196.8911778	2.7666348	3692416064777472640	15.051 ± 0.037	19.720 ± 0.018	23.888 ± 0.569	16.611 ± 0.055
J1313+1404 ‡	198.4447057	14.0825798	3743732776411929472	15.793 ± 0.071	20.384 ± 0.006	16.186 ± 0.854	16.430 ± 0.115
J1315+3232 ‡	198.8293776	32.5338098	1466650487416101504	12.949 ± 0.023	16.912 ± 0.001	33.523 ± 0.098	14.539 ± 0.006
J1320+4238 ‡	200.1293042	42.6378205	1525546995989465344	12.839 ± 0.025	16.695 ± 0.001	37.454 ± 0.064	14.562 ± 0.004
J1420+3235 ‡	215.1086971	32.5981565	1477880589944207744	13.824 ± 0.026	17.774 ± 0.001	21.907 ± 0.141	14.477 ± 0.014
J1423+5146 ‡	215.7633280	51.7760046	1604901876901703168	11.885 ± 0.021	15.867 ± 0.001	57.802 ± 0.059	14.676 ± 0.002
J1441+4217 ‡	220.4522858	42.2970197	1490058849451967744	15.722 ± 0.061	20.439 ± 0.006	22.053 ± 0.626	17.156 ± 0.062
J1452+0931 *	223.0056374	9.5260993	1174086386182157696	15.418 ± 0.070	20.114 ± 0.006	20.382 ± 0.668	16.660 ± 0.071
J1514+3547 ‡	228.7368646	35.7961237	1291186058168054016	16.097 ± 0.073	20.742 ± 0.008	18.902 ± 1.046	17.125 ± 0.120
J1536+0646 *	234.2473725	6.7803897	4430701697214030464	15.609 ± 0.066	20.669 ± 0.009	16.451 ± 1.214	16.749 ± 0.161
J1544–0435 †	236.1769024	-4.5919062	440227488928322944	15.901 ± 0.081	20.806 ± 0.008	19.245 ± 1.504	17.227 ± 0.170
J1544+3301 ‡	236.2299864	33.0294671	1370790111609798144	15.548 ± 0.057	20.653 ± 0.007	41.756 ± 0.775	18.756 ± 0.041
J1628–4652 *	247.1506423	-46.8816276	5942058396163925376	15.490 ± 0.011	20.132 ± 0.007	16.086 ± 1.035	24.100 ± 0.140
J1637+1813 †	249.4715498	18.2284064	4562510841912952192	15.461 ± 0.049	20.312 ± 0.005	20.092 ± 0.698	23.797 ± 0.076
J1646–2115 †	251.5970487	-21.2533460	4126955670100614400	15.633 ± 0.064	20.698 ± 0.008	21.184 ± 1.858	24.068 ± 0.191
J1654–3819 ‡	253.5650997	-38.3184147	5970493789759784192	12.084 ± 0.026	15.956 ± 0.001	39.666 ± 0.060	17.964 ± 0.003
J1700–4048 *	255.2221268	-40.8051656	5966993223906484992	16.252 ± 0.112	20.579 ± 0.010	4.397 ± 1.316	27.378 ± 0.650
J1713–3952 ‡	258.4192905	-39.8712362	5972124644679705728	13.401 ± 0.026	18.133 ± 0.002	51.561 ± 0.178	19.571 ± 0.008
J1737+4705 ‡	264.4109622	47.0951605	1363482108789712000	14.572 ± 0.029	19.237 ± 0.003	26.803 ± 0.208	22.096 ± 0.017
J1847–3419 ‡	281.9459895	-34.3260745	6735308241178655872	12.725 ± 0.029	16.737 ± 0.003	36.887 ± 0.088	18.902 ± 0.006
J1938+4321 ‡	294.7019820	43.3553497	2077988676275617408	12.708 ± 0.022	16.404 ± 0.001	37.376 ± 0.048	18.541 ± 0.003
J2019+2256 †	304.9530278	22.9457810	1829571684884360832	13.820 ± 0.111	19.444 ± 0.003	33.938 ± 0.342	21.791 ± 0.022

^a – Estimated by Faherty et al. (2021) using SpeX spectral data.

data is generally the same for both the prism and SXD data, with the exception of the telluric correction methods: the prism data use a convolution kernel created using the Instrument Profile method, while the convolution kernels for the SXD data are constructed through the deconvolution method using the Pa δ line which lies around 1.005 μm (Paschen 1908). The reduction for the ARCoIRIS

data utilised a version of SPECTOOL adapted for ARCoIRIS spectra

Table 2. Basic data for each of the UCDs in this paper. Spectroscopic classifications (SpT) of the UCDs are as given by SPLAT, and photometric spectral types (PhT) are also shown. Where applicable, published NIR and optical spectroscopic classifications for each UCD are also shown. UCDs with entries in *italics* are those which have spectra with sub-optimal signal-to-noise or poor telluric standard star availability, thus their derived properties are not definitive. Effective temperature and surface gravity estimate derivations are outlined in Section 7, and spectrophotometric distances are calculated in Section 6. UCDs marked with a dagger † are those observed with SpeX Prism, those marked with a double dagger ‡ are observed with SpeX SXD, and those marked with an asterisk * are observed with ARCoIRIS. This data is also contained within the collated data table in Appendix D.

Object Short Name	SIMBAD Name	SpT (this work)	PhT (this work)	Published NIR SpT	Published Optical SpT	T _{eff} (K)	Spectrophotometric Distance (pc)
J0508+3319 ‡	2MASS J05085506+3319272	L2 ± 0.4	L1 ± 2.5	–	L2 ^[1]	2000 ± 60	21.97 ± 1.42
J0515+0613 ‡	<i>Gaia</i> DR2 3240769806581623296	M9 ± 0.4	M9 ± 3.0	–	–	2800 ± 120	76.19 ± 1.48
<i>J0526–5026</i> *	<i>2MASS J05265973–5026216</i>	<i>L6 ± 0.4</i>	<i>L8 ± 2.0</i>	–	<i>L3^[2]</i>	<i>1700 ± 90</i>	<i>22.01 ± 0.88</i>
<i>J0542+0041</i> ‡	<i>Gaia</i> DR3 3219457457305021568	<i>L7 ± 1.2</i>	<i>L9 ± 2.5</i>	–	–	<i>1600 ± 180</i>	<i>15.84 ± 1.15</i>
J0723+4622 ‡	<i>Gaia</i> DR3 974639306231785344	L1 ± 0.5	L0 ± 4.5	–	–	2000 ± 200	74.95 ± 3.82
J0808+3157 ‡	2MASS J08080189+3157054	M7 ± 0.4	M7 ± 1.5	–	–	3000 ± 130	26.68 ± 0.36
J0811+1855 ‡	2MASS J08111040+1855280	L1 ± 0.4	L3 ± 2.0	–	L1 ^[3]	2600 ± 80	31.71 ± 0.45
J0817–6155 *	2MASS J08173001–6155158	T6 ± 0.4	T7 ± 1.5	T6 ^[4]	–	1200 ± 70	4.93 ± 0.31
J0832+3538 †	LP 258–34	M6 ± 0.4	M6 ± 2.0	–	–	2800 ± 140	26.79 ± 0.37
J0850–0318 †	2MASS J08500913–0318305	M8 ± 0.4	M7.5 ± 1.5	–	–	2600 ± 100	44.02 ± 1.12
J0900+5205 ‡	SDSS J090051.84+520512.1	M9 ± 0.4	L0 ± 1.0	–	L0 ^[6]	2800 ± 160	92.68 ± 4.24
J0911+1432 ‡	SDSS J091136.57+143244.4	M9 ± 0.5	M9 ± 2.5	–	L0 ^[6]	2600 ± 80	58.50 ± 1.74
J0916–1121 ‡	2MASS J09165708–1120597	M8 ± 0.4	M7 ± 2.0	M9 ^[7]	–	2600 ± 80	41.99 ± 1.02
J0941+3315A ‡	<i>Gaia</i> DR3 794031395948224640	M8 ± 0.4	M8 ± 2.0	–	–	2800 ± 100	38.85 ± 6.84
J0942–2551 ‡	<i>Gaia</i> DR3 5658599213249509120	L1 ± 0.4	L0 ± 2.0	–	–	2800 ± 130	60.40 ± 1.88
J0948+5300 ‡	2MASS J09481259+5300387	L1 ± 0.4	M9 ± 3.0	L2 ^[8]	–	2000 ± 160	51.34 ± 2.53
J1036–3441 *	2MASSW J1036530–344138	L8 ± 0.4	T0 ± 1.5	L6.5 ^[9]	L6 ^[10]	1700 ± 80	15.40 ± 0.22
J1048–5254 *	DENIS J104827.8–525418	L1 ± 0.4	M8.5 ± 1.0	L0.5 ^[11]	L1.5 ^[12]	2100 ± 150	25.06 ± 0.95
J1126–2706 ‡	2MASS J11263718–2706470	M8 ± 0.4	M7 ± 1.0	–	–	2700 ± 100	45.10 ± 0.97
J1143+5324 †	<i>Gaia</i> DR3 840382713073253760	L1 ± 0.4	L1 ± 4.0	–	–	2400 ± 60	69.53 ± 1.33
J1150–2914 ‡	<i>Gaia</i> DR2 3480771277705948928	L0 ± 0.4	L0 ± 4.5	–	–	2000 ± 170	44.39 ± 1.76
J1152+5901 ‡	<i>Gaia</i> DR2 846350351086394752	L0 ± 0.4	M8.5 ± 3.0	–	–	2000 ± 200	64.88 ± 4.50
J1158–0008 *	2MASS J11583104–0008491	M9 ± 0.4	M8 ± 3.0	–	–	2700 ± 100	91.78 ± 3.44
J1158+3817 ‡	2MASS J11581724+3817203	M7 ± 0.4	M7.5 ± 1.5	–	–	2700 ± 90	65.50 ± 1.39
J1212+0206 *	2MASS J12123389+0206280	L1 ± 0.4	L1 ± 3.0	L1 ^[5]	L1 ^[6]	2600 ± 150	50.76 ± 5.36
J1215+0042 *	<i>Gaia</i> DR3 3698542165611096064	M9 ± 0.4	L2 ± 2.5	–	–	2800 ± 160	72.98 ± 3.08
J1243+6001 †	<i>WISE</i> J124332.17+600126.6	L7 ± 0.4	M8.5 ± 2.5	L8 ^[13]	–	1600 ± 130	43.46 ± 12.28
J1250+0455 ‡	2MASS J12501559+0455065	M9 ± 0.4	L2 ± 1.5	–	–	2600 ± 110	58.53 ± 3.22
J1252+0347 *	2MASS J12523834+0347351	M8 ± 0.4	M9 ± 2.5	–	M7 ^[15]	2500 ± 70	82.67 ± 2.10
J1307+0246 *	2MASS J13073376+0246048	L1 ± 0.4	L2 ± 5.0	–	–	2000 ± 90	54.08 ± 1.48
J1313+1404 ‡	<i>Gaia</i> DR2 3743732776411929472	M8 ± 0.4	L1 ± 2.5	–	–	2800 ± 130	86.18 ± 3.29
J1315+3232 ‡	2MASS J13151905+3232031	M7 ± 0.4	M6 ± 2.0	–	–	2900 ± 110	30.90 ± 0.99
J1320+4238 ‡	LP 218–81	M7 ± 0.4	M6 ± 1.0	–	–	3000 ± 130	29.41 ± 0.99
J1420+3235 ‡	<i>Gaia</i> DR2 1477880589944207744	M7 ± 0.4	M6 ± 2.5	–	–	2900 ± 110	45.04 ± 0.97
J1423+5146 ‡	LP 134–7	M7 ± 0.4	M6 ± 2.0	–	M7 ^[14]	2900 ± 130	18.64 ± 0.44
J1441+4217 ‡	<i>Gaia</i> DR3 1490058849451967744	L3 ± 0.6	L0 ± 1.5	–	–	1600 ± 140	42.65 ± 1.83
J1452+0931 *	2MASS J14520130+0931372	M8 ± 0.4	M9 ± 2.5	–	L0 ^[15]	2700 ± 90	75.64 ± 2.28
J1514+3547 ‡	<i>Gaia</i> DR3 1291186058168054016	L1 ± 0.5	L1 ± 3.0	–	–	2600 ± 60	59.63 ± 4.50
J1536+0646 *	2MASS J15365938+0646507	L0 ± 0.4	L2 ± 3.0	–	–	2500 ± 70	65.82 ± 2.63
J1544–0435 †	<i>Gaia</i> DR2 4402274889228322944	L1 ± 0.4	L1 ± 1.5	–	–	1700 ± 100	55.66 ± 2.54
J1544+3301 ‡	2MASS J15445518+3301447	L2 ± 0.4	L1.5 ± 1.5	–	L6 ^[16]	1500 ± 110	44.47 ± 5.83
J1628–4652 *	<i>Gaia</i> DR3 5942058396163925376	M8 ± 0.4	L1.5 ± 3.0	–	–	2800 ± 100	81.69 ± 2.46
J1637+1813 †	<i>Gaia</i> DR2 4562510841912952192	M7 ± 0.4	M6.5 ± 1.5	–	–	2200 ± 100	84.94 ± 5.82
J1646–2115 †	2MASS J16462325–2115064	sdL2 ± 0.4	L2 ± 3.0	–	–	2300 ± 40	49.11 ± 4.14
<i>J1654–3819</i> ‡	<i>2MASS J16541588–3818593</i>	<i>M6 ± 0.4</i>	<i>M6 ± 1.0</i>	–	–	<i>2600 ± 200</i>	<i>26.17 ± 4.03</i>
<i>J1700–4048</i> *	<i>Gaia</i> DR3 5966993223906484992	<i>L4 ± 0.4</i>	<i>L5.5 ± 4.0</i>	–	–	<i>1600 ± 220</i>	<i>50.23 ± 3.84</i>
J1713–3952 ‡	<i>Gaia</i> DR3 5972124644679705728	L1 ± 0.4	L2 ± 1.0	–	–	2500 ± 80	20.15 ± 1.26
J1737+4705 ‡	2MASS J17373855+4705511	M8 ± 0.4	M8.5 ± 1.5	–	–	1200 ± 100	48.78 ± 1.16
J1847–3419 ‡	2MASS J18474700–3419345	M7 ± 0.4	M7 ± 1.5	–	–	2900 ± 120	26.98 ± 0.55
J1938+4321 ‡	LSPM J1938+4321	M6 ± 0.4	M6 ± 2.5	–	–	2900 ± 120	29.50 ± 0.36
J2019+2256 †	<i>Gaia</i> DR2 1829571684884360832	L2 ± 0.4	L1.5 ± 1.5	–	–	1800 ± 80	21.84 ± 1.74

References

- [1] – Kirkpatrick et al. (2016) [2] – Reid et al. (2008) [3] – Schmidt et al. (2015)
 [4] – Artigau et al. (2010) [5] – Faherty et al. (2009) [6] – Kiman et al. (2019) [7] – Kirkpatrick et al. (2014)
 [8] – Kellogg et al. (2017) [9] – Burgasser et al. (2010) [10] – Gizis (2002) [11] – Folkes et al. (2012)
 [12] – Phan-Bao et al. (2008) [13] – Faherty et al. (2021) [14] – Kirkpatrick et al. (2024) [15] – Zhang et al. (2010)
 [16] – Schmidt et al. (2014)

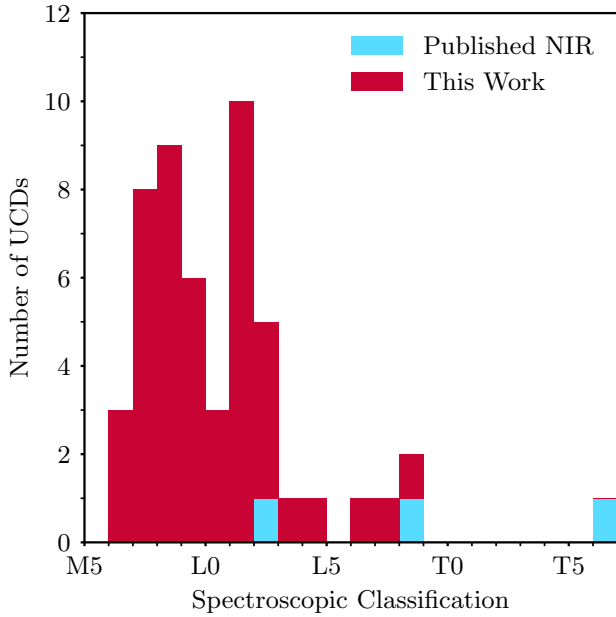


Figure 1. Histogram of previously published NIR spectroscopic classifications for the UCDs presented in this work (blue) and the contribution of the new NIR spectral type classifications of UCDs from this work (red).

by K. Allers¹, and thus follows the same general reduction process as the SpeX SXD data.

Perhaps the most critical part of the reduction process is the telluric correction for each UCD, specifically the selection of the standard star to be used for correcting each science object’s spectrum. The primary method of choosing the standard star was finding the best airmass-match for each object, so that the observing conditions are as similar as possible for the science target and the standard. In most cases, the best airmass-matched telluric standard also has the smallest time difference between when the observations were taken. The observing schedule was designed so that each UCD observation was followed by an observation of a A0V standard star, minimising the effects of the changing sky conditions. When the airmass difference between a UCD and the following telluric standard star exceeds 0.100, the next-closest time-matched standard star is tested in the telluric correction process and the result judged by visual inspection. This process is repeated until the standard star with the optimal balance of time-match and airmass difference is found: the telluric standard with the smallest residuals is selected.

The spectra are also flux calibrated during the telluric correction process, using the *B* and *V* magnitudes of the A0-type standard stars. These magnitudes are used by the *xtellcor* program for IDL to scale a high-resolution model spectrum of Vega to use for the absolute flux calibration (Vacca et al. 2003). The *B* and *V* magnitudes for scaling the Vega model spectrum are included in the observing log in Appendix A.

¹ The adaptation of SPEXTOOL for ARCoIRIS data is publicly available from: <https://www.dropbox.com/sh/wew08hcqluib8am/AAC6H1CeAVoiDPSe-MXRU2Cda?dl=0>

3 SPECTRAL CLASSIFICATION

3.1 Spectroscopic Classification using SPLAT

The SpeX Prism Library Analysis Toolkit² PYTHON module (hereafter SPLAT; Burgasser & Splat Development Team 2017) was used to classify the spectral type of each UCD. By using the `classifyByStandard` routine, the spectroscopic type of each of the UCDs can be found (presented in Table 2). The `classifyByStandard` classification method uses a spectral standard of each spectral type, M0 through T9, from the SpeX Prism Library (Burgasser et al. 2006; Kirkpatrick et al. 2010; Cushing et al. 2011) and compares it with the spectrum of interest by minimising chi-squared values. SPLAT then returns the best-fitting spectral classification for the UCD, along with associated uncertainties calculated using the distribution of chi-squared values for each spectral type fit.

First, we used the `classifyByStandard` built-in Kirkpatrick method to classify the spectral type of each UCD by fitting the standard spectra to only the 0.9–1.4 μm band (Kirkpatrick et al. 2010). In most cases, this gives a spectral type which matches the overall shape of the spectrum. To verify these classifications, we also used the SPLAT `classifyByStandard` routine to match each object’s spectrum with the SpeX Library standards over the entire spectrum, with the spectral types derived using the two methods agreeing with each other within ± 1.0 spectral types. We take the adopted spectroscopic classification as the weighted mean of the Kirkpatrick-method and whole-spectrum fits, and the associated uncertainties are calculated as the standard errors of the weighted means. When the weighted mean gives a classification in-between spectral types, the two spectral types are compared by-eye and the best-fitting classification is selected.

Overall, comparisons with published spectral types for these UCDs show that our classifications are consistent with published spectral types (Table 2). For some UCDs, the spectral classifications are equivalent to those published, while other UCDs’ spectral types vary by a few subtypes (such as J0526–5026), likely due to poor observing conditions leading to spectra with poor signal-to-noise ratios or the UCD being a non-single source (see Section 9.4). Fig. 1 shows a histogram of previously spectroscopically classified UCDs in the GUCDS sample (blue) and the new UCD classifications contributed by this work (red).

SPLAT returns L0 as the best-fitting spectral classification for J1646–2115, however visual inspection and comparison with its photometric data suggest that it is more likely to be an early-L subdwarf. Using the `std_class = "subdwarf"` option, SPLAT gives an sdL0 classification, which is closer to our suspected early-L subdwarf classification. Based on the combination of our by-eye classification, SPLAT’s spectroscopic classification and the photometric classification (see Section 3.2), we take the spectral type of J1646–2115 to be sdL2. The potential of J1646–2115 being a subdwarf is discussed in further detail in Section 10.2.

3.2 Photometric Classification

The spectral classification method outlined by Skrzypek et al. (2015) can be used to find the spectral types of the UCDs photometrically, as a means of checking the spectral types given by SPLAT. For this work, we use Pan-STARRS *i*, *z* and *y* magnitudes; 2MASS *J*,

² The SPLAT module for PYTHON is publicly available from: <https://github.com/aburgasser/splat>

H and *K_s* photometry, and CatWISE2020 *W1* and *W2* magnitudes (Eisenhardt et al. 2020; Marocco et al. 2021) of published UCDs to create a template relation between spectral classification and a range of colours. Appendix C outlines the template used for the photometric classification. Not all of the 51 UCDs have complete sets of 2MASS and CatWISE2020 magnitudes, so these were classified using the photometry which is available. By calculating χ^2 values for each of the UCDs, the best-fitting photometric spectral type can be found. The photometric classifications are shown alongside the spectroscopic types in Table 2.

3.3 Comparison of Spectroscopic and Photometric Spectral Types

The spectroscopic classifications that we obtained with SPLAT can be compared with those derived from photometric data, in order to ensure consistency between the different classification methods. This also allows us to identify any UCDs with differing spectroscopic and photometric classifications, since these may indicate non-solar metallicities or unusual surface gravity values. Table 2 shows a comparison between the two sets of classifications, verifying that the spectral types given by the spectroscopic and photometric methods are fairly consistent. The majority of the photometric spectral types lie within the uncertainties of the spectroscopic classifications, with only a few UCDs which do not have overlapping photometric and spectroscopic classification uncertainties: J1048–5254, J1243+6001 and J1250+0455. These UCDs will be investigated in more detail in Section 10.

3.4 Comparison of NIR and Optical Classifications

NIR and optical observations of UCDs probe different depths of the objects' atmospheres, and can provide clarification when an object is suspected to be an unresolved binary. Nine of our UCDs have published optical spectral classifications (Table 3). The robustness of our NIR spectroscopic types is verified by the optical classifications, with most of the NIR and optical types falling within the uncertainties of each other, although there are two exceptions: J1036–3441 and J1536+0646.

J1036–3441 has a NIR spectral classification of L8, while its optical spectral type is given as L6 by Gizis (2002). This 2-subtype difference could be due to a number of reasons, such as the UCD's age or the UCD being an unresolved binary. Further investigation of J1036–3441's potential binarity is presented in Section 10.4.5.

J1536+0646 has an L0 NIR spectral type and a L2-type optical photometric classification given by Zhang et al. (2010). As with J1036–3441, this difference in spectral classifications could be caused by the UCD's age or the UCD being an unresolved binary. Section 10.4.10 contains further investigation of the properties of J1536+0646.

4 SPECTRAL ANALYSIS

4.1 Spectral Plots

By creating stacked plots of the spectra sorted by spectral type, it is possible to check that our spectral classifications are logical and follow the expected trend as spectral classifications progress from late-M to T-type (see Geballe et al. 2002; Kirkpatrick 2005; Burgasser et al. 2009, among others). By inspecting these plots, we are also able to identify any interesting features within the spectra.

Table 3. Comparison of NIR SpT classifications (this work) and optical spectral types (published). Where available, spectral type uncertainties are also included.

Short Name	NIR SpT	Optical SpT	Optical PhT
J0508+3319	L2 ± 0.4	L2 ^[1]	–
J0526–5026	L6 ± 0.4	L3 ^[2]	–
J0811+1855	L1 ± 0.4	L1 ^[3]	–
J1036–3441	L8 ± 0.4	L6 ^[4]	–
J1048–5254	L1 ± 0.4	L1.5 ^[5]	–
J1158–0008	M9 ± 0.4	–	M9.5 ^[6]
J1212+0206	L1 ± 0.4	L1 ^[7]	–
J1452+0931	M8 ± 0.4	L0 ^[6]	–
J1536+0646	L0 ± 0.4	–	L2 ^[6]

References	^[1] – Kirkpatrick et al. (2016)
^[2] – Reid et al. (2008)	^[3] – Schmidt et al. (2015)
^[4] – Gizis (2002)	^[5] – Phan-Bao et al. (2008)
^[6] – Zhang et al. (2010)	^[7] – Kiman et al. (2019)
^[8] – Faherty et al. (2009)	

As can be seen from the spectral plots in Figs. 2 & 3, the low resolution of the SpeX prism compared to the other instruments used in this work is clear. The later-type UCDs have much noisier spectra, so the highest and lowest wavelength ends of the spectra have been removed from the plots since there is too much noise to make use of the flux these regions.

With simple visual inspection, it can be seen that most of the UCD spectra follow the sequence that would be expected from the progression from M-type through T-type classifications, though there are a few UCDs with unusual spectral shapes: J1143+5324 has a relatively triangular-shaped *H*-band; J1243+6001 has an overall positive gradient in its spectrum, and J1646–2115 has a very blue NIR spectrum. There are also UCDs with unusual spectral features: J0811+1855 and J1637+1813 have deep FeH lines in the *J*-band, and J0542+0041 and J0811+1855 have strong TiO features in the *J*-band. Each of these UCDs will be investigated individually in Section 10.

Some of the spectra appear to be interesting, but this is caused by poor signal-to-noise ratios due to inadequate observing conditions. J0900+5205 has an unusual shape to its *J*-band and comparatively flat *H* and *K*-bands, however the overall shape of the spectrum and strengths of the spectral features are not dissimilar to that of a typical late-M UCD. J0948+5300 has a relatively flat *H*-band, and J1700–4048 has a spectrum which is flatter and smoother than expected in its entirety (although this may be a consequence of poor observing conditions rather than its intrinsic spectral characteristics). All of these spectra are likely to be victims of poor conditions during the observations: adverse weather conditions such as cloud cover or wind gusts can cause poor signal-to-noise ratios in observations, hence causing the spectra observed to be difficult to characterise once the noise is smoothed out.

4.2 Comparisons with Other Available NIR Spectra

Using the GUCDS Data Browser (Cooper & Nicastro 2023) and the SIMPLE Database (Cruz et al. 2023), any available spectra for the UCDs can be found and compared with those in this work. There are a handful of UCDs with published NIR spectra: J0808+3157, J0948+5300 and J1036–3441. Fig. 4 shows a comparison between the spectra obtained in this work with those previously published.

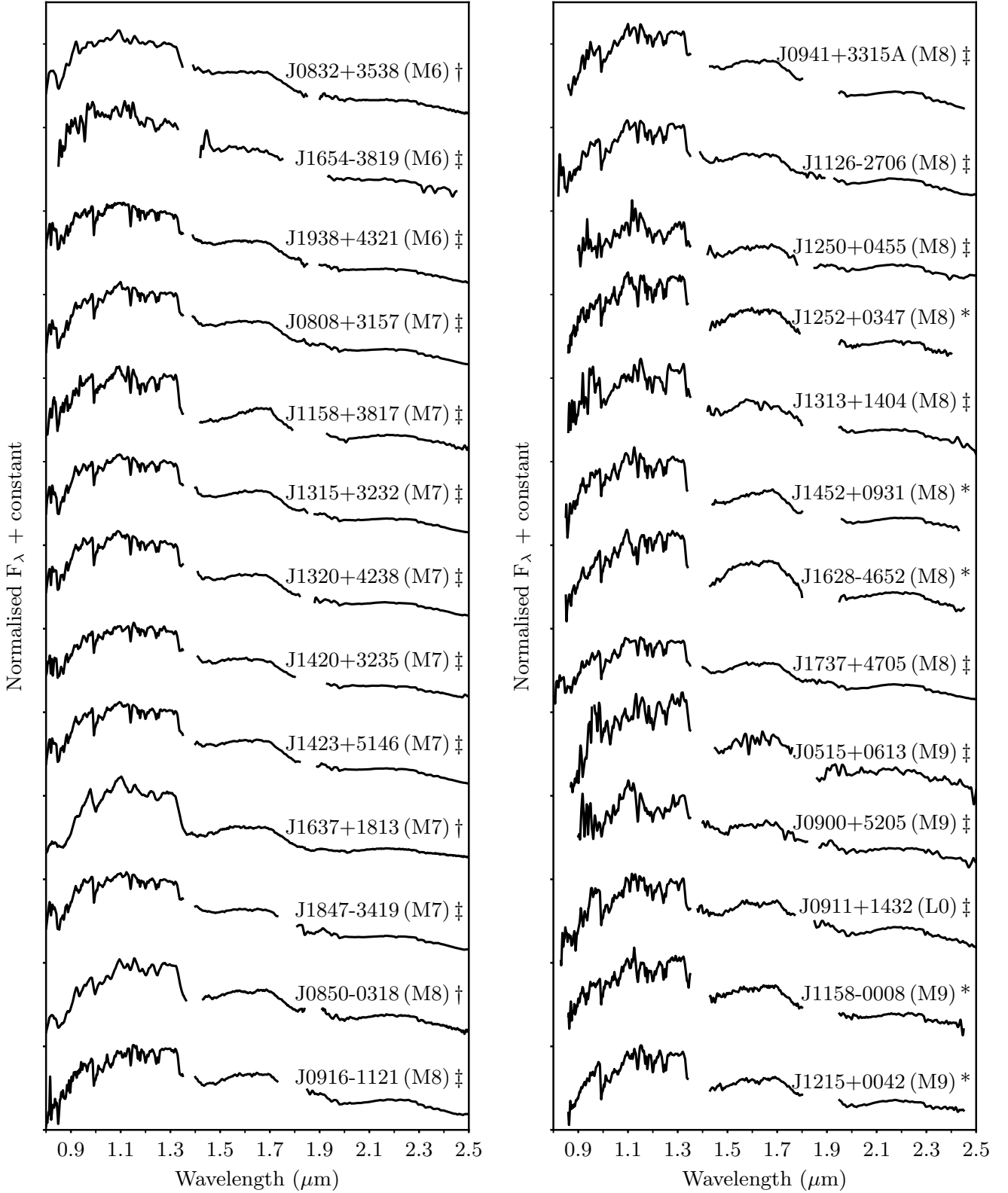


Figure 2. Left: plots of the UCD spectra, sorted by spectral classification (M6–M8). Right: plots of the UCD spectra, sorted by spectral classification (M8–M9). Each spectrum is normalised at $1.27\ \mu\text{m}$ and vertically offset by equal flux increments. Noisy areas around the H_2O bands at $\sim 1.3\ \mu\text{m}$ and $\sim 1.9\ \mu\text{m}$ have been removed to make plots clearer. UCDS marked with a dagger \dagger are those observed with SpeX Prism, those marked with a double dagger \ddagger are observed with SpeX SXD, and those marked with an asterisk $*$ are observed with ARCoIRIS.

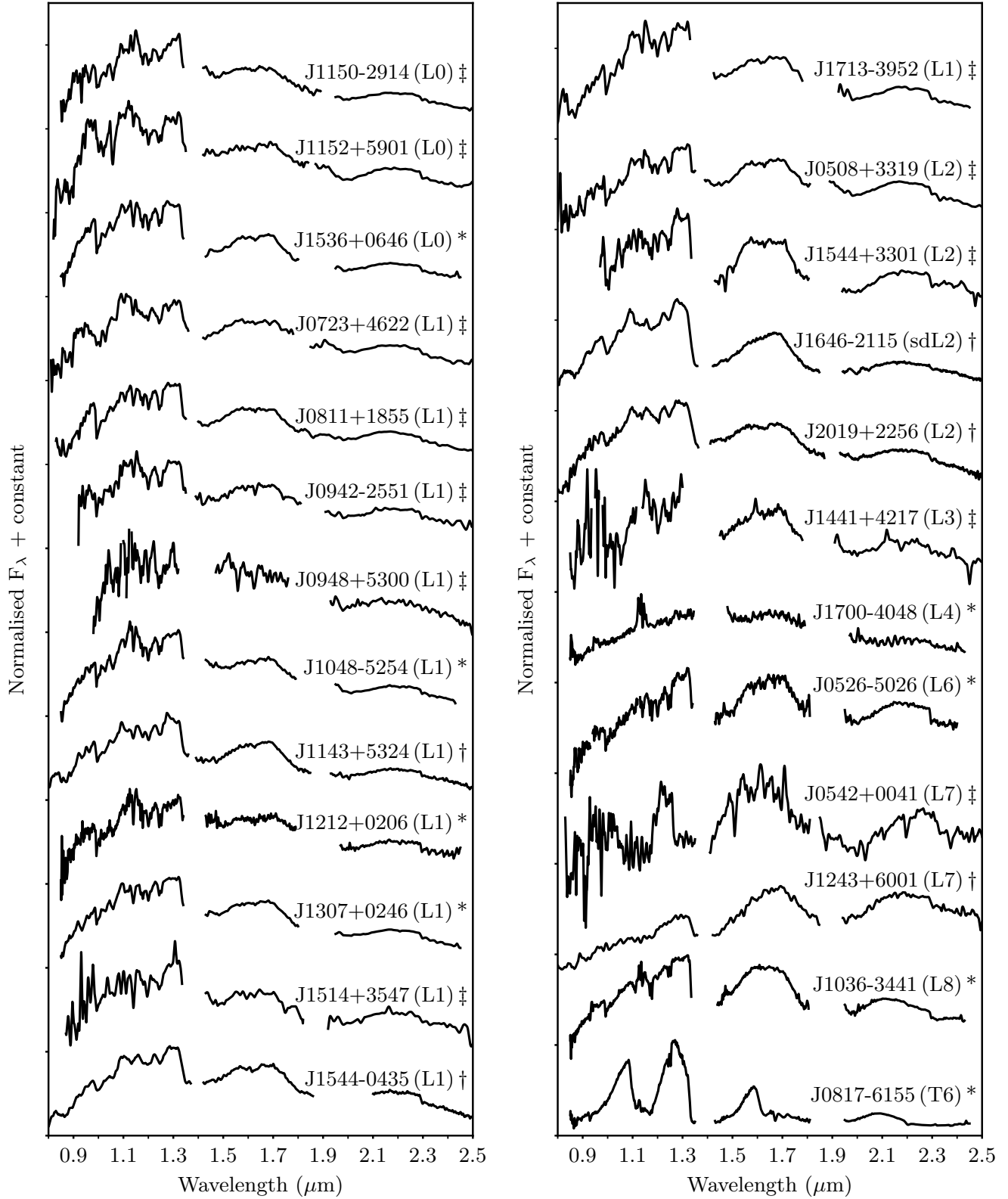


Figure 3. Left: plots of the UCD spectra sorted by spectral classification (L0–L1). Right: plots of the UCD spectra, sorted by spectral classification (L1–T6). Each spectrum is normalised at 1.27 μm and vertically offset by equal flux increments. Noisy areas around the H₂O bands at $\sim 1.3 \mu\text{m}$ and $\sim 1.9 \mu\text{m}$ have been removed to make plots clearer. UCDs marked with a dagger † are those observed with SpeX Prism, those marked with a double dagger ‡ are observed with SpeX SXD, and those marked with an asterisk * are observed with ARCoIRIS.

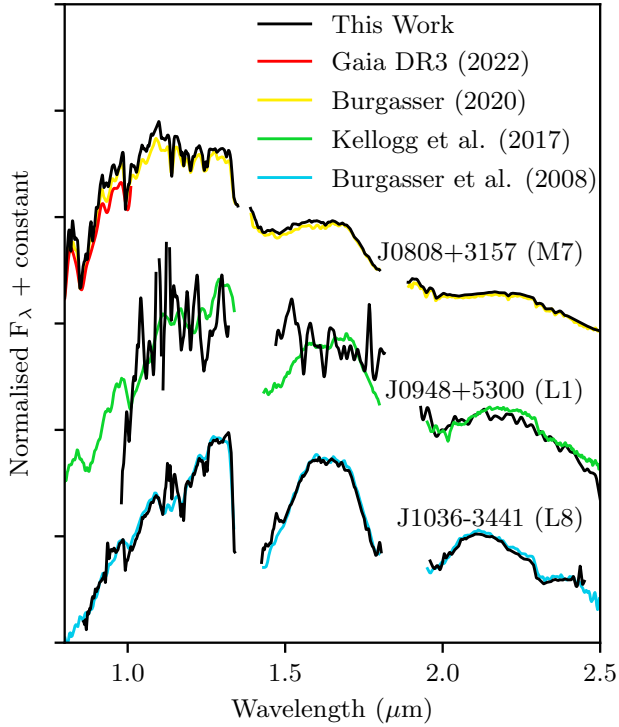


Figure 4. Comparison of the spectra obtained in this work with previously published NIR spectra of the same UCDS.

Generally, all of the previously published spectra match those in Figs. 2 & 3.

J0808+3157 was observed in 2020 (program 2020B057, PI: Smart), and although the spectrum has not been included in any publications it can be found in the GUCDS Data Browser and NASA/IPAC Infrared Science Archive³. This spectrum was obtained using the SpeX prism configuration, thus it is directly comparable to the spectrum presented in this work which was taken with the SpeX SXD configuration. There is also *Gaia* DR3 XP spectral data available for J0808+3157, which reaches up to $1.05\ \mu\text{m}$ (Gaia Collaboration et al. 2016). As can be seen in Fig. 4, all of the observations show the same general spectral shape expected of an M7-type UCD, with only minor deviations which likely arose due to small differences in the observing conditions and reduction processes.

J0948+5300 has a spectrum that was previously obtained using the SpeX prism configuration in 2015 and published by Kellogg et al. (2017). A visual comparison of our spectrum and the one obtained by Kellogg et al. (2017) immediately highlights some differences. While the general shapes of the *J*-bands are similar, the *H*-band has significant deviations. The *H*-band of the Kellogg et al. (2017) spectrum has a much more pronounced arched shape than that of the spectrum obtained for this work. A major contributor to the differences in the two spectra is likely to be the poor quality of the observation obtained for this work, since the observing conditions for our SpeX SXD observation were poor, resulting in a spectrum which is much noisier than desired. Due to the poor signal-

³ A summary of the observation can be found at https://irsa.ipac.caltech.edu/data/IRTF/2020B/20201124/summary/2020B057/sbd_20201124_140156/summary.html

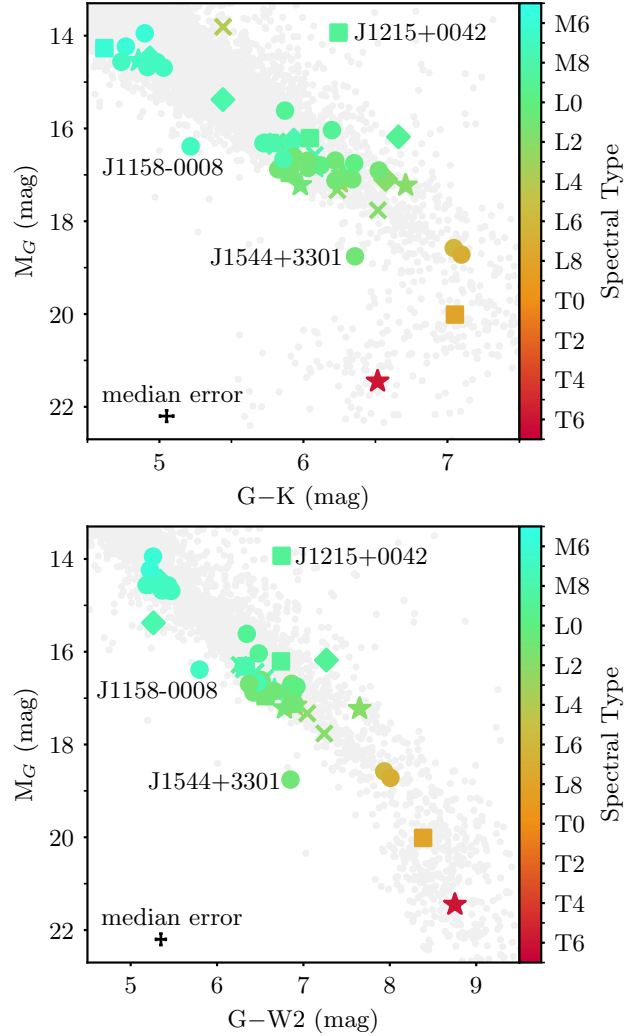


Figure 5. Top: CMD of M_G versus $G-Ks$ for the UCDS. Bottom: CMD of M_G versus $G-W2$ for the UCDS. The colour corresponds to the spectral type of the UCD: blue objects are earlier types and red objects are later types. The median uncertainties are plotted as error bars in the lower left corner of each plot. Grey points are objects from the GUCDS Master list, showing the expected distribution of UCDS on the CMD. Labeled UCDS lie away from the expected distribution and are investigated in Section 10. UCDS plotted as a star \star are potentially young (see Section 9.1), and those plotted as a cross \times are thick disc UCDS and subdwarfs (see Section 9.2). Diamonds \blacklozenge indicate wide binary UCDS (Section 9.3) and squares \blacksquare denote potential unresolved binaries (Section 9.4).

to-noise ratio of our spectrum for J0948+5300, it is likely that the spectrum presented by Kellogg et al. (2017) is a better representation of UCD's spectral shape.

J1036-3441 was observed in 2010 with the SpeX prism configuration, and the results were published by Burgasser et al. (2010). The two spectra are incredibly similar, aside from the differences in resolutions of the instruments and minor deviations due to differences in the reduction methods. This similarity between the spectra strengthens our L9 spectral classification for this UCD.

5 COLOUR-MAGNITUDE DIAGRAMS

Plotting colour-magnitude diagrams (hereafter CMDs) allows for the redness (or blueness) of each UCD to be visualised and compared to the expectations for UCDs with similar absolute G -band magnitudes. This, in turn, means that any of our UCDs which have unusual colours or absolute G -band magnitudes can be identified so that they can be investigated in more depth in Section 10.

5.1 Absolute G -band magnitude versus $G-K_s$ colour

By plotting absolute G -band magnitude against $G-K_s$ colour in a CMD, a clear relation can be seen (Fig. 5, top panel). As with the photometric classification outlined in Section 3.2, *Gaia* G and 2MASS K_s magnitude values are used. Two of our UCDs do not have K_s magnitude data available, so are not plotted on this CMD: J1243+6001 and J1628–4652.

As expected, the brighter UCDs have bluer colours than the fainter UCDs. The shape of the distribution of our UCDs resembles that seen in fig. 10 of [Smart et al. \(2019\)](#), although J1215+0042 is brighter than would be expected for a UCD of the same colour. J1158–0008 and J1544+3301 both lie slightly below the grey points, suggesting that they may be subdwarfs. Section 10 discusses these UCDs individually in more detail.

5.2 Absolute G -band magnitude versus $G-W_2$ colour

Using CatWISE2020 W_2 magnitude values, the absolute G -band magnitude can be plotted against the $G-W_2$ colour in a CMD (Fig. 5, bottom panel). CatWISE2020 W_2 magnitudes are not available for some of the UCDs: J0850–0318, J1628–4652, J1700–4048 and J2019+2256.

This CMD is similar to fig. 11 of [Smart et al. \(2019\)](#), and the trends are comparable, following the expected relation of brighter UCDs having bluer $G-W_2$ colours than fainter UCDs. J1215+0042 again is brighter than would be expected. J1158–0008 and J1544+3301 again lie below the grey points, furthering that they could be subdwarfs. These UCDs will be discussed in more detail in Section 10.

6 SPECTROPHOTOMETRIC DISTANCES

Using the spectral type-absolute magnitude relations defined by [Dupuy & Liu \(2012\)](#), we have been able to calculate spectrophotometric distances for the UCDs in our sample. Since the majority of our UCDs have 2MASS and CatWISE2020 photometry (only five UCDs are missing some photometric data), we calculated spectrophotometric distances using 2MASS J , H and K -band magnitudes as well as CatWISE2020 W_1 and W_2 -band photometry. We take the spectrophotometric distance to be the mean of the distance values, and the uncertainties to be the standard deviation of the values. (Table 2). These distances can then be compared to the parallactic distances derived from the *Gaia* parallax measurements, thus highlighting any over-bright UCDs (suggestive of unresolved binarity).

7 ESTIMATING EFFECTIVE TEMPERATURES

Effective temperatures are a valuable tool for constraining the properties of UCDs, particularly in categorising potential planetary

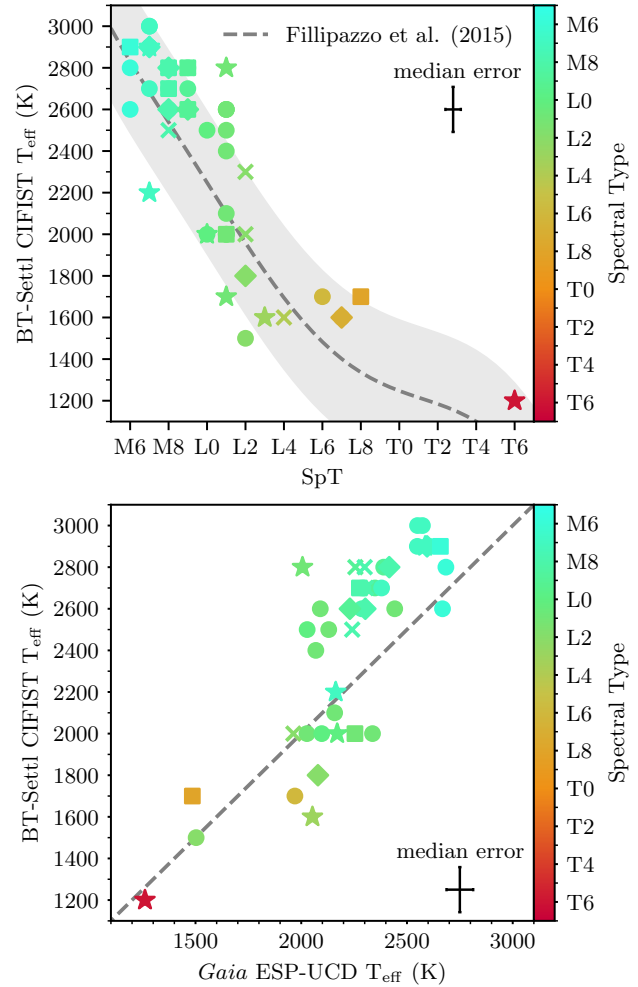


Figure 6. Top: Plot showing estimated effective temperature against spectral type for the UCDs in this paper. The grey dashed line shows the spectral type-temperature relation from [Filippazzo et al. \(2015\)](#), and the shaded region corresponds to their 1σ uncertainty. Bottom: comparison of ESP-UCD effective temperature calculations and our effective temperature estimates. The grey dashed line represents the 1:1 ratio of ESP-UCD and BT-Settl CIFIST effective temperature. The median uncertainties are plotted as error bars in the corner of each plot. Colours and symbols are the same as in Fig. 5.

objects and identifying brown dwarfs. By performing a chi-squared fit of the BT-Settl CIFIST models from [Baraffe et al. \(2015\)](#) to each UCD (as outlined by [Marocco et al. 2013](#)), the effective temperature of the UCD can be deemed to be that corresponding to the smallest χ^2 . It was possible to use this fitting method to also find an estimate for the surface gravity of the UCD, as [Baraffe et al. \(2015\)](#) provides models containing variations in both temperature and $\log(g)$, however the surface gravity was kept constant at $\log(g) = 5.0$ dex throughout the fitting process to ensure consistency in the fits (and because of the known degeneracy between effective temperatures and $\log(g)$; [Kirkpatrick 2005](#)). Uncertainties are derived from the standard deviations of the results of the chi-squared fitting process for each UCD. Table 2 shows the effective temperatures for each UCD from the chi-squared fitting.

The top plot in Fig. 6 shows the relation between our estimated temperatures using the BT-Settl CIFIST grid and our spectral classification of each UCD (as in fig. 4 by [Ravinet et al. 2024](#)).

Table 4. Spectral lines used in the measurements of radial velocity with both line-centring and cross-correlation methods of `rvfitter`.

Line	Wavelength (μm)
Na I-a	0.8133
Na I-b	0.8195
Na I-c	1.1381
Na I-d	1.1404
K I-a	1.1690
K I-b	1.1773
K I-c	1.2432
K I-d	1.2522

Table 5. Published radial velocity values for UCDSs in our sample, along with the difference between our measured radial velocity and those previously published. J0900+5205 has no uncertainties associated with its published radial velocity.

Object Short Name	Published Radial Velocity (km s^{-1})	Measured Radial Velocity (km s^{-1})	Radial Velocity Difference (km s^{-1})
SpeX SXD			
J0808+3157	31.1 ± 0.06 ^[1]	36.5 ± 12.9	5.4
J0811+1855	31.0 ± 10.6 ^[2]	26.5 ± 14.6	4.5
J0900+5205	-14.5 ^[2]	5.1 ± 17.5	19.6
J1423+5146	28.9 ± 0.04 ^[1]	33.4 ± 12.8	4.5
J1544+3301	-32.1 ± 16.5 ^[2]	-8.6 ± 16.3	23.5
ARCoIRIS			
J1536+0646	41.7 ± 13.7 ^[2]	32.6 ± 17.9	9.1
References ^[1] – Jönsson et al. (2020) ^[2] – Kiman et al. (2019)			

The general shape distribution of our estimated temperatures follows the relation from Filippazzo et al. (2015), with the majority of our effective temperature estimates laying within 3σ of their relation once effective temperature uncertainties are taken into account (Filippazzo et al. 2015 state that their uncertainty for their spectral type-effective temperature relation is $\sigma = 113$ K, with this 3σ uncertainty shown as the shaded grey region in the top panel of Fig. 6).

The bottom plot in Fig. 6 shows a comparison between our estimated effective temperatures and those given by the *Gaia* Astrophysical Parameters Inference System (hereafter Apsis; Bailer-Jones et al. 2013) module for UCDSs called the Extend Stellar Parametrizer - UltraCool Dwarfs (hereafter ESP-UCD). The grey dashed line corresponds to a 1:1 relation between the ESP-UCD effective temperature and our estimates. As can be seen from the plot, our estimated temperatures for the hottest UCDSs (> 2000 K) are higher than those determined by the Apsis module, and there is significant scatter around ~ 2000 K. A similar trend is seen by Ravinet et al. (2024), with their estimated effective temperatures also being higher than the ESP-UCD temperatures for the hottest UCDSs. This difference at the hotter temperatures likely arises due to the correction factor that the ESP-UCD module uses to correct for overestimations of effective temperatures at in the hotter regime (Ulla et al. 2022).

Table 6. The radial velocity values measured using the cross-correlation and line-centring methods for the SXD and ARCoIRIS observations. We take the adopted radial velocity to be the weighted mean of the two methods. Na I-a and Na I-b lines were not used in the radial velocity measurements for UCDSs in *italics* due to excessive noise in the short-wavelength part of the spectra. The adopted radial velocity data is also contained within the collated data table in Appendix D.

Object Short Name	Cross Correlation (km s^{-1})	Line Centring (km s^{-1})	Adopted Radial Velocity (km s^{-1})
J0508+3319	51.5 ± 18.3	46.3 ± 20.3	49.4 ± 13.6
<i>J0515+0613</i>	<i>74.1 ± 19.5</i>	<i>75.5 ± 20.3</i>	<i>74.8 ± 14.1</i>
J0526–5026	3.5 ± 25.7	0.0 ± 25.6	1.8 ± 18.2
<i>J0542+0041</i>	<i>-5.5 ± 23.2</i>	<i>-53.7 ± 17.7</i>	<i>-35.9 ± 14.1</i>
<i>J0723+4622</i>	<i>23.4 ± 18.5</i>	<i>24.4 ± 19.1</i>	<i>23.9 ± 13.3</i>
J0808+3157	39.4 ± 18.2	33.4 ± 18.4	36.5 ± 12.9
J0811+1855	31.1 ± 21.2	22.4 ± 20.3	26.5 ± 14.6
<i>J0817–6155</i>	<i>-21.9 ± 25.7</i>	<i>-22.9 ± 18.4</i>	<i>-22.7 ± 4.9</i>
J0900+5205	4.7 ± 22.4	5.6 ± 27.9	5.1 ± 17.5
J0911+1432	15.5 ± 18.1	24.9 ± 18.5	20.1 ± 13.0
J0916–1121	-9.6 ± 18.0	-12.6 ± 18.2	-11.1 ± 12.8
<i>J0941+3315A</i>	<i>3.5 ± 17.8</i>	<i>-5.6 ± 18.2</i>	<i>-1.0 ± 12.7</i>
J0942–2551	3.5 ± 18.0	5.3 ± 18.9	4.3 ± 13.0
<i>J0948+5300</i>	<i>37.3 ± 28.7</i>	<i>33.7 ± 28.6</i>	<i>35.5 ± 20.2</i>
<i>J1036–3441</i>	<i>13.7 ± 25.2</i>	<i>-0.7 ± 25.6</i>	<i>6.6 ± 18.0</i>
J1126–2706	13.8 ± 19.0	7.7 ± 18.5	10.7 ± 13.3
J1150–2914	16.9 ± 18.4	-8.4 ± 18.7	4.5 ± 13.1
J1152+5901	-1.4 ± 19.2	7.2 ± 19.8	2.7 ± 13.8
J1158–0008	22.4 ± 25.2	21.1 ± 25.1	21.8 ± 17.8
<i>J1158+3817</i>	<i>20.0 ± 18.0</i>	<i>21.1 ± 18.2</i>	<i>20.4 ± 12.8</i>
J1212+0206	-21.5 ± 25.7	-17.6 ± 25.9	-19.5 ± 18.3
<i>J1215+0042</i>	<i>-2.8 ± 25.3</i>	<i>-9.4 ± 25.5</i>	<i>-6.1 ± 17.9</i>
<i>J1250+0455</i>	<i>13.5 ± 25.8</i>	<i>12.0 ± 28.7</i>	<i>12.9 ± 19.2</i>
J1252+0347	18.7 ± 25.2	13.1 ± 25.3	15.9 ± 17.9
J1307+0246	14.0 ± 25.1	8.6 ± 25.2	11.4 ± 17.8
J1313+1404	-21.3 ± 26.0	-60.8 ± 21.0	-45.2 ± 16.3
J1315+3232	36.0 ± 18.3	35.0 ± 18.1	35.5 ± 12.9
J1320+4238	-30.2 ± 18.0	-37.7 ± 18.3	-33.9 ± 12.9
J1420+3235	-11.7 ± 17.8	-21.6 ± 18.5	-16.4 ± 12.8
J1423+5146	35.5 ± 18.1	31.2 ± 18.2	33.4 ± 12.8
<i>J1441+4217</i>	<i>-23.5 ± 19.5</i>	<i>-24.9 ± 19.8</i>	<i>-24.2 ± 13.9</i>
J1452+0931	-12.2 ± 25.0	-8.7 ± 25.2	-10.4 ± 17.7
<i>J1514+3547</i>	<i>1.2 ± 20.3</i>	<i>15.8 ± 19.3</i>	<i>8.9 ± 14.0</i>
J1536+0646	32.9 ± 25.1	32.3 ± 25.5	32.6 ± 17.9
<i>J1544+3301</i>	<i>-16.3 ± 22.2</i>	<i>0.4 ± 24.1</i>	<i>-8.6 ± 16.3</i>
J1628–4652	-21.7 ± 25.2	-22.4 ± 25.2	-22.0 ± 17.8
J1713–3952	-34.0 ± 18.6	-44.5 ± 19.7	-39.0 ± 13.5
<i>J1737+4705</i>	<i>0.8 ± 19.4</i>	<i>-3.3 ± 18.9</i>	<i>-1.3 ± 13.6</i>
J1847–3419	-47.9 ± 20.1	-52.9 ± 24.1	-49.9 ± 15.4
J1938+4321	28.1 ± 13.9	2.5 ± 18.2	21.1 ± 12.8

8 CALCULATING RADIAL VELOCITIES

Using the PYTHON module `rvfitter`⁴ (Cooper 2022), the radial velocities of the UCDSs observed with the higher-resolution instruments (i.e. SpeX SXD and ARCoIRIS observations) can be measured with two methods: line-centring and cross-correlation.

The lines used to measure the radial velocity all lie in the *J*-band due to the shorter wavelengths having the best signal-to-noise in our observations. The lines are shown in Table 4. All measurements of

⁴ The `rvfitter` module for PYTHON is publicly available from: <https://github.com/Will-Cooper/rvfitter>

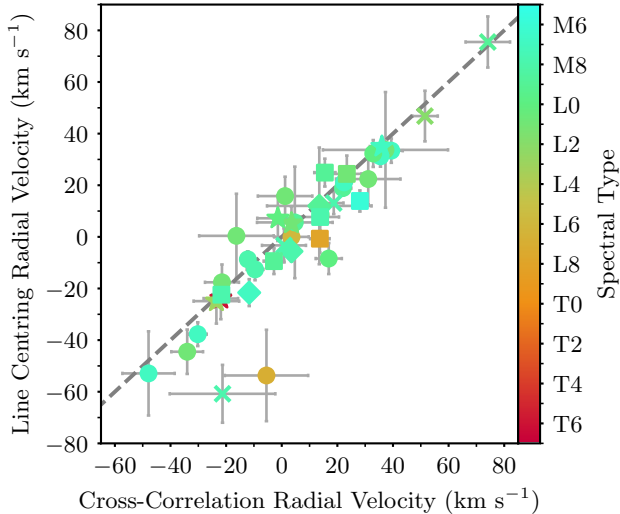


Figure 7. Comparison of line centring radial velocity and cross-correlation radial velocity measurements. The grey dashed line represents the 1:1 ratio of line centring and cross-correlation values. Colours and symbols are the same as in Fig. 5.

radial velocity used the Na I-c, Na I-d, KI-a, KI-b, KI-c and KI-d lines, while the Na I-a and Na I-b lines were only used when the signal of the spectrum was sufficient to clearly distinguish the features from the continuum (detections were deemed to be sufficient by-eye, approximating a 3σ detection). UCDs with radial velocities measured without using the Na I-a and Na I-b lines are italicised in Table 6. The line-centring routine fits a continuum to the spectrum around the spectral line, and a Gaussian is fitted to the manually-identified feature, thus giving a radial velocity measurement for each line based on its shift from its position in air (taken from the NIST Atomic Spectra Database; Kramida et al. 2023). The cross-correlation measurements are made in a similar way, finding the best-fitting radial velocity-shifted BT-Settl CIFIST spectrum by eye for each spectral line. Comparing the measured radial velocity values reveals that the two methods are generally consistent with each other (Fig. 7).

The `rvfitter` module gives an uncertainty for each of the radial velocity measurements, which is calculated using inverse variance weighting equations (see section 4.3.3 of Cooper et al. 2024). This uncertainty is added in quadrature with the median difference in order to account for systematic uncertainties, such as instrumental drift and undersampling. The median differences for the SpeX SXD and ARCoIRIS instruments are 17.7 km s^{-1} and 25.0 km s^{-1} , respectively (see Table 5 for the published radial velocities). This is comparable to the $\sim 20 \text{ km s}^{-1}$ radial velocity uncertainty associated with the typical signal-to-noise ratio of ~ 30 in our observations.

Barycentric corrections are applied to the measured radial velocities: calculating a correction factor using the `Astropy`⁵ module for `PYTHON` and adding it multiplicatively. Equation (1) shows how the correction factor is added to the radial velocity measurements; v_r is the barycentric-corrected radial velocity, v_{meas} is the measured radial velocity, v_{corr} is the correction factor and c is the speed of light in a vacuum.

⁵ The `Astropy` module for `PYTHON` is publicly available from: <https://docs.astropy.org/en/stable/install.html>

$$v_r = v_{meas} + v_{corr} + \frac{v_{meas} \cdot v_{corr}}{c} \quad (1)$$

Table 6 shows the values measured using the two methods. Overall, the values measured using the two methods are consistent with each other, with only two UCDs lying away from the 1:1 line of Figure 7. These UCDs are J0542+0041 and J1313+1404, both of which have their *J*-band spectral features hidden by noise – this is likely the cause of the inconsistencies between the radial velocity values measured using the two methods.

The radial velocity measurements presented in Table 6 can be used in Section 10 to help confirm young moving group memberships, as well as for calculating the space velocities of potential thick disc and halo objects.

9 YOUNG, THICK DISC, SUBDWARF OR BINARY?

9.1 Identification of Young Objects

The BANYAN Σ tool (Gagné et al. 2018) can be used to give a classification of young group membership for each of our UCDs. Table 12 shows the most probable classification given by BANYAN Σ for each UCD, along with the probability of the UCD being a member of the young moving group. Most of the UCDs are classified as being field objects, i.e. not likely to be a member of any of the young groups that the BANYAN Σ tool considers. The probabilities assigned by BANYAN Σ to each nearby moving group for a UCD are used to classify its membership into one of six categories based on a probability threshold. If the assigned probability exceeds 90 per cent, the UCD’s group membership is classified as Bona Fide. This classification additionally requires a strong kinematic match, complete three-dimensional velocity information, and independent indicators of youth, such as X-ray emission, lithium depletion signatures, or a position on the colour-magnitude diagram consistent with the estimated age of the moving group (see section 7 of Gagné et al. 2018 for further details). Using this threshold probability, we find seven UCDs to be likely members of young moving groups: J0942–2551, J1152+5901, J1441+4217, J1544–0435, J1544+3301, J1637+1813 and J2019+2256.

As outlined by Sarro et al. (2023), low gravity is another indicator of young objects. SPLAT can be used to determine each UCD’s gravity classification, making use of the index-based method outlined by Allers & Liu (2013): classifying the gravity of the UCD from its VO-band, FeH-bands, Na I lines, KI lines and H-band continuum indices. This Allers & Liu (2013) method was created for spectral types M5–L6, so any UCDs outside of this spectral type range do not have surface gravity classifications. A low surface gravity classification (hereafter VL-G) is associated with objects with ages ~ 10 – 30 Myr, while a classification of intermediate surface gravity (hereafter INT-G) is associated with objects with ages ~ 50 – 200 Myr. Table 12 shows the UCDs with non-field gravity classifications of INT-G and VL-G: J0900+5205, J0948+5300, J1152+5901, J1315+3232, J1544–0435, J1646–2115 and J1700–4048.

As discussed by Allers & Liu (2013), visual inspection of a UCD’s spectrum can help verify the UCD’s youth – young UCDs have a triangular *H*-band and a positive slope in the *Ks*-band. In our sample, there are two UCDs with such spectral shapes: J1243+6001 and J1544–0435. More detailed inspection of the spectra can reveal more features of youth: weak FeH bands at 0.99 , 1.20 and $1.55 \mu\text{m}$ (Allers & Liu 2013) and strong TiO features at ~ 0.78 and $\sim 0.82 \mu\text{m}$

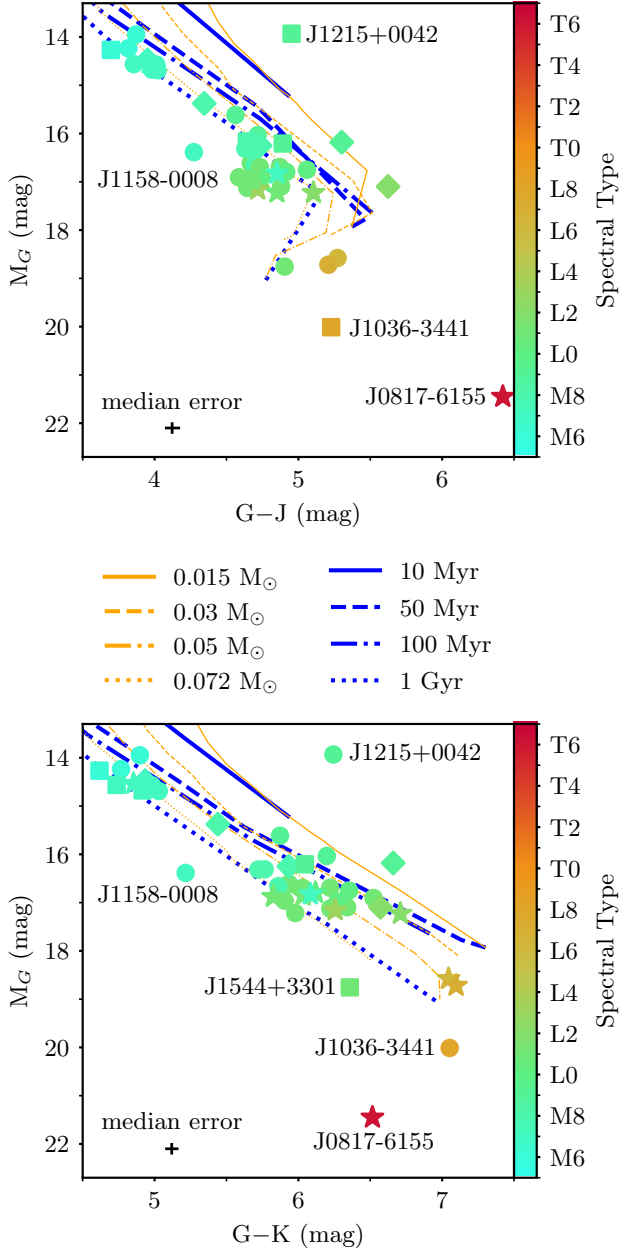


Figure 8. Top: cooling track plot showing BHAC15 mass (orange) and age (blue) relations for M_G versus $G-J$ (Baraffe et al. 2015). Bottom: cooling track plot showing BHAC15 mass (orange) and age (blue) relations for M_G versus $G-K$ s for the UCDS (Baraffe et al. 2015). The median uncertainties are plotted as error bars in the corner of each plot. Suspected thick disc and subdwarf UCDS (see Section 9.2) are not plotted, since the BHAC15 isochrones assume solar metallicities. Colours and symbols are the same as in Fig. 5.

in the J -band (McGovern et al. 2004) are indicators of very young objects, with J1544–0435 and J2019+2256 having such features.

Cooling tracks are useful tools for distinguishing stellar UCDS from sub-stellar UCDS. Using the BHAC15 isochrones from Baraffe et al. (2015), evolutionary age and mass tracks can be plotted on CMDs, showing the distribution of the UCDS across the BHAC15 models. All of the UCDS have 2MASS J -band photometry available, and only two UCDS do not have 2MASS K_s -band photometry

(J1243+6001 and J1628–4652, as mentioned in Section 5.1). There are no available BHAC15 isochrones for CatWISE2020 photometry, hence a cooling track plot for $G-W2$ (which would allow for a more comprehensive comparison with the CMDs in Fig. 5) cannot be plotted. The suspected thick disc and subdwarf objects (see Section 9.2) are not included in this plot, since the BHAC15 isochrones assume solar metallicities and we suspect these three UCDS to be located in the thick disc (see Section 9.2).

The BHAC15 isochrones are valid for temperatures ~ 2000 – 6000 K, thus cooler UCDS with later spectral types (i.e. mid-late L-dwarfs and T-dwarfs) cannot be accurately represented by the cooling tracks. Our sample is comprised primarily of late-M and early-L type UCDS, thus the BHAC15 isochrones are suitable for characterising the majority of our UCDS.

As can be seen in Fig. 8, the majority of the UCDS in this work are old and stellar in nature, while the few dim red UCDS in the lower right corners of the plots are almost certain to be sub-stellar objects. These UCDS are J0817–6155 and J1036–3441, which have late-L and T-type classifications. J1215+0042 is located above the cooling tracks in Fig. 8, suggesting that it could be an unresolved binary. J1158–0008 and J1544+3301 both lie further to the left of the isochrones than any of the other UCDS, suggesting that they may be binaries since they are more massive than would be expected based on their spectral classifications, or subdwarfs with relatively old ages. As with the UCDS highlighted in the CMDs, all of these UCDS will be investigated in more detail in Section 10.

By combining the SPLAT gravity classifications with visual inspection and positions on the cooling track plots of Fig. 8, the UCDS with convincing characteristics suggestive of youth will be investigated further in Section 10.1: J0526–5026, J0817–6155, J0942–2551, J1152+5901, J1315+3232, J1441+4217, J1544–0435, J1637+1813 and J1847–3419.

9.2 Identification of Thick Disc and Subdwarf Objects

Subdwarfs are low-metallicity Population II objects, crucial to the understanding of interior structures at the sub-stellar mass limit and star formation in the early Universe. As outlined by Zhang et al. (2017), subdwarfs include both the lowest mass metal-poor stars and brown dwarfs with subsolar metallicities. Subdwarfs can be characterised by their NIR spectral features: weak metal oxides, strong metal hydrides and enhanced collision-induced H_2 absorption (see Bates 1952; Borysow et al. 1989; Borysow 2002; Abel et al. 2012; Saumon et al. 2012; Zhang et al. 2013b, among others). Potential subdwarf objects can be identified by visually comparing each spectrum with fig. 7 from Greco et al. (2019). The old nature of subdwarfs means that they belong to the Milky Way’s thick disc and halo and can be identified by their surface gravity classification: thick disc objects and subdwarfs often have higher surface gravity than younger thin disc UCDS (Martin et al. 2017). This means that the SPLAT gravity classifications shown in Table 12 can be used to aid the identification of thick disc and subdwarf objects.

Space velocities are also an indicator of an object being located in the galactic disc. Using the criteria outlined by Nissen (2004), UCDS which are likely to be located in the thick disc ($v_{\text{tot}} > 85 \text{ km s}^{-1}$) and halo ($v_{\text{tot}} > 180 \text{ km s}^{-1}$) can be identified using their total space velocities. Our radial velocity measurements can be used to calculate UVW space velocities for the UCDS observed with the SpeX SXD and ARCoIRIS instruments, while the UCDS without radial velocity measurements have space velocities estimated by allowing their radial velocity to vary between -300 km s^{-1} and 300 km s^{-1} , as by Ravinet et al. (2024). Fig. 9 shows the positions of each UCDS on

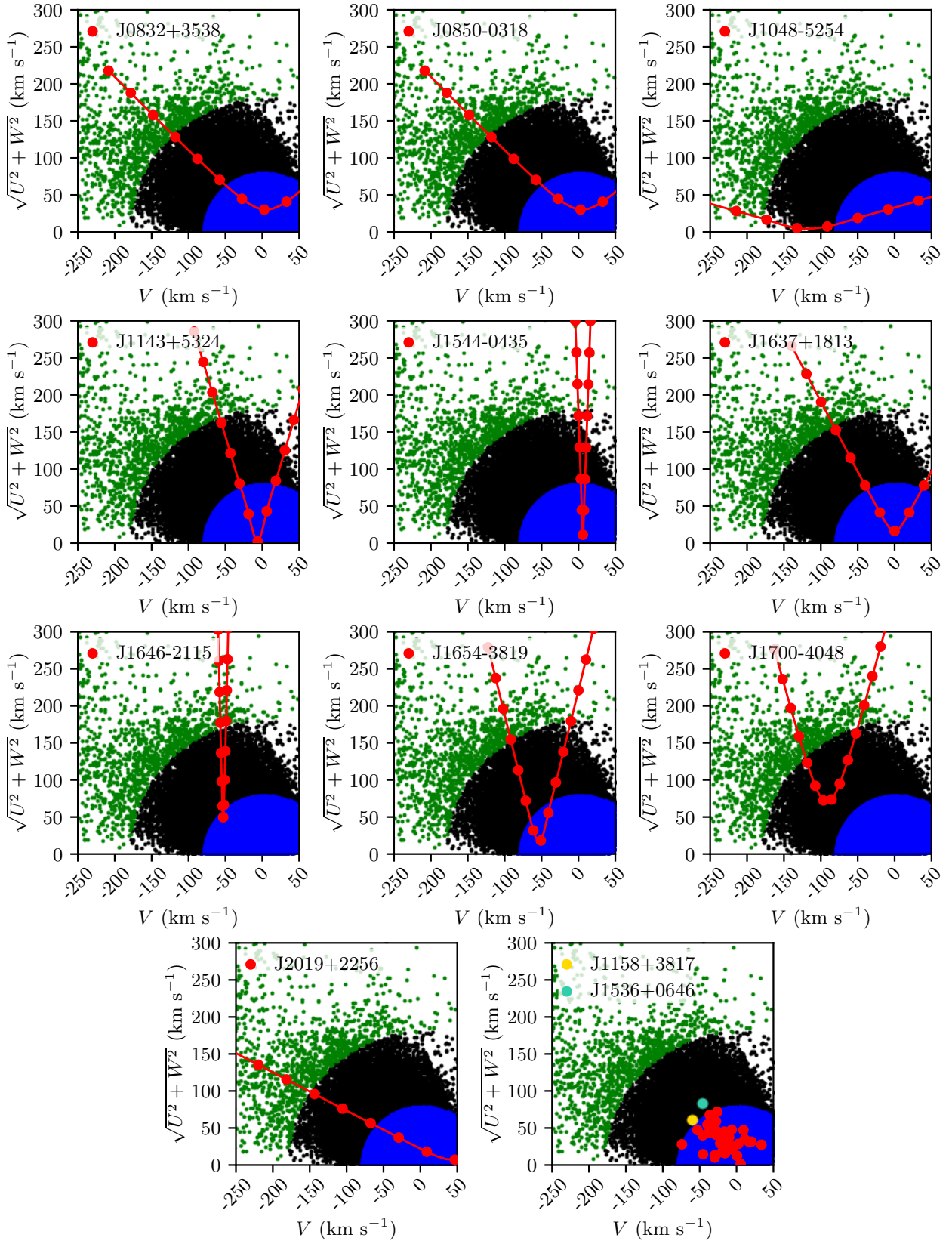


Figure 9. Toomre diagrams for our UCDs sample. UCDs without radial velocity measurements are plotted individually by allowing radial velocities between $\pm 300 \text{ km s}^{-1}$. The final panel shows the UCDs with measured radial velocities. Red objects are likely thin disc members, while other colours indicate thick disc candidates. Background sources are from GCNS: thin disc members are plotted in blue, thick disc in black and halo in green (Gaia Collaboration et al. 2021a).

a Toomre plot of the sources in the *Gaia* Catalogue of Nearby Stars (hereafter GCNS; [Gaia Collaboration et al. 2021a](#)). UCDs without radial velocity measurements are plotted individually in red; all of these UCDs have inconclusive positions on the Toomre diagram, with the exception of J1700–4048 which is likely to be a member of the thick disc or galactic halo. This is supported by the UCD’s relatively high tangential velocity ($112.75 \pm 33.82 \text{ km s}^{-1}$). Of the UCDs with radial velocity measurements, there are two which lie within the thick disc region of the Toomre diagram in Fig. 9: J1158–3817 and J1536+0646.

Using these criteria, and the positions of the UCDs on the CMDs of Fig. 5, four objects in our sample can be further investigated as being a potential thick disc UCD or subdwarf in Section 10.2: J0515+0613, J1536+0646 and J1700–4048.

9.3 Identification of Wide Binary Objects

Using the methods outlined by [Smart et al. \(2019\)](#), we found that some of the UCDs have secondary (or tertiary) associated *Gaia* objects. We used the criteria outlined by [Baig et al. \(2024\)](#) to identify systems with common proper motion, allowing for perturbations invoked by orbital motion. We also use the false positive probability equations as laid out in section 2.4.1 of [Baig et al. \(2024\)](#) to confirm the companionships of our binary systems.

The UCDs in our sample that we identify as being in wide binaries are: J0850–0318, J0941+3315A, J1243+6001, J1250+0455, J1420+3235, and J2019+2256. A summary of the UCDs and their wide companions can be found in Table 11.

9.4 Identification of Unresolved Binary Objects

The *Gaia* re-normalised unit weight error value (hereafter RUWE) can be used as an indication of whether the UCD is likely to be an unresolved binary (for a single-star source, the RUWE value is expected to be 1.0, while a significantly larger value is often an indication that the source is non-single). In this sample, we use a RUWE cut-off value of 1.2 to identify potential binary objects ([Tofflemire et al. 2021](#)). There are a handful of potential binary UCDs with RUWE values above 1.2 in our sample: J0817–6155, J1036–3441, J1126–2706 and J1423+5146. In addition, there is a brighter-than-expected UCD which may also be considered to be a potential unresolved binary candidate: J1215+0042.

[Bardalez Gagliuffi et al. \(2014\)](#) outlines a method which makes use of spectral indices to identify potential unresolved binary objects. Using the indices and selection criteria they present (Tables 9 & 10), the spectral index relations can be plotted and any potential unresolved binaries can be identified (Fig. 10). With these indices, we identified two strong candidates (which satisfy three or more of the selection criteria) and five weak candidates (which satisfy two of the selection criteria; see Table 8 for number of spectral indices satisfied by each unresolved binary candidate).

Using methods similar to those outlined by [Burgasser et al. \(2010\)](#) and [Marocco et al. \(2015\)](#), we created a set of binary template spectra from the M0–T9 standard from the library of spectral standards in the SpeX Prism Library (hereafter SPL, [Burgasser 2014](#)). Some of these standards are known to be variable or binary systems, in these cases we used alternative objects with consistent NIR and optical spectral classifications to create our templates. The objects used in the creation of our template binary spectra are presented in Table 7. We performed absolute flux calibration of the standard spectra using 2MASS *J*-band magnitudes: first

Table 7. Objects used in the creation of the template binary spectra. Objects are taken from the SPL with known variables and binaries are substituted for alternative objects.

Object	SpT
GI270	M0
IRAS F04196+2638	M1
GI91	M2
GI752A	M3
2MASS J03452021+3217223	M4
2MASS J01294256–0823580	M5
2MASS J00130931–0025521	M6
vB 8	M7
2MASS J00552554+4130184	M8
LHS 2924	M9
2MUCD 20165	L0
SIPS J2130–0845	L1
2MASS J00062250+1300451	L2
2MASSW J1506544+132106	L3
2MASS J21580457–1550098	L4
SDSS J083506.16+195304.4	L5
2MASS J1010148–040649	L6
SDSS J104409.43+042937.6	L7
2MASSW J1632291+190441	L8
2MASS J02550357–4700509	L9
2MASS J00164364+2304262	T0
SDSSp J083717.22–000018.3	T1
WISE J045746.08–020719.2	T2
2MASS J01383648–0322181	T3
2MASS J08195820–0335266	T4
2MASS J00454267+3611406	T5
SDSSp J162414.37+002915.6	T6
2MASS J0727182+171001	T7
2MASS J0415195–093506	T8
UGPS J072227.51–054031.2	T9

interpolating the 2MASS *J*-band filter curve to match each standard UCD spectrum and calculating a weighted flux before integrating under the filter curve to give the new absolute-calibrated standard spectra. We then combined these standard spectra to create our binary templates.

By performing a chi-squared fit of the template binary spectra to the spectra of the UCDs, we can find the most probable combination of objects which make up the unresolved binary system. We perform our fits using the wavelengths 0.9–1.35 μm , 1.45–1.8 μm and 2.0–2.35 μm in order to avoid noise introduced by water bands. The chi-squared values of the binary template fits are shown in Table 8.

We also calculated a one-sided F-test for each unresolved binary candidate following the method presented by [Burgasser et al. \(2010\)](#). Equation (2) is the distribution statistic, where we assume $\nu_{\text{single}} = \nu_{\text{binary}} = \nu$, and we take ν to be the number of data points used in the chi-squared fit minus one (as in [Burgasser et al. 2010](#)). In order to achieve a 90 per cent confidence level in the binary fit, we require $\eta_{\text{SB}} > 1.1$. The values of η_{SB} are presented in Table 8.

$$\eta_{\text{SB}} = \frac{\chi_{\text{single,min}}^2 / \nu_{\text{single}}}{\chi_{\text{binary,min}}^2 / \nu_{\text{binary}}} \quad (2)$$

The potential binarity of each of these unresolved binary candidates is investigated in Section 10.4.

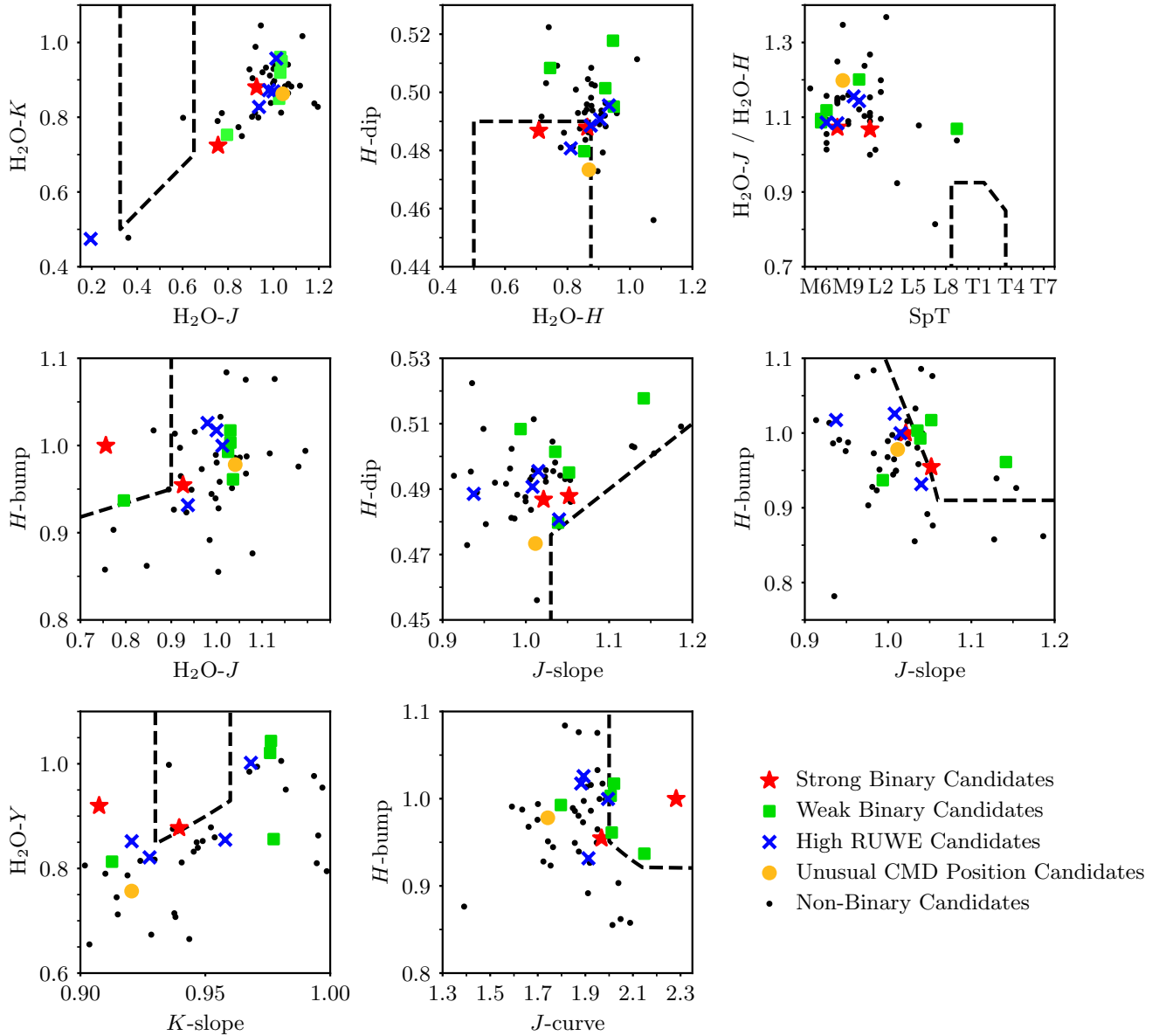


Figure 10. Spectral index relations for unresolved binary candidate selection. Dashed lines indicate the selection areas, red stars \star indicate strong objects and green squares \blacksquare indicate weak objects. Blue crosses \times denote objects with high RUWE values, and yellow circles \bullet are objects with unusual positions on the CMDs of Fig. 5.

10 ANALYSIS OF SPECIFIC OBJECTS

Most UCDs in our sample have RUWE values < 1.2 and $v_{\text{tan}} < 85 \text{ km s}^{-1}$, typical of solo objects located in the thin disc, however some UCDs can be discussed in a little more detail; here we look at the UCDs which have been identified as being interesting in Sections 4–9, mainly by considering their BANYAN Σ classification, SPLAT gravity classification, spectral features, RUWE and tangential and radial velocities. By systematically inspecting various features (summarised in Table 12) the characteristics of these UCDs can be determined. The majority of the UCDs have field BANYAN Σ and SPLAT gravity classifications, with spectral shapes and features typical of their spectral types.

10.1 Potentially Young Objects

10.1.1 J0526–5026 (L6)

J0526–5026 has a fairly prominent CO feature at $\sim 2.3 \mu\text{m}$, suggesting that it could have high metallicity. Performing a chi-squared fitting of the Witte et al. (2011) models at the effective temperature value determined in Section 7, the metallicity of J0526–5026 is estimated to be $[M/H] = +0.3$ dex. The spectroscopic classification of L6 is also notably different from the photometric spectral type of L8, suggesting that the UCD is fainter and redder than would typically be expected of a L6-type UCD. The high metallicity, along with the weak FeH lines in the J -band and spectral classification differences, suggest that J0526–5026 is likely to be a young UCD, although the field surface gravity classification and photometric faintness suggests that youth is unlikely. The

Table 8. Unresolved binary candidates from index-based selection, objects with RUWE values > 1.2 , and objects with unusual CMD positions.

Object Short Name	Single SpT	N ^o of Index Criteria	Best-fitting Binary	Binary χ^2 Value	η_{SB} Value
Strong Candidates					
J1544+3301	L2	3	L0 + L2	2.253	0.744
J1628-4652	M8	3	M9 + L9	3.720	1.133
Weak Candidates					
J0832+3538	M6	2	M6 + L6	7.479	0.302
J0911+1432	M9	2	M8 + L3	2.445	1.076
J1036-3441	L8	2	L5 + T1	1.676	1.875
J1320+4238	M7	2	M6 + M7	3.263	1.025
J1938+5146	M6	2	M7 + M9	3.512	0.839
High RUWE Objects					
J0723+4622	L1	1	M8 + L7	1.574	2.229
J0817-6155	T6	1	T0 + T6	9.142	0.115
J1126-2706	M8	0	M8 + L1	1.073	1.244
J1423+5146	M7	0	M6 + M7	4.494	0.974
J1536+0646	L0	1	L1 + T4	2.048	0.550
Unusual CMD Position Objects					
J1215+0042	M9	1	M8 + L9	3.601	1.022

TiO features in the *J*-band are also weak, further suggesting that J0526-5026 is not a young UCD. Ultimately, it is unlikely that this is a young UCD, and further studies will be required to determine the cause of the discrepancy between the spectroscopic and photometric spectral type classifications.

10.1.2 J0942-2551 (L1)

J0942-2551 is classified as likely being a member of the Carina-Near moving group by the BANYAN Σ tool, with a probability of 0.939. Carina-Near is a group of co-moving stellar objects with ages of ~ 200 Myr at a distance of around 30 ± 20 pc (Zuckerman et al. 2006; Gagné et al. 2018), which is consistent with the distance of J0942-2551. Using the measured radial velocity of 4.3 ± 13.0 km s⁻¹, we calculate the space velocity of J0942-2551 to be $U = -21.8$ km s⁻¹, $V = -4.4$ km s⁻¹, $W = -11.3$ km s⁻¹. This is somewhat similar to the average space velocity of the Carina-Near moving group as defined by Zuckerman et al. (2006) ($U = -25.9$ km s⁻¹, $V = -18.1$ km s⁻¹, $W = -2.3$ km s⁻¹), so it is likely that J0942-2551 is a member of the young moving group.

We identify *Gaia* DR3 5661603972370860800 as a potential wide companion to J0942-2551, however a calculation of the false positive probability yields a value of 0.939, thus it is unlikely that this is a wide binary.

10.1.3 J1152+5901 (L0)

J1152+5901 is classified as a member of the Crius 198 moving group by the BANYAN Σ tool, with a probability of 0.983. Crius 198 is a young moving group at an average distance of around 47 pc and an age of 100-700 Myr (Moranta et al. 2022). J1152+5901 has a parallactic distance of 53.7 ± 2.1 pc, so it is reasonable that it could be part of the Crius 198 group. Using our measured radial velocity of 2.7 ± 13.8 km s⁻¹, we can calculate the space velocity

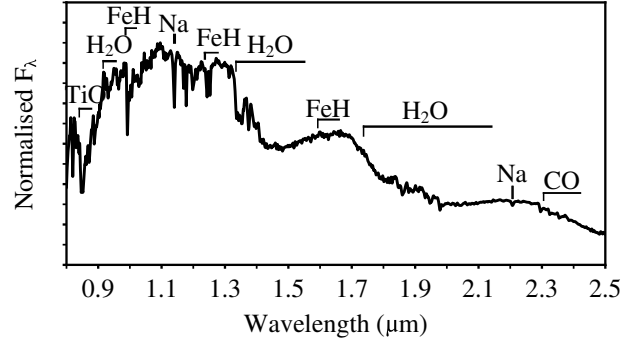


Figure 11. Spectrum of J1315+3232 with key spectral features labelled. Note the shallow *J*-band FeH features and strong TiO lines – a telltale sign of youth in UCDS.

of J1152+5901: $U = -33.6$ km s⁻¹, $V = -12.9$ km s⁻¹, $W = -7.0$ km s⁻¹. Moranta et al. (2022) defines the average space velocity of the Crius 198 group as $U = -34.3$ km s⁻¹, $V = -12.9$ km s⁻¹, $W = -11.0$ km s⁻¹. BANYAN Σ uses multiple input parameters to determine young moving group memberships, thus the discrepancy between the *W*-components of the space velocities is minor in comparison to the agreement between the other parameters, and we can consider J1152+5901 to be a member of the Crius 198 young moving group.

10.1.4 J1315+3232 (M7)

J1315+3232 has a surface gravity classification of INT-G, with fairly weak FeH lines and relatively strong TiO features in the *J*-band, suggesting that it could be a young UCD. Its tangential velocity of 11.702 ± 0.04 km s⁻¹ is consistent with J1315+3232 being young, as is its radial velocity of 35.5 ± 12.9 km s⁻¹. Using this radial velocity measurement, we calculate the space velocities of J1315+3232 to be: $U = 6.8$ km s⁻¹, $V = -14.5$ km s⁻¹, $W = -43.8$ km s⁻¹. These low space velocity values place the UCD in the thin disc region of the Toomre diagram of Fig. 9, further supporting the theory that J1315+3232 may be a young UCD. J1315+3232 has only been previously published as a potential UCD by Reylé (2018).

10.1.5 J1441+4217 (L3)

The BANYAN Σ tool identifies J1441+4217 as being a likely member of the Crius 198 moving group, which is consistent with its distance of 45.3 ± 1.3 pc (the Crius 198 group has an average distance of ~ 47 pc; Moranta et al. 2022). The radial velocity of J1441+4217 is measured to be -24.2 ± 13.9 km s⁻¹, which can be used to calculate the UCD's space velocity ($U = -35.2$ km s⁻¹, $V = -11.5$ km s⁻¹, $W = -5.6$ km s⁻¹). This space velocity is very similar to that of the Crius 198 moving group ($U = -34.3$ km s⁻¹, $V = -12.9$ km s⁻¹, $W = -11.0$ km s⁻¹; Moranta et al. 2022). Only the surface gravity classification of FLD-G suggests that J1441+4217 is not a young UCD, though the 100-700 Myr age of the Crius 198 group (Moranta et al. 2022) means that a FLD-G gravity classification is plausible for a member of this group (similar to some of the surface gravity classifications of the sample presented by Manjavacas et al. 2019).

Table 9. Spectral indices used for identification of potential unresolved binary objects.

Spectral Index	Numerator Range (μm)	Denominator Range (μm)	Spectral Feature	Reference
H ₂ O- <i>Y</i>	1.04–1.07	1.14–1.17	1.15 μm H ₂ O	1
H ₂ O- <i>J</i>	1.14–1.165	1.26–1.285	1.15 μm H ₂ O	2
H ₂ O- <i>H</i>	1.48–1.52	1.56–1.60	1.4 μm H ₂ O	2
H ₂ O- <i>K</i>	1.975–1.995	2.08–2.10	1.9 μm H ₂ O	2
<i>K</i> / <i>J</i>	2.06–2.10	1.25–1.29	<i>J</i> - <i>K</i> colour	2
<i>J</i> -slope	1.27–1.30	1.30–1.33	1.28 μm flux peak shape	1
<i>J</i> -curve	1.04–1.07 + 1.26–1.29 ^a	1.14–1.17	Curvature across <i>J</i> -band	1
<i>H</i> -bump	1.54–1.57	1.66–1.69	Slope across <i>H</i> -band peak	1
<i>H</i> -dip	1.61–1.64	1.56–1.59 + 1.66–1.69 ^a	1.634 μm FeH/CH ₄	3
<i>K</i> -slope	2.06–2.10	2.10–2.14	<i>K</i> -band shape/CIA H ₂	4

Notes ^a – Average of the two wavelength ranges

References 1 – Bardalez Gagliuffi et al. (2014) 2 – Burgasser et al. (2006) 3 – Burgasser et al. (2010) 4 – Burgasser et al. (2002)

Table 10. Selection criteria used for identification of potential unresolved binary objects in different parameter spaces.

Abcissa (<i>x</i>)	Ordinate (<i>y</i>)	Limits	N ^o Sources
H ₂ O- <i>J</i>	H ₂ O- <i>K</i>	Intersection of: $y = 0.615x + 0.3$, $x = 0.325$ and $x = 0.65$ Select points in upper middle	1
H ₂ O- <i>H</i>	<i>H</i> -dip	Intersection of: $y = 0.49$, $x = 0.5$ and $x = 0.875$ Select points in lower middle	12
SpT	H ₂ O- <i>J</i> /H ₂ O- <i>H</i>	Intersection of: $y = 0.95$, $y = -0.0375x + 1.731$, $x = \text{L}8.5$ and $x = \text{T}3.5$ Where L0 = 10, T0 = 20 etc. Select points in lower middle	0
H ₂ O- <i>J</i>	<i>H</i> -bump	Intersection of: $y = 0.16x + 0.806$ and $x = 0.90$ Select points in upper left corner	4
<i>J</i> -slope	<i>H</i> -dip	Intersection of: $y = 0.20x + 0.27$ and $x = 1.03$ Select points in lower right corner	0
<i>J</i> -slope	<i>H</i> -bump	Intersection of: $y = -2.75x + 3.84$ and $y = 0.91$ Select points in upper right corner	12
<i>K</i> -slope	H ₂ O- <i>Y</i>	Intersection of: $y = 12.036x^2 - 20.000x + 8.973$, $x = 0.93$ and $x = 0.96$; $\sigma = 0.064$ Select points above 1σ curve in upper middle	3
<i>J</i> -curve	<i>H</i> -bump	Intersection of: $y = 0.269x^2 - 1.326x + 2.479$, $y = 2.00$ and $x = 0.92$; $\sigma = 0.048$ Select points above 1σ curve in upper right corner	6

10.1.6 J1544–0435 (L1)

The BANYAN Σ tool classifies J1544–0435 as likely to be a member of the Ursa Major Corona, the peripheral regions of the Ursa Major moving group. The Ursa Major group has an average distance of $25.4^{+0.8}_{-0.7}$ pc and an average age of 414 Myr (Jones et al. 2015; Gagné et al. 2018). J1544–0435 has a distance of 52.0 ± 3.8 pc, so it is unlikely that it is a member of the core of this young moving group, however it is plausible that it could be a member of the extended Ursa Major Corona, as suggested by the BANYAN Σ tool. We did not measure the radial velocity of J1544–0435 since it was observed with the SpeX prism configuration, however estimating space velocities by allowing radial velocities between $\pm 300 \text{ km s}^{-1}$ suggests that it is likely to be located in the thin disc (see Fig. 9), consistent with being a younger UCD.

10.1.7 J1637+1813 (M7)

J1637+1813 has TiO features which are deeper than usual for an M7-type UCD, suggesting that this could be a young UCD. Its tangential velocity is $16.132 \pm 0.59 \text{ km s}^{-1}$, consistent with J1637+1813 being a young UCD. The BANYAN Σ tool identifies J1637+1813 as being a member of the Ursa Major Corona. Dopcke et al. (2019) outlines that the kinematics of the extended Ursa Major Corona suggests that the members of the extended group are found

over a wider range of distances than the core of the moving group (which has a distance of $25.4^{+0.8}_{-0.7}$ pc; Gagné et al. 2018). J1637+1813 has a distance of 49.8 ± 1.7 pc, so it is possible that it is a member of the Ursa Major Corona, though we do not deem it to be a young UCD. Reylé (2018) lists J1637+1813 as a UCD.

10.1.8 J1847–3419 (M7)

J1847–3419 is classified as being a potential member of the Ursa Major moving group by the BANYAN Σ tool, and the moving group's distance is consistent with the UCD's distance of 27.1 ± 0.1 pc. The radial velocity of J1847–3419 is measured to be $-49.9 \pm 15.4 \text{ km s}^{-1}$, which is a much larger radial velocity than that of the Ursa Major Corona stars (Chupina et al. 2006), hence it is unlikely that J1847–3419 is a member of the young moving group. Since the BANYAN Σ classification is the only indicator of youth for this UCD, it is most likely that J1847–3419 is not a young UCD.

10.2 Thick Disc and Subdwarf Objects

10.2.1 J0515+0613 (M9)

J0515+0613 has a measured radial velocity of $74.8 \pm 14.1 \text{ km s}^{-1}$, thus we can calculate the space velocity of J0515+0613 to be $U = -86.0 \text{ km s}^{-1}$, $V = -42.1 \text{ km s}^{-1}$, $W = -25.7 \text{ km s}^{-1}$. Plotting the

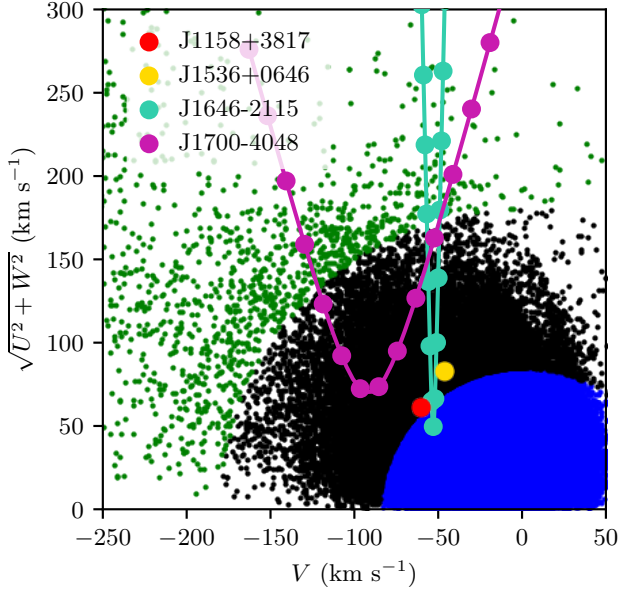


Figure 12. Toomre diagram showing potential thick disc and subdwarf UCDs identified in Section 9.2. Curves for UCDs without measured radial velocities assume radial velocities between $\pm 300 \text{ km s}^{-1}$ with markers plotted at intervals of 50 km s^{-1} . Background points are stars taken from GCNS with known radial velocities (Gaia Collaboration et al. 2021a). Blue points are thin disc stars, black are thick disc and green are halo stars.

position of J0515+0613 on a Toomre diagram reveals that, based on its space velocities, J0515+0613 is likely to be a member of the thick disc (Fig. 12). There are no other indications of J0515+06713 being a subdwarf, so overall, it is likely that J0515+0613 is simply a normal UCD located in the thick disc.

10.2.2 J1646–2115 (sdL2)

J1646–2115 has a best-fitting SPLAT spectral type of L0, however its photometric spectral type and position on the CMDs in Fig. 5 indicate that it has a spectral classification of L2. Visual inspection of the spectrum compared to the SPLAT L2 and T0 standards show that the spectrum is more similar to that of the L2 UCD. There are, however, deviations from the standard in the spectrum of J1646–2115 which suggest that it may be a subdwarf.

Fig. 13 shows a comparison of the spectrum of J1646–2115 with that of our adopted L2 standard, 2MASS J00062250+1300451. As is evident from this comparative plot, J1646–2115 is fainter and bluer in the *H* and *K*-bands, and has stronger FeH features in the *J*-band. The lack of CH_4 features at $1.6 \mu\text{m}$ and $2.2 \mu\text{m}$ can also be seen in the plot. This plot looks remarkably similar to that of *WISE* J1013–7246 in the top plot of fig. 67 by Kirkpatrick et al. (2016), furthering that J1646–2115 is a sdL2-type object.

The photometry for J1646–2115 is typical of a L2-type UCD, and the UCD’s position on the CMDs does not suggest that it is a subdwarf. The position of J1646–2115 on the Toomre diagram of Fig. 12 shows that it is likely to be a thick disc or halo object, although the range of potential space velocity values extends into the thin disc region, so thick disc membership cannot be confirmed using this method.

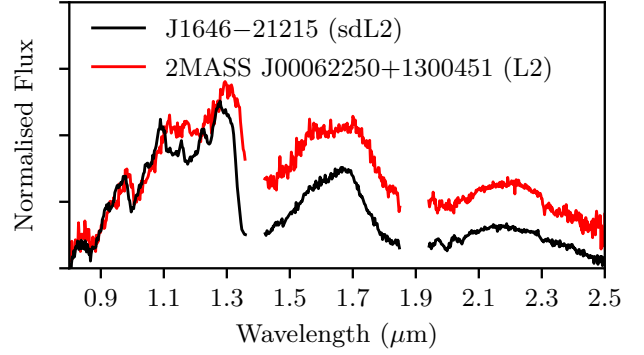


Figure 13. Spectrum of J1646–2115 compared with that of 2MASS J00062250+1300451, the L2-type UCD which we have adopted for use as the class standard in this work. Our UCD’s spectrum is clearly dimmer in the *H* and *K*-bands, and shows a lack of CH_4 features and strong FeH features, characteristic of a subdwarf.

10.2.3 J1700–4048 (L4)

J1700–4048 has a SPLAT surface gravity classification of VL-G, but its spectrum is too noisy to identify any spectral shapes indicative of young UCDs, and the poor signal-to-noise of our spectrum means that the VL-G surface gravity classification should not be taken as definite. The tangential velocity of J1700–4048 is $112.745 \pm 33.819 \text{ km s}^{-1}$, and plotting a Toomre diagram using radial velocities varying between $\pm 300 \text{ km s}^{-1}$ shows that J1700–4048 is likely to be a thick disc object (Fig. 12). It has the faintest absolute *Gaia* *G*-band magnitude (M_G) of any of the UCDs in our sample (27.763 ± 0.650), suggesting that it may be a subdwarf. Overall, J1700–4048 is likely to be located within the thick disc, but further spectroscopic observations will be required to confirm whether it is a subdwarf. J1700–4048 has not been included in any previous publications.

10.3 Wide Binary Objects

10.3.1 J0850–0318 (M8) + SCR J0850–0318 (M1)

As outlined in Section 9.3, the methods defined by Smart et al. (2019) were used to identify potential wide companions for the UCDs. J0850–0318 was identified to have a wide companion: SCR J0850–0318, at a separation of 8.84 arcsec (a projected separation of 310.9 AU at the distance of the UCD). SCR J0850–0318 is a well-characterised M1 star published by Gaidos et al. (2014), with an effective temperature of $3881 \pm 78 \text{ K}$, radius of $0.56 \pm 0.04 R_\odot$ and mass of $0.60 \pm 0.07 M_\odot$.

This system is included in the Ultracool Dwarf Binary Catalogue (hereafter UCDC; Baig et al. 2024), where J0850–0318 and SCR J0850–0318 are confirmed to be a binary system with reasonable projected separations, comparable parallaxes and common proper motion. The system has a false positive probability of 3.68×10^{-8} , confirming the companionship of the system.

10.3.2 J0941+3315A (M8) + J0941+3315B (M5)

J0941+3315A is identified as a companion to J0941+3315B. Both of these objects were observed for this work, and J0941+3315B is omitted from the UCD sample since we determine it to have an M5 spectral classification (see Appendix B). The J0941+3315AB system is not included in the UCDC, however using the criteria

Table 11. Key information about the UCDCs in wide binary systems, including the companion object spectral type (if available) and false positive probability, as calculated following the method outlined by Baig et al. (2024). Some UCDCs have more than one wide companion.

UCD Short Name	Spectral Type	Companion <i>Gaia</i> DR3 ID	Companion SpT	Separation (arcsec)	Projected Separation (AU)	False Positive Probability
J0850–0318	M8	5762038930729097728	M1 ^[1]	8.84	310.9	3.86×10^{-8}
J0941+3315A	M8	794031395950867968	M5 ^[2]	7.34	242.0	5.17×10^{-10}
J1243+6001	L7	1579929906250111232	K0 ^[3]	35.19	–	2.92×10^{-14}
J1250+0455	M9	3705763723623026304	–	10.45	449.92	6.90×10^{-7}
J1420+3235	M7	1477880761742899456	–	129.87	286.76	3.69×10^{-5}
J2019+2256	L2	1829571684890816384	M3 + M0 ^[4]	11.02	324.7	5.70×10^{-8}
		1829571684890816512	M3.5 ^[4]	9.84	289.9	

References ^[1] – Gaidos et al. (2014) ^[2] – This work (see Appendix B2) ^[3] – Faherty et al. (2021) ^[4] – Cifuentes et al. (2021)

from Baig et al. (2024) we find the pair to have appropriate projected separation, and consistent parallaxes and proper motions. Using the equations outlined by Baig et al. (2024), we calculate the false positive probability for this system to be 5.17×10^{-10} , confirming the companionship of this binary. Seli et al. (2021) identifies J0941+3315AB as a co-moving pair, with J0941+3315A being listed as one of their TRAPPIST-1 analogue systems.

10.3.3 J1243+6001 (L7) + BD+60 1417 (K0)

J1243+6001 only has limiting magnitudes in *Gaia* and 2MASS photometry, so is not plotted on the CMDs in Fig. 5 or the cooling track plots in Fig. 8. The SPLAT surface gravity tool gives a classification of VL–G, and visual inspection of the spectrum reveals a triangular *H*-band and positive slope in the *K*-band, indicating that this is likely to be a young UCD. Performing a chi-squared fit of the Witte et al. (2011) models at $T_{\text{eff}} = 1600$ K and $\log(g) = 5.0$ dex reveals a best-fitting metallicity of $[M/H] = +0.3$ dex. This is consistent with J1243+6001 being a young UCD. Faherty et al. (2021) also conclude that J1243+6001 is a young UCD, with an estimated age of 10–150 Myr.

J1243+6001 is also identified as a wide companion to BD+60 1417, which has been previously published by Faherty et al. (2021) and Calamari et al. (2024). The system is not published in the UCDC, although this is likely due to the lack of *Gaia* detection for J1243+6001. Our calculated spectrophotometric distance (43.5 ± 12.3 pc) is consistent with the parallactic distance of BD+60 1417 (45.0 ± 0.0 pc, based on its *Gaia* DR3 parallax measurement). Calculating a false positive probability for this pair in the same way as Baig et al. (2024), we find a false positive probability value of 2.92×10^{-14} , thus confirming the companionship of the system.

10.3.4 J1250+0455 (M9) + *Gaia* DR3 3705763723623026304

J1250+0455 has a RUWE value of 1.5097 – the highest RUWE value for any UCD within the sample in this work. J1250+0455 is included in the list of L-dwarfs by Skrzypek et al. (2015), with a photometric classification of L1. The discrepancy between the photometric and spectroscopic classifications is reflected in the position of J1250+0455 on the CMDs and cooling tracks: the UCD is unusually red for an UCD of its spectral type (Fig. 5 & 8). In addition to the redness in the photometry, the spectrum of J1250+0455 also displays suggestions that there may be hidden companion, since there are strong H₂O features at $\sim 0.9 \mu\text{m}$ and $\sim 1.1 \mu\text{m}$ and weak FeH features at $\sim 1.0 \mu\text{m}$ and $\sim 1.2 \mu\text{m}$. Baig et al. (sub.) resolve this UCD as a binary.

Our methods also identify *Gaia* DR3 3705763723623026304 as

a wide companion to J1250+0455, at a separation of 10.45 arcsec (a projected separation of 449.92 AU at the distance of the UCD). Baig et al. (2024) includes J1250+0455 in the UCDC, as a wide binary with *Gaia* DR3 3705763723623026304, and also identifies the UCD as having a potential hidden companion using blended photometry methods (see section 3.2 of their paper). As with J0850–0318, the inclusion of J1250+0455 in the UCDC means that the binary has a sensible projected separation and consistent parallaxes and proper motions, thus confirming the companionship of the pair.

10.3.5 J1420+3235 (M7) + *Gaia* DR3 1477880761742899456

J1420+3235 is identified to have one potential wide companion: *Gaia* DR3 1477880761742899456, an M-dwarf identified by Morrell & Naylor (2019). The two objects are separated by 129.87 arcsec, corresponding to a projected separation of 286.76 AU at the distance of the UCD. J1420+3235 is included in the UCDC, meaning that the projected separation of the components is reasonable, and there is common proper motion and consistent parallaxes between the two objects, thus confirming the binarity.

Some of the properties of *Gaia* DR3 1477880761742899456 are estimated by Morrell & Naylor (2019): $T_{\text{eff}} = 3500$ K, $\log(g) = 5.5$ dex, $R = 0.43 R_{\odot}$. These values have a poor goodness of fit from their model-fitting methods, so further observations of this pair will be required to confirm their properties.

10.3.6 J2019+2256 (L2) + LP 395-8 AB (M3 + M0 + M3.5)

J2019+2256 is identified to have two wide companions: LP 395-8 A and LP 395-8 B. LP 395-8 B is a known M3.5-type companion to the M-dwarf binary system comprised of LP 395-8 Aa and LP 395-8 Ab (M3 and M0 types respectively; Cifuentes et al. 2021). J2019+2256 is identified by Cifuentes et al. (2021) as a M9-type companion to the hierarchical triple system, listing the UCD as LP 395-8 C in their table 1. Fig. 14 shows a diagram depicting the Cifuentes et al. (2021) description of the hierarchical nature of the system.

The J2019+2256 + LP 395-8 AB system is also listed in the UCDC. This verifies that the system has reasonable projected separation, consistent parallaxes and common proper motion. Baig et al. (2024) gives a false positive probability of 5.70×10^{-8} , confirming the membership of J2019+2256 in this hierarchical system.

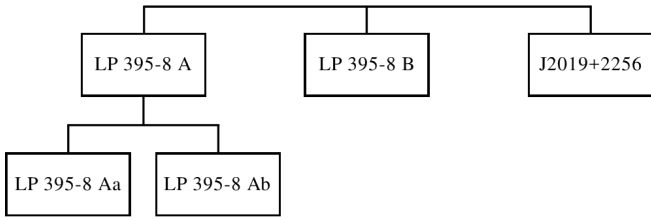


Figure 14. Diagram showing the hierarchical structure of the J2019+2256 + LP 395-8 AB system described by (Cifuentes et al. 2021).

10.4 Unresolved Binary Objects

10.4.1 J0723+4622 (M8 + L7)

J0723+4622 has a *Gaia* RUWE value of 1.2470, which suggests that this is likely to be a binary object; although there were no Image Parameters Determination (hereafter IPD) windows with more than one peak (a double peak means that the detection may be a resolved double star, i.e. a visual double or real binary), so it most likely that this is an unresolved binary.

J0723+4622 only satisfies one of the spectral index criteria laid out in Section 9.4, but its spectrophotometric distance suggests that it is over-luminous for a single L1-type UCD (the parallactic distance is 55.8 ± 4.5 pc and the spectrophotometric distance is 74.9 ± 3.8 pc). The significant difference in the parallactic and spectrophotometric distance values suggests that it may not be a single source. A chi-squared fitting of the binary spectra created using the library of standard spectra included in SPLAT reveals the best-fitting binary to be one with M8 and L7 components. Plotting this binary template spectrum over the spectrum of J0723+4622 shows that the binary spectrum is more closely matched with the UCD spectrum (Fig. 15), and the η_{SB} value is 2.229, consistent with a > 90 per cent confidence that this spectrum is better-fitted by a binary template. This is consistent with the over-luminosity suggested by the spectrophotometric distance, thus J0723+4622 is likely to be an unresolved binary with M8 and L7-type components.

10.4.2 J0817–6155 (T6)

J0817–6155 lies in the region of the CMDs which would be expected for a sub-stellar object. Its RUWE value is 1.2429, so it is possible that this is a binary object, although the spectral index criteria do not suggest that J0817–6155 is an unresolved binary. A chi-squared fit of the binary template spectra gives a best-fitting binary with T0 and T6 components. The η_{SB} value of 0.115 means that we can safely conclude the single-source spectral fit is better than the binary, which is consistent with a by-eye comparison of the spectral fits (Fig. 15), so it is mostly likely that J0817–6155 is a single UCD.

The sub-stellar nature of J0817–6155 is furthered by the SPLAT surface gravity classification of INT-G. The *Gaia* DR3 tangential velocity of 27.437 ± 0.062 km s⁻¹ and our measured radial velocity of -22.9 ± 18.4 km s⁻¹ are also consistent with J0817–6155 being a young object. This UCD has been included in a number of works: Kiman et al. (2019); Schneider et al. (2016); Kirkpatrick et al. (2011). J0817–6155 is discussed in detail by Artigau et al. (2010), and our findings largely agree with theirs.

10.4.3 J0832+3538 (M6)

J0832+3538 is identified as a weak unresolved binary candidate using the spectral index criteria, with the best-fitting binary template being that of an M6 + L6 binary. The η_{SB} value is 0.302, thus the single-source spectrum can be deemed a better fit than that of the binary. When comparing the two spectral fits by-eye, the single-source spectrum matches the spectrum of J0832+3538 more closely than the binary spectrum, furthering that J0832+3538 is a single UCD. The spectrophotometric distance is similar to the parallactic distance (26.8 ± 0.4 pc and 30.9 ± 0.1 pc respectively), so it is most likely that it is a single M6-type UCD.

10.4.4 J0911+1432 (M8 + L3)

J0911+1432 is a strong unresolved binary candidate based on the spectral index criteria. The best-fitting binary template spectrum is that of a M8 + L3 binary, and when compared by-eye to the spectrum of J0911+1432, as shown in Fig. 15, the binary spectrum is more similar than that of the M9 standard (J0911+1432 was spectroscopically classified as a M9-type UCD in Section 3.1). This is reflected by the η_{SB} value of 1.076, which is consistent with an 80 percent confidence of it being a binary. The possibility of J0911+1432 being an unresolved binary is further supported by the discrepancy between the parallactic distance (67.1 ± 3.3 pc) and spectrophotometric distance (58.5 ± 1.7 pc). This means that it is likely that J0911+1432 is an unresolved binary with M8 and L3 constituent components, rather than a single M9-type UCD.

10.4.5 J1036–3441 (L5 + T1)

J1036–3441 has a RUWE value of 1.2900, meaning that is likely that this could be a binary object. There are no potential wide companions, so this is likely to be an unresolved binary, a possibility supported by the 3–subtype difference in optical and NIR spectral classifications. The spectral index criteria in Section 9.4 indicate that J1036–3441 is a weak binary candidate, and it was published by Bardalez Gagliuffi et al. (2014) as a weak binary candidate with a best-fitting binary spectrum composed of L5 + T1.5 components.

Comparing the L5 + T1 template binary and single-source spectra to that of J1036–3441 by-eye reveals that the binary spectrum better matches the spectrum of the UCD, so it is likely that it is an unresolved binary UCD (Fig. 15). This is supported by the η_{SB} value of 1.875, which corresponds to a > 90 per cent confidence that the binary spectral fit is better than that of the single-UCD spectrum.

J1036–3441 has been previously published as a high proper motion object by Schneider et al. (2016). It has also been published as a UCD by Gizis (2002), with a spectral classification of L6.

10.4.6 J1126–2706 (M8 + L1)

J1126–2706 has a RUWE value of 1.3152, so it is likely to be a binary. Its spectral indices do not suggest that it is an unresolved binary, but there are also no potential wide companions. A chi-squared fit suggests that J1126–2706 could be a M8 + L1 binary, and comparing the spectrum of J1126–2706 with the binary and standard spectra by-eye reveals that the binary spectrum matches that of the UCD more closely in the *J*-band, although the spectral types comprising the binary template are similar so the differences between the spectra are minimal. The η_{SB} value of 1.244 gives a > 90 per cent confidence that the binary template is a better spectral fit for J1126–2706.

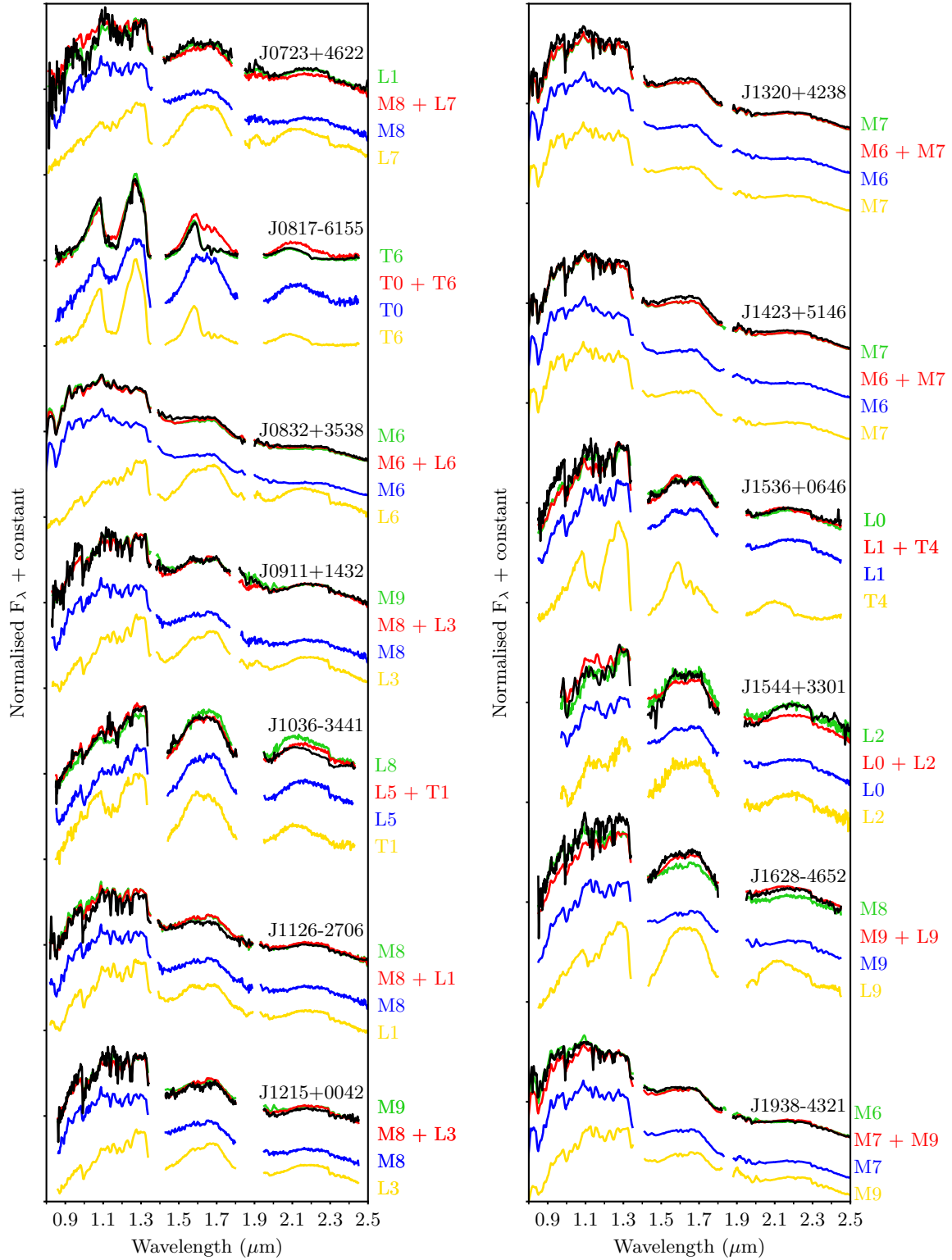


Figure 15. Spectral deconvolution of the unresolved binary UCDs. The spectrum of the UCD is plotted (black), along with the best-fitting single standard spectrum (green), the best-fitting binary template spectrum (red), and the two components of the binary spectrum (blue and yellow). Plotted spectra are normalised at $1.27 \mu\text{m}$. Spectra used to create the binary templates are listed in Table 7.

When compared to the parallactic distance (33.3 ± 0.3 pc), the spectrophotometric distance (45.1 ± 1.0 pc) suggests that J1126–2706 is brighter than expected. This suggests that J1126–2706 is likely to be an unresolved binary with M8 and L1-type components. [Reylé \(2018\)](#) lists J1126–2706 as a UCD.

10.4.7 J1215+0042 (M8 + L3)

J1215+0042 lies in the top right corners of the CMDs (i.e. it is brighter than would be expected considering its redness). It also lies above the cooling tracks in Fig. 8, and has a considerable difference between its spectroscopic and photometric spectral type classifications. This difference is reflected in the parallactic and spectrophotometric distance discrepancy (the parallactic distance is 44.3 ± 2.1 pc and the spectrophotometric distance is 73.0 ± 3.1 pc).

Performing a chi-squared fit of template binary spectra gives a best-fitting binary with M8 and L3-type components. A by-eye comparison of the binary template spectrum with that of the M8 standard and the UCD, reveals that the binary spectrum is the better match. The η_{SB} value of 1.022 shows that there is not a > 90 per cent confidence that the binary fit is better than the single-spectrum fit, although all other indicators suggest that J1215+0042 is a binary. It is thus more likely that J1215+0042 is an unresolved binary with M8 and L3-type components. J1215+0042 has been previously published as a UCD with a photometric spectral type of L1.5 by [Skrzypek et al. \(2015\)](#).

10.4.8 J1320+4238 (M7)

J1320+4238 is a weak unresolved binary candidate based on its spectral indices, with a best-fitting binary template of a M6 + M7 system. This binary template is not a closer match to our observed spectrum than that of a single M7-type UCD when compared by-eye. This is further supported by the η_{SB} value of 1.025, indicating a < 90 per cent confidence on the binary spectral fit being better than the single-source fit.

The single-source nature of J1320+4238 is further supported by the agreement between then parallactic and spectrophotometric distances (26.7 ± 0.0 pc and 29.4 ± 1.0 pc, respectively). We can thus conclude that J1320+4238 is most likely to be a single M7-type UCD.

10.4.9 J1423+5146 (M7)

J1423+5146 is not identified as an unresolved binary candidate based on its spectral indices, but it has a RUWE value of 1.2084, and we have not found any potential wide companions for J1423+5146, so it is possible that it is an unresolved binary. A chi-squared fit of binary template spectra results in a best-fitting binary comprised of M6 + M7 components, which is almost identical to the single-source spectral template. The η_{SB} value of 0.974 shows that there is a < 90 per cent confidence that the binary template is a better-fit to the spectrum of J1423+5146, thus this is most likely a single M7-type UCD. This is further supported by the consistency between the parallactic distance (17.3 ± 0.0 pc) and spectrophotometric distance (18.6 ± 0.4 pc). J1423+5146 is therefore unlikely to be an unresolved binary.

10.4.10 J1536+0646 (L0)

J1536+0646 has a RUWE value of 1.2198, suggesting that this could be a binary object. J1536+0646 has been published as a UCD by [Zhang et al. \(2010\)](#), and has a photometric spectral type of L2 by [Skrzypek et al. \(2015\)](#). The small discrepancy between their photometric spectral type and our spectroscopic classification of L0 further suggests that it may be a binary. This is furthered by the 2-subtype difference between the optical and NIR spectroscopic classifications.

A chi-squared fit of binary template spectra reveals a L1 + T4 to be the best-fitting binary spectrum; however, the single-source spectrum of the L0 standard better represents the spectrum of J1536+0646 when making a comparison by-eye. There is a < 90 per cent confidence in the binary fit being better than the single-source fit, as shown by the η_{SB} value of 0.550. The possibility of the UCD being a single-object source is further supported by the consistency between the parallactic distance (60.8 ± 4.2 pc) and spectrophotometric distance (65.8 ± 2.6 pc); thus it is mostly likely that this is a single UCD.

J1536+0646 is also identified as a potential thick disc object in Section 9.2, with a radial velocity of 74.8 ± 14.1 km s⁻¹ and space velocities of $U = -65.2$ km s⁻¹, $V = -36.3$ km s⁻¹, $W = -18.6$ km s⁻¹. This places the UCD in the thick disc region of the Toomre diagram, although the spectrum is not indicative of a subdwarf; thus it is likely that J1536+0646 is a single UCD located in the thick disc.

10.4.11 J1544+3301 (L2)

J1544+3301 is a strong unresolved binary candidate, based on the spectral index criteria laid out in Section 9.4. A chi-squared fit of the binary template spectra reveals an L0 + L2 binary to be the best-fitting binary template, and plotting a comparison between this binary spectrum and that of the L2 standard 2MASSW J2130446–084520 shows that the single source is a better match to the spectrum of J1544+3301 when compared by-eye. The η_{SB} value of 0.744 reflects this, showing that there is a < 90 per cent confidence that the binary template is a better fit.

This suggestion of J1544+3301 being a single source is inconsistent with the discrepancy between the parallactic (23.9 ± 0.4 pc) and spectrophotometric distances (44.5 ± 5.8 pc), since the spectrophotometric distance suggests that J1554+3301 is brighter than a typical L2-type UCD. This could be explained by J1544+3301 being a young UCD, since the BANYAN Σ tool identifies J1544+3301 as being a potential member of the Rhea 300 moving group, a young moving group at an average distance of around 24 pc. This distance is very similar to J1544+3301's parallactic distance of ~ 23.9 pc, so it is possible that the UCD is a member of the young moving group, although distance alone is insufficient for determining a UCD's membership to a young moving group. Further investigation will be required to confirm the youth of J1544+3301.

10.4.12 J1628–4652 (M9 + L9)

J1628–4652 is a strong unresolved binary candidate, based on its spectral indices (Section 9.4). The best-fitting binary template is a M9 + L9 system, which matches our observed spectrum better than that of a single M8-type UCD when compared by-eye. The η_{SB} value of 1.133 indicates a > 90 per cent confidence that the binary template is a better fit to the UCD's spectrum than the single-source model.

This binarity is further supported by the difference between the parallactic (62.2 ± 3.8 pc) and spectrophotometric distances (81.7 ± 2.5 pc). It is therefore likely that J1628–4652 is an unresolved M9 + L9 binary.

10.4.13 J1938+4321 (M6)

J1938+4321 is a weak unresolved binary candidate, satisfying two of the spectral index selection criteria outlined in Section 9.4. A χ^2 fitting of binary templates reveals a M7 + M9 to be the best-fitting binary template. A by-eye comparison of the binary and single-source spectral fits reveals that the single M6-type spectrum is more similar to the spectrum of J1938+4321. This is supported by the η_{SB} value of 0.839, since there is a < 90 per cent confidence that the binary template is a better fit than the single-source spectrum. The spectrophotometric distance of 29.5 ± 0.4 pc is consistent with the parallactic distance of 26.8 ± 0.3 pc, thus it is likely that J1938+4321 is not an unresolved binary.

11 CONCLUSIONS

In this paper, 51 *Gaia* UCDs have been observed with the Blanco ARCoIRIS and IRTF SpeX instruments, in order to classify the spectral types of each UCD. 44 of these are new classifications, while three already have published NIR spectroscopic types. These previously published spectral classifications are consistent with our NIR spectral types. All but one of the UCDs are within 100 pc: 37 lie within 50 pc, and the more distant UCD lies at ~ 227 pc.

The PYTHON module SPLAT was used to classify the spectra, identifying the spectral types of the UCDs by comparing them with standards from the SpeX Prism Library. Our sample is comprised of a total of 26 M-types, 24 L-types and one T-type UCD, and the spectral type consistency has been confirmed using the photometric classification method outlined by Skrzypek et al. (2015).

The photometry for the UCDs follow the general trends that would be expected, based on Smart et al. (2019), and plotting the UCDs on CMDs and cooling track plots reveals that the majority of our UCDs are old and stellar in nature. There are, however, a few UCDs of interest that lie away from the general trends, highlighting potential young, binary and thick disc/subdwarf UCDs.

In addition, our spectra allow for more detailed analysis of the UCDs, namely their effective temperatures and radial velocities can be estimated. By comparing our UCDs' spectra with the BT-Settl CIFIST spectra, we can find the best-fitting temperature for each UCD, and doing so gives a temperature range between 1200 K and 3000 K for the UCDs in our sample. Using the rvfitter module for PYTHON, we were able to measure the radial velocities for the higher resolution observations (i.e. the ARCoIRIS and SpeX SXD observations).

By combining published data with measurements of radial velocities using our spectra, we find a number of UCDs which have properties similar to young UCDs, as well as some thick disc and subdwarf UCDs and a plethora of wide and unresolved binary UCDs. Looking at these UCDs individually, we find a total of seven young, three thick disc, one subdwarf, six wide binary and six unresolved binary UCDs, though further observations and deeper investigation will be required to confirm the full properties of these UCDs.

Table 12: Indications of youth, thick disc, halo and binary UCDS given by sensitive features for each UCD in this work, including BANYAN Σ group membership, SPLAT surface gravity classification, spectral features and Gaia DR3 data.

Object Short Name	SpT	CMD Position	Cooling Track	BANYAN Σ Membership	BANYAN Σ Probability	Surface Gravity	Spectral Shape	FeH/TiO Features	Toomre Diagram	Gaia DR3 RUWE	Gaia DR3 v_{tan} (km s ⁻¹)	Young, Thick Disc, or Binary?
J0508+3319	L2	-	-	Field	1.000	FLD-G	-	-	-	1.0803	58.428 ± 0.512	-
J0515+0613	M9	-	-	Field	0.970	FLD-G	-	-	Thick disc	1.0773	17.956 ± 0.969	Thick disc
J0526-5026	L6	-	-	Field	0.988	FLD-G	-	-	-	1.1563	28.615 ± 0.686	-
J0542+0041	L7	-	-	Field	0.993	VL-G	Young	Young	-	1.1348	6.276 ± 0.208	-
J0723+4622	L1	-	-	Field	1.000	FLD-G	-	-	-	1.2470	43.728 ± 3.890	UB
J0808+3157	M7	-	-	Field	1.000	FLD-G	-	-	-	1.0626	17.167 ± 0.041	-
J0811+1855	L1	-	-	Field	0.830	FLD-G	-	Young	-	1.1226	12.953 ± 0.173	-
J0817-6155	T6	VLM	VLM	Field	1.000	INT-G	-	-	-	1.2429	27.437 ± 0.062	Young
J0832+3538	M6	-	-	Field	1.000	FLD-G	-	-	-	1.0809	52.493 ± 0.155	-
J0850-0318	M8	-	-	Field	1.000	FLD-G	-	-	-	1.0475	30.226 ± 0.282	WB
J0900+5205	M9	-	-	Field	1.000	INT-G	-	-	-	1.0702	47.448 ± 4.877	-
J0911+1432	M9	-	-	Field	1.000	FLD-G	-	-	-	1.1326	23.698 ± 1.276	UB
J0916-1121	M8	-	-	Field	1.000	FLD-G	-	-	-	1.1117	64.271 ± 0.489	-
J0941+3315A	M8	-	Young	Field	1.000	FLD-G	-	-	-	0.9854	71.002 ± 0.383	WB
J0942-2551	L1	-	-	CARN	0.939	FLD-G	-	-	-	1.2074	24.561 ± 1.482	Young
J0948+5300	L1	-	-	Field	1.000	VL-G	-	-	-	1.1384	23.938 ± 0.933	-
J1036-3441	L8	VLM	VLM	Field	1.000	INT-G	-	-	-	1.2900	31.890 ± 0.759	UB
J1048-5254	L1	-	-	CARN	0.753	FLD-G	-	-	-	1.0817	31.793 ± 0.163	-
J1126-2706	M8	-	-	Field	1.000	FLD-G	-	Young	-	1.3152	19.522 ± 0.184	UB
J1143+5324	L1	-	-	Field	1.000	FLD-G	Young	Young	-	1.1220	6.603 ± 0.381	-
J1150-2914	L0	-	-	CARN	0.538	FLD-G	-	-	-	1.0407	35.029 ± 0.686	-
J1152+5901	L0	-	-	Cri198	0.983	INT-G	-	-	-	1.0817	36.561 ± 1.517	Young
J1158-0008	M9	Old	Old	Field	1.000	FLD-G	-	-	-	0.9978	50.337 ± 5.224	-
J1158+3817	M7	-	-	Field	1.000	FLD-G	Young	-	-	1.0730	76.462 ± 0.849	-
J1212+0206	L1	-	-	Field	1.000	FLD-G	-	-	-	1.1962	33.893 ± 3.321	-
J1215+0042	M9	Binary	Binary	Field	0.999	FLD-G	-	-	-	1.1442	21.441 ± 1.123	UB
J1243+6001	L7	-	-	Cri227	0.439	VL-G	Young	-	-	-	-	Young, WB
J1250+0455	M9	-	-	Field	1.000	FLD-G	-	-	-	1.5097	46.326 ± 3.845	WB
J1252+0347	M8	-	-	Field	1.000	FLD-G	-	-	-	1.1078	85.143 ± 8.211	-
J1307+0246	L1	-	-	Field	1.000	FLD-G	-	-	-	1.0784	65.477 ± 1.569	-
J1313+1404	M7	-	-	Field	0.997	FLD-G	-	-	-	1.1653	41.188 ± 2.220	-
J1315+3232	M7	-	-	Field	1.000	INT-G	-	-	-	0.9841	11.702 ± 0.038	Young
J1320+4238	M7	-	-	Field	1.000	FLD-G	-	-	-	0.9897	25.281 ± 0.044	-
J1420+3235	M7	-	-	Field	1.000	FLD-G	-	-	-	1.1934	13.828 ± 0.096	WB
J1423+5346	M7	-	-	Field	1.000	FLD-G	-	-	-	1.2084	33.692 ± 0.035	-
J1441+4217	L3	-	-	Cri198	0.957	FLD-G	-	-	-	1.1242	34.567 ± 1.002	Young
J1452+0931	M8	-	-	Field	1.000	FLD-G	Young	-	-	1.1047	52.494 ± 1.733	-
J1514+3547	L1	-	-	Field	1.000	FLD-G	-	-	-	0.9870	30.576 ± 1.731	-
J1536+0646	L0	-	-	Field	1.000	FLD-G	-	-	-	1.2198	24.587 ± 1.895	Thick disc
J1544-0435	L1	-	-	UMC	0.988	INT-G	Young	Young	-	1.0325	12.626 ± 1.114	Young
J1544+3301	L2	Old	Old	OCTN	0.996	FLD-G	-	-	-	1.0985	8.965 ± 0.212	-

Table 12: – continued

Object Short Name	SpT	CMD Position	Cooling Track	BANYAN Σ Membership	BANYAN Σ Probability	Surface Gravity	Spectral Shape	FeH/TiO Features	Toomre Diagram	<i>Gaia</i> DR3 RUWE	<i>Gaia</i> DR3 v_{tan} (km s ⁻¹)	Young, Thick Disc, or Binary?
J1628–4652	M8	–	–	Field	1.000	FLD-G	–	–	–	1.2326	37.572 ± 2.468	UB
J1637+1813	M7	–	–	UMC	0.993	FLD-G	–	–	–	1.0922	16.132 ± 0.589	–
J1646–2115	sdL2	–	–	Field	1.000	INT-G	Subdwarf	Subdwarf	Thick disc	1.1187	72.582 ± 6.387	Subdwarf
J1654–3819	M6	–	–	Field	1.000	FLD-G	–	–	–	1.0395	54.161 ± 0.082	–
J1700–4048	L4	–	Young	Field	0.989	VL-G	–	–	Thick disc	1.0781	112.745 ± 33.819	Thick disc
J1713–3952	L1	–	–	Field	1.000	FLD-G	Flat	–	–	1.0167	28.122 ± 0.101	–
J1737+4705	M8	–	–	Field	1.000	FLD-G	–	–	–	1.0364	86.863 ± 0.676	–
J1847–3419	M7	–	–	Field	0.998	FLD-G	–	–	–	1.1031	5.651 ± 0.022	–
J1938+4321	M6	–	–	Field	1.000	FLD-G	–	–	–	1.1077	34.835 ± 0.046	–
J2019+2256	L2	–	–	CARN	0.855	FLD-G	–	Young	–	1.0464	19.938 ± 0.207	WB

Notes. The young association full names are: Cassiopeia-Taurus (Cas-Tau), Octans-Near (OCTN), Carina-Near (CARN), Rhea 449 (Rhea449), Crisus 198 (Cris198), Ursa Major Corona (UMC) and Rhea 300 (Rhea300).

WB = wide binary; UB = unresolved binary.

ACKNOWLEDGEMENTS

GC is funded by a University of Hertfordshire studentship. RLS has been supported by a STSM grant from COST Action CA18104: MW-Gaia. GC, HRAJ, WJC, DJP recognise the computing infrastructure provided via STFC grant ST/R000905/1 at the University of Hertfordshire.

Based in part on observations made at the Infrared Telescope Facility, which is operated by the University of Hawaii under contract 80HQTR19D0030 with the National Aeronautics and Space Administration, and observations made at Cerro Tololo Inter-American Observatory at NSF's NOIRLab (NOIRLab Prop. ID 2018A-0910; PI: J. Beamin), which is managed by the Association of Universities for Research in Astronomy (AURA) under a cooperative agreement with the National Science Foundation. This paper makes use of observations made at Infrared Telescope Facility, which is operated by the University of Hawaii under contract 80HQTR19D0030 with the National Aeronautics and Space Administration.

This paper makes use of data from the SIMBAD database, operated at CDS, Strasbourg, France (<http://simbad.u-strasbg.fr/Simbad>).

This work has made use of data from the European Space Agency (ESA) mission *Gaia* (<https://www.cosmos.esa.int/gaia>), processed by the *Gaia* Data Processing and Analysis Consortium (DPAC, <https://www.cosmos.esa.int/web/gaia/dpac/consortium>). Funding for the DPAC has been provided by national institutions, in particular the institutions participating in the *Gaia* Multilateral Agreement.

This research has benefited from the SpeX Prism spectral Libraries, maintained by Adam Burgasser at <https://cass.ucsd.edu/~ajb/browndwarfs/spexprism/index.html>. SPLAT is an collaborative project of research students in the UCSD Cool Star Lab, aimed at developing research through the building of spectral analysis tools. Contributors to SPLAT have included Christian Aganze, Jessica Birky, Daniella Bardalez Gagliuffi, Adam Burgasser (PI), Caleb Choban, Andrew Davis, Ivanna Escala, Joshua Hazlett, Carolina Herrera Hernandez, Elizabeth Moreno Hilario, Aishwarya Iyer, Yuhui Jin, Mike Lopez, Dorsa Majidi, Diego Octavio Talavera Maya, Alex Mendez, Gretel Mercado, Niana Mohammed, Johnny Parra, Maitrayee Sahi, Adrian Suarez, Melissa Tallis, Tomoki Tamiya, Chris Theissen, and Russell van Linge. This project has been supported by the National Aeronautics and Space Administration under Grant No. NNX15AI75G.

The Pan-STARRS1 Surveys (PS1) and the PS1 public science archive have been made possible through contributions by the Institute for Astronomy, the University of Hawaii, the Pan-STARRS Project Office, the Max-Planck Society and its participating institutes, the Max Planck Institute for Astronomy, Heidelberg and the Max Planck Institute for Extraterrestrial Physics, Garching, The Johns Hopkins University, Durham University, the University of Edinburgh, the Queen's University Belfast, the Harvard-Smithsonian Center for Astrophysics, the Las Cumbres Observatory Global Telescope Network Incorporated, the National Central University of Taiwan, the Space Telescope Science Institute, the National Aeronautics and Space Administration under Grant No. NNX08AR22G issued through the Planetary Science Division of the NASA Science Mission Directorate, the National Science Foundation Grant No. AST-1238877, the University of Maryland, Eotvos Lorand University (ELTE), the Los Alamos National Laboratory, and the Gordon and Betty Moore Foundation.

This publication makes use of data products from the Two

Micron All Sky Survey, which is a joint project of the University of Massachusetts and the Infrared Processing and Analysis Center/California Institute of Technology, funded by the National Aeronautics and Space Administration and the National Science Foundation.

This publication makes use of data products from the Wide-field Infrared Survey Explorer, which is a joint project of the University of California, Los Angeles, and the Jet Propulsion Laboratory/California Institute of Technology, and NEOWISE, which is a project of the Jet Propulsion Laboratory/California Institute of Technology. WISE and NEOWISE are funded by the National Aeronautics and Space Administration.

We acknowledge the relevant open source packages used in our PYTHON codes (van Rossum & de Boer 1991): Astropy (Astropy Collaboration et al. 2013, 2018, 2022), Matplotlib (Hunter 2007), NumPy (Harris et al. 2020), pandas (McKinney 2010), rvfitter (Cooper 2022), SciPy (Virtanen et al. 2020), specutils (Astropy-Specutils Development Team 2019), SPLAT (Burgasser & Splat Development Team 2017).

DATA AVAILABILITY

The data underlying this article will be available in CDS VizieR, the GUCDS Data Browser, and the SIMPLE Database.

REFERENCES

- Abel M., Frommhold L., Li X., Hunt K. L. C., 2012, in 67th International Symposium on Molecular Spectroscopy. p. RC04
- Allard F., Homeier D., Freytag B., 2012, *Philosophical Transactions of the Royal Society of London Series A*, 370, 2765
- Allers K. N., Liu M. C., 2013, *ApJ*, 772, 79
- Almendros-Abad V., Mužić K., Moitinho A., Krone-Martins A., Kubiak K., 2022, *A&A*, 657, A129
- Alonso-Floriano F. J., et al., 2015, *A&A*, 577, A128
- Artigau É., Radigan J., Folkes S., Jayawardhana R., Kurtev R., Lafrenière D., Doyon R., Borissova J., 2010, *ApJ*, 718, L38
- Astropy Collaboration et al., 2013, *A&A*, 558, A33
- Astropy Collaboration et al., 2018, *AJ*, 156, 123
- Astropy Collaboration et al., 2022, *apj*, 935, 167
- Astropy-Specutils Development Team 2019, Specutils: Spectroscopic analysis and reduction, Astrophysics Source Code Library (ascl:1902.012), <https://ui.adsabs.harvard.edu/abs/2019ascl.soft02012A>
- Baig S., Smart R. L., Jones H. R. A., Gagné J., Pinfield D. J., Cheng G., Moranta L., 2024, *MNRAS*, 533, 3784
- Bailer-Jones C. A. L., et al., 2013, *A&A*, 559, A74
- Baraffe I., Homeier D., Allard F., Chabrier G., 2015, *A&A*, 577, A42
- Bardalez Gagliuffi D. C., et al., 2014, *ApJ*, 794, 143
- Basri G., Mohanty S., Allard F., Hauschildt P. H., Delfosse X., Martín E. L., Forveille T., Goldman B., 2000, *ApJ*, 538, 363
- Bates D. R., 1952, *MNRAS*, 112, 40
- Bédard A., Bergeron P., Brassard P., Fontaine G., 2020, *ApJ*, 901, 93
- Beiler S. A., Allers K. N., Cushing M., Faherty J., Marley M., Skemer A., 2023, *MNRAS*, 518, 4870
- Belokurov V., et al., 2020, *MNRAS*, 496, 1922
- Blaauw A., 1956, *ApJ*, 123, 408
- Borysow A., 2002, *A&A*, 390, 779
- Borysow A., Frommhold L., Moraldi M., 1989, *ApJ*, 336, 495
- Bouy H., et al., 2022, *arXiv e-prints*
- Bowler B. P., et al., 2019, *ApJ*, 877, 60
- Brown A. G. A., et al., 2018, *A&A*, 616, A1
- Burgasser A. J., 2014, in Astronomical Society of India Conference Series. pp 7–16, doi:10.48550/arXiv.1406.4887

- Burgasser A. J., Splat Development Team 2017, in *Astronomical Society of India Conference Series*. pp 7–12, doi:10.48550/arXiv.1707.00062
- Burgasser A. J., et al., 2002, *ApJ*, 564, 421
- Burgasser A. J., Kirkpatrick J. D., Lépine S., 2005, in Favata F., Hussain G. A. J., Battrick B., eds, *ESA Special Publication Vol. 560, 13th Cambridge Workshop on Cool Stars, Stellar Systems and the Sun*. p. 237
- Burgasser A. J., Geballe T. R., Leggett S. K., Kirkpatrick J. D., Golimowski D. A., 2006, *ApJ*, 637, 1067
- Burgasser A. J., Lépine S., Lodieu N., Scholz R.-D., Delorme P., Jao W.-C., Swift B. J., Cushing M. C., 2009, in Stempels E., ed., *American Institute of Physics Conference Series Vol. 1094, 15th Cambridge Workshop on Cool Stars, Stellar Systems, and the Sun*. pp 242–249, doi:10.1063/1.3099098
- Burgasser A. J., Cruz K. L., Cushing M., Gelino C. R., Looper D. L., Faherty J. K., Kirkpatrick J. D., Reid I. N., 2010, *ApJ*, 710, 1142
- Calamari E., Faherty J. K., Visscher C., Gemma M. E., Burningham B., Rothermich A., 2024, *ApJ*, 963, 67
- Cannon A. J., Pickering E. C., 1993, *VizieR Online Data Catalog*, p. III/135A
- Chambers K. C., et al., 2016, *arXiv e-prints*, p. arXiv:1612.05560
- Choi J., Dotter A., Conroy C., Cantiello M., Paxton B., Johnson B. D., 2016, *ApJ*, 823, 102
- Chupina N. V., Reva V. G., Vereshchagin S. V., 2006, *A&A*, 451, 909
- Cifuentes C., Caballero J. A., Agustí S., 2021, *Research Notes of the American Astronomical Society*, 5, 129
- Cooper W. J., 2022, *Zenodo*
- Cooper W., Nicastro L., 2023, *GUCCDS Data Browser*, <https://guccds.inaf.it/>
- Cooper W. J., et al., 2024, *MNRAS*, 534, 695
- Cruz K. L., et al., 2007, *AJ*, 133, 439
- Cruz K., Rodriguez D. R., Whiteford N. P., Fontanive C., Hort E. B., Terach D. P., Cooper W., 2023, *SIMPLE Database*, <https://simple-bd-archive.org/>
- Cummings J. D., Kalirai J. S., Tremblay P. E., Ramirez-Ruiz E., Choi J., 2018, *ApJ*, 866, 21
- Cushing M. C., Vacca W. D., Rayner J. T., 2004, *PASP*, 116, 362
- Cushing M. C., et al., 2011, *ApJ*, 743, 50
- Cushing M., Vacca W., Rayner J., 2017, *SpeX FITS Keyword Reference*, http://irtfweb.ifa.hawaii.edu/~s2/software/Spex_FITS_keyword_reference/Spex_FITS_keyword_reference-v1.2.pdf
- Dahn C. C., et al., 2002, *AJ*, 124, 1170
- Day-Jones A. C., et al., 2013, *MNRAS*, 430, 1171
- Deacon N. R., Hambly N. C., King R. R., McCaughrean M. J., 2009, *MNRAS*, 394, 857
- Deacon N. R., et al., 2014, *ApJ*, 792, 119
- Dopcke G., Porto de Mello G. F., Sneden C., 2019, *MNRAS*, 485, 4375
- Dotter A., 2016, *ApJS*, 222, 8
- Dupuy T. J., Liu M. C., 2012, *ApJS*, 201, 19
- Eggen O. J., 1998, *ApJ*, 115, 2397
- Eisenhardt P. R. M., et al., 2020, *ApJS*, 247, 69
- Fabircius C., et al., 2021, *A&A*, 649, A5
- Faherty J. K., Burgasser A. J., Cruz K. L., Shara M. M., Walter F. M., Gelino C. R., 2009, *AJ*, 137, 1
- Faherty J. K., et al., 2021, *ApJ*, 923, 48
- Filippazzo J. C., Rice E. L., Faherty J., Cruz K. L., Van Gordon M. M., Looper D. L., 2015, *ApJ*, 810, 158
- Folkes S. L., et al., 2012, *MNRAS*, 427, 3280
- Gagné J., Best W., 2014b, *List of All UltraCool Dwarfs*, <https://docs.google.com/spreadsheets/d/1shqSyDMEForWLRvTqYEHTt8T-TDqWCTX00zWivP97oU/edit?usp=sharing>
- Gagné J., Best W., 2014a, *List of M6-M9 Dwarfs*, https://docs.google.com/spreadsheets/d/1Vq1RzHL2y_racQgd6vrWUj5s8S1Ruv_Y6nvzTJwjTXs/edit?usp=sharing
- Gagné J., et al., 2018, *ApJ*, 856, 23
- Gaia Collaboration et al., 2016, *A&A*, 595, A1
- Gaia Collaboration et al., 2018, *A&A*, 616, A10
- Gaia Collaboration et al., 2021a, *A&A*, 649, A6
- Gaia Collaboration et al., 2021b, *A&A*, 650, C3
- Gaia Collaboration et al., 2022, *A&A*
- Gaidos E., et al., 2014, *MNRAS*, 443, 2561
- Gálvez-Ortiz M. C., Solano E., Lodieu N., Aberasturi M., 2017, *MNRAS*, 466, 2983
- Geballe T. R., et al., 2002, *ApJ*, 564, 466
- Geißler K., Metchev S., Kirkpatrick J. D., Berriman G. B., Looper D., 2011, *ApJ*, 732, 56
- Gentile Fusillo N. P., et al., 2019, *MNRAS*, 482, 4570
- Gentile Fusillo N. P., et al., 2021, *MNRAS*, 508, 3877
- Gerasimov R., Homeier D., Burgasser A., Bedin L. R., 2020, *Research Notes of the American Astronomical Society*, 4, 214
- Gershberg R. E., Katsova M. M., Lovkaya M. N., Terebizh A. V., Shakhovskaya N. I., 1999, *A&AS*, 139, 555
- Girven J., Gänsicke B. T., Steeghs D., Koester D., 2011, *MNRAS*, 417, 1210
- Gizis J. E., 2002, *ApJ*, 575, 484
- Greco J. J., Schneider A. C., Cushing M. C., Kirkpatrick J. D., Burgasser A. J., 2019, *AJ*, 158, 182
- Guo Y. X., et al., 2019, *MNRAS*, 485, 2167
- Harris C. R., et al., 2020, *Nature*, 585, 357
- Høg E., et al., 2000, *A&A*, 355, L27
- Holmberg J., Nordström B., Andersen J., 2009, *A&A*, 501, 941
- Hunter J. D., 2007, *Computing in Science & Engineering*, 9, 90
- James D., Herter T., Schlawin E., 2015, *NOAO Newsletter*, 112, 13
- Jiménez-Esteban F. M., Torres S., Rebassa-Mansergas A., Skorobogatov G., Solano E., Cantero C., Rodrigo C., 2018, *MNRAS*, 480, 4505
- Jones J., et al., 2015, in *American Astronomical Society Meeting Abstracts #225*. p. 112.03, <https://ui.adsabs.harvard.edu/abs/2015AAS...22511203J>
- Jönsson H., et al., 2020, *AJ*, 160, 120
- Keenan P. C., McNeil R. C., 1989, *ApJS*, 71, 245
- Keenan P. C., Pitts R. E., 1980, *ApJS*, 42, 541
- Keenan P. C., Garrison R. F., Deutsch A. J., 1974, *ApJS*, 28, 271
- Kellogg K., Metchev S., Miles-Páez P. A., Tannock M. E., 2017, *AJ*, 154, 112
- Kervella P., Arenou F., Mignard F., Thévenin F., 2019, *A&A*, 623, A72
- Kimani R., Schmidt S. J., Angus R., Cruz K. L., Faherty J. K., Rice E., 2019, *AJ*, 157, 231
- Kimani R., Xu S., Faherty J. K., Gagné J., Angus R., Brandt T. D., Casewell S. L., Cruz K. L., 2022, *AJ*, 164, 62
- Kirkpatrick J. D., 1998, in *Rebolo R., Martin E. L., Zapatero Osorio M. R., eds, Astronomical Society of the Pacific Conference Series Vol. 134, Brown Dwarfs and Extrasolar Planets*. p. 405
- Kirkpatrick J. D., 2005, *ARA&A*, 43, 195
- Kirkpatrick J. D., Henry T. J., McCarthy Donald W. J., 1991, *ApJS*, 77, 417
- Kirkpatrick J. D., Henry T. J., Irwin M. J., 1997, *AJ*, 113, 1421
- Kirkpatrick J. D., et al., 2010, *ApJS*, 190, 100
- Kirkpatrick J. D., et al., 2011, *ApJS*, 197, 19
- Kirkpatrick J. D., et al., 2014, *ApJ*, 783, 122
- Kirkpatrick J. D., et al., 2016, *ApJS*, 224, 36
- Kirkpatrick J. D., et al., 2021, *ApJS*, 253, 7
- Kirkpatrick J. D., et al., 2024, *ApJS*, 271, 55
- Kramida A., Ralchenko Y., Reader J., NIST ASD Team 2023, *National Institute of Standards and Technology*, version 5.11
- Lamman C., et al., 2020, *AJ*, 159, 139
- Lépine S., Gaidos E., 2011, *AJ*, 142, 138
- Lépine S., Shara M. M., 2005, *AJ*, 129, 1483
- Lindgren L., 2018, *Re-normalising the astrometric chi-square in Gaia DR2*, *GAIA-C3-TN-LU-LL-124*, http://www.rssd.esa.int/doc_fetch.php?id=3757412
- Lindgren L., et al., 2018, *A&A*, 616, A2
- Lodieu N., Zapatero Osorio M. R., Martín E. L., Rebolo López R., Gauza B., 2022, *A&A*, 663, A84
- Luhman K. L., 2014, *ApJ*, 781, 4
- Mainzer A., et al., 2011, *ApJ*, 731, 53
- Manjavacas E., Lodieu N., Béjar V. J. S., Zapatero-Osorio M. R., Boudreault S., Bonnefoy M., 2019, *MNRAS*, 491, 5925
- Marocco F., 2014, *PhD thesis*, University of Hertfordshire, Hatfield, UK
- Marocco F., et al., 2013, *AJ*, 146, 161
- Marocco F., et al., 2015, *MNRAS*, 449, 3651

- Marocco F., et al., 2020, *MNRAS*, 494, 4891
- Marocco F., et al., 2021, *ApJS*, 253, 8
- Martin E. C., et al., 2017, *ApJ*, 838, 73
- Mason B. D., Wycoff G. L., Hartkopf W. I., Douglass G. G., Worley C. E., 2001, *AJ*, 122, 3466
- McGovern M. R., Kirkpatrick J. D., McLean I. S., Burgasser A. J., Prato L., Lowrance P. J., 2004, *ApJ*, 600, 1020
- McKinney W., 2010, in van der Walt S., Millman J., eds, Proceedings of the 9th Python in Science Conference. pp 56 – 61, doi:10.25080/Majora-92bf1922-00a
- McLean I. S., Prato L., Kim S. S., Wilcox M. K., Kirkpatrick J. D., Burgasser A., 2001, *ApJ*, 561, L115
- Medan I., Lépine S., Hartman Z., 2021, *AJ*, 161, 234
- Moranta L., Gagné J., Couture D., Faherty J. K., 2022, *ApJ*, 939, 94
- Morrell S., Naylor T., 2019, *MNRAS*, 489, 2615
- Newton E. R., Charbonneau D., Irwin J., Berta-Thompson Z. K., Rojas-Ayala B., Covey K., Lloyd J. P., 2014, *AJ*, 147, 20
- Nissen P. E., 2004, in McWilliam A., Rauch M., eds, Origin and Evolution of the Elements. p. 154, doi:10.48550/arXiv.astro-ph/0310326
- Paschen F., 1908, doi:10.1002/andp.19083321303
- Patience J., King R. R., De Rosa R. J., Vigan A., Witte S., Rice E., Helling C., Hauschildt P., 2012, *A&A*, 540, A85
- Penoyre Z., Belokurov V., Evans N. W., 2022, *MNRAS*, 513, 2437
- Phan-Bao N., et al., 2008, *MNRAS*, 383, 831
- Pye J. P., Rosen S., Fyfe D., Schröder A. C., 2015, *A&A*, 581, A28
- Ravinet T., et al., 2024, *arXiv e-prints*, p. arXiv:2402.09783
- Rayner J. T., Toomey D. W., Onaka P. M., Denault A. J., Stahlberger W. E., Vacca W. D., Cushing M. C., Wang S., 2003, *PASP*, 115, 362
- Reid I. N., Gizis J. E., 2005, *PASP*, 117, 676
- Reid I. N., Hawley S. L., Gizis J. E., 1995, *AJ*, 110, 1838
- Reid I. N., et al., 2004, *AJ*, 128, 463
- Reid I. N., Cruz K. L., Kirkpatrick J. D., Allen P. R., Mungall F., Liebert J., Lowrance P., Sweet A., 2008, *AJ*, 136, 1290
- Reylé C., 2018, *A&A*, 619, L8
- Riello M., et al., 2021, *A&A*, 649, A3
- Sarro L. M., et al., 2023, *A&A*, 669, A139
- Saumon D., Marley M. S., Abel M., Frommhold L., Freedman R. S., 2012, *ApJ*, 750, 74
- Schlawin E., et al., 2014, in Ramsay S. K., McLean I. S., Takami H., eds, Society of Photo-Optical Instrumentation Engineers (SPIE) Conference Series Vol. 9147, Ground-based and Airborne Instrumentation for Astronomy V. p. 91472H, doi:10.1117/12.2055233
- Schmidt S. J., West A. A., Bochanski J. J., Hawley S. L., Kielty C., 2014, *PASP*, 126, 642
- Schmidt S. J., Hawley S. L., West A. A., Bochanski J. J., Davenport J. R. A., Ge J., Schneider D. P., 2015, *AJ*, 149, 158
- Schneider A. C., Greco J., Cushing M. C., Kirkpatrick J. D., Mainzer A., Gelino C. R., Fajardo-Acosta S. B., Bauer J., 2016, *ApJ*, 817, 112
- Scholz R. D., 2020, *A&A*, 637, A45
- Sebastian D., et al., 2021, *A&A*, 645, A100
- Seli B., Vida K., Moór A., Pál A., Oláh K., 2021, *A&A*, 650, A138
- Sharples R. M., Whitelock P. A., Feast M. W., 1995, *MNRAS*, 272, 139
- Skiff B. A., 2008, Unpublished
- Skrutskie M. F., et al., 2006, *AJ*, 131, 1163
- Skrzypczek N., Warren S. J., Faherty J. K., Mortlock D. J., Burgasser A. J., Hewett P. C., 2015, *A&A*, 574, A78
- Skrzypczek N., Warren S. J., Faherty J. K., 2016, *A&A*, 589, A49
- Smart R. L., Marocco F., Caballero J. A., Jones H. R. A., Barrado D., Beamín J. C., Pinfield D. J., Sarro L. M., 2017, *MNRAS*, 469, 401
- Smart R. L., Marocco F., Sarro L. M., Barrado D., Beamín J. C., Caballero J. A., Jones H. R. A., 2019, *MNRAS*, 485, 4423–4440
- Solano E., et al., 2019, *A&A*, 627, A29
- Steele I. A., Jones H. R. A., 2001, *PASP*, 113, 403
- Stephenson C. B., 1986, *AJ*, 92, 139
- Suárez G., Metchev S., 2022, *MNRAS*, 513, 5701
- Taylor M. B., 2005, in Shopbell P., Britton M., Ebert R., eds, Astronomical Society of the Pacific Conference Series Vol. 347, Astronomical Data Analysis Software and Systems XIV. p. 29
- Tofflemire B. M., et al., 2021, *AJ*, 161, 171
- Ulla A., et al., 2022, Gaia DR3 documentation Chapter 11: Astrophysical parameters, Gaia DR3 documentation, European Space Agency; Gaia Data Processing and Analysis Consortium. id. 11
- Uppgren A. R., 1962, *AJ*, 67, 37
- Vacca W. D., Cushing M. C., Rayner J. T., 2003, *PASP*, 115, 389
- Veyette M. J., Muirhead P. S., Mann A. W., Allard F., 2016, *ApJ*, 828, 95
- Virtanen P., et al., 2020, *Nature Methods*, 17, 261
- Vysotsky A. N., Balz A. G. A. J., 1958, Publications of the Leander McCormick Observatory, 13, 0
- Wang Y.-F., et al., 2022, *A&A*, 660, A38
- Warren S. J., et al., 2007, *MNRAS*, 381, 1400
- Wenger M., et al., 2000, *A&AS*, 143, 9
- West A. A., Bochanski J. J., Bowler B. P., Dotter A., Johnson J. A., Lépine S., Rojas-Ayala B., Schweitzer A., 2011, in Johns-Krull C., Browning M. K., West A. A., eds, Astronomical Society of the Pacific Conference Series Vol. 448, 16th Cambridge Workshop on Cool Stars, Stellar Systems, and the Sun. p. 531, doi:10.48550/arXiv.1101.1086
- Witte S., Helling C., Barman T., Heidrich N., Hauschildt P. H., 2011, *A&A*, 529, A44
- Wright E. L., et al., 2010, *AJ*, 140, 1868
- Zhang Z. H., et al., 2009, *A&A*, 497, 619
- Zhang Z. H., et al., 2010, *MNRAS*, 404, 1817
- Zhang Z. H., Pinfield D. J., Burningham B., Jones H. R. A., Day-Jones A. C., Marocco F., Gomes J., Galvez-Ortiz M. C., 2013a, in European Physical Journal Web of Conferences. p. 06007, doi:10.1051/epjconf/20134706007
- Zhang Z. H., et al., 2013b, Mem. Soc. Astron. Italiana, 84, 989
- Zhang Z. H., Pinfield D. J., Burningham B., Gálvez-Ortiz M. C., Jones H. R. A., Marocco F., Smart R. L., Lodieu N., 2014, Mem. Soc. Astron. Italiana, 85, 736
- Zhang Z. H., et al., 2017, *MNRAS*, 464, 3040
- Zhang S., et al., 2019, *ApJS*, 240, 31
- Zuckerman B., Bessell M. S., Song I., Kim S., 2006, *ApJ*, 649, L115
- Zuckerman B., Vican L., Song I., Schneider A., 2013, *ApJ*, 778, 5
- van Rossum G., de Boer J., 1991, *CWI Quarterly*, 4, 283

APPENDIX A: OBSERVING LOG

The observation log for this work is presented in Table A1.

APPENDIX B: NON-UCD OBJECTS

On several of the observing nights, conditions were too poor to be able to make observations of the UCD targets from the list of UCDS. In these cases, alternative objects were observed, so as to not waste observing time. The same steps were taken to analyse the spectra of these objects that as for the UCDS, albeit in not as much depth. As would be expected, all of the non-UCDs that were observed can be found in *Gaia* DR3, and most of them can be found in SIMBAD with published classifications (shown in Table B1). Additionally, some of the UCDS were determined to have spectral classifications earlier than M7 so are presented in this appendix.

B1 Data Collection and Reduction

In addition to the UCDS presented in the main body of this work, we also observed some objects which are not classified as UCDS. Some of these objects were in the GUCDS candidate list, with their new spectroscopic classifications narrowly missing the M7 classification required to be considered a UCD, while their photometric classifications from literature may suggest that they are UCDS. Others of these non-UCDS are giant stars, which were

Table A1. Observation log for the observations used for this work, showing details of gratings and exposure times for each observation made. The observation date and average airmass of each object are also noted.

Object Short Name	Observation Date (UTC)	Instrument –	Average Airmass	Exp Time DIT (s) × NDIT	Telluric Standard	Standard Exp Time DIT (s) × NDIT	Standard <i>B</i> (mag) ^a	Standard <i>V</i> (mag) ^a
J0526–5026	2018 Apr 03	ARCoIRIS	1.62	240 × 4	HD 36381	8 × 4	7.98	7.99
J0817–6155	2018 Apr 03	ARCoIRIS	1.18	45 × 4	HD 62091	5 × 4	7.67	7.61
J1036–3441	2018 Apr 03	ARCoIRIS	1.01	300 × 4	HD 92678	4 × 4	6.84	6.80
J1048–5254	2018 Apr 03	ARCoIRIS	1.16	90 × 4	HD 95534	5 × 4	6.82	6.81
J1158–0008	2018 Apr 03	ARCoIRIS	1.18	300 × 4	HD 97585	1.2 × 4	5.37	5.40
J1212+0206	2018 Apr 03	ARCoIRIS	1.18	300 × 4	HD 97585	1.2 × 4	5.37	5.40
J1215+0042	2018 Apr 03	ARCoIRIS	1.26	240 × 4	HD 111744	8 × 4	8.86	8.84
J1252+0347	2018 Apr 03	ARCoIRIS	1.21	300 × 4	HD 97585	1.2 × 4	5.37	5.40
J1307+0246	2018 Apr 03	ARCoIRIS	1.01	180 × 4	HD 109309	2 × 4	5.43	5.47
J1452+0931	2018 Apr 03	ARCoIRIS	1.30	240 × 4	HD 126129	1.2 × 4	5.03	5.04
J1536+0646	2018 Apr 03	ARCoIRIS	1.27	300 × 4	HD 140775	1.2 × 4	5.60	5.58
J1628–4652	2018 Apr 03	ARCoIRIS	1.04	300 × 4	HD 146802	10 × 4	8.88	8.81
J1700–4048	2018 Apr 03	ARCoIRIS	1.03	300 × 4	HD 151681	8 × 4	8.46	8.32
J0948+5300	2018 June 16	SpeX SXD	1.20	299.8 × 8	HD 92245	19.92 × 6	6.02	6.05
J1150–2914	2018 June 16	SpeX SXD	1.57	299.8 × 8	HD 110443	9.730 × 8	9.51	9.34
J1250+0455	2018 June 16	SpeX SXD	1.04	299.8 × 8	HD 111744	19.92 × 8	8.86	8.81
J1441+4217	2018 June 16	SpeX SXD	1.09	299.8 × 6	HD 111744	19.92 × 8	8.86	8.81
J1143+5324	2018 June 17	SpeX Prism	1.20	1.9 × 8	HD 99966	1.853 × 8	7.33	7.39
J0508+3319	2020 Mar 04	SpeX SXD	1.06	119.5 × 8	HD 35076	9.730 × 4	6.37	3.44
J0723+4622	2020 Mar 24	SpeX SXD	1.12	299.8 × 8	HD 66824	4.634 × 4	6.30	6.33
J0811+1855	2020 Mar 24	SpeX SXD	1.00	119.5 × 8	HD 74721	9.730 × 4	8.76	8.70
J0916–1121	2020 Mar 24	SpeX SXD	1.17	239.6 × 4	HD 73687	4.634 × 4	6.66	6.64
J0942–2551	2020 Mar 24	SpeX SXD	1.43	299.8 × 16	HD 98949	9.730 × 2	7.51	7.52
J1126–2706	2020 Mar 24	SpeX SXD	1.47	239.6 × 8	HD 98949	9.730 × 2	7.51	7.52
J1152+5901	2020 Mar 24	SpeX SXD	1.29	299.8 × 12	HD 73687	9.730 × 2	6.66	6.64
J1320+4238	2020 June 28	SpeX SXD	1.09	359.6 × 4	HD 128039	19.92 × 4	9.50	9.28
J1423+5146	2020 June 28	SpeX SXD	1.18	299.8 × 4	HD 128998	4.634 × 4	5.82	5.82
J1544+3301	2020 June 28	SpeX SXD	1.07	299.6 × 4	HD 158261	4.634 × 4	5.93	5.93
J1654–3819	2020 June 28	SpeX SXD	1.92	299.8 × 4	HD 154056	9.730 × 4	9.21	9.07
J1713–3952	2020 June 28	SpeX SXD	1.98	299.8 × 4	HD 162620	4.634 × 4	11.02	9.71
J0808+3157	2021 Jan 02	SpeX SXD	1.02	359.6 × 4	HD 71906	9.730 × 4	6.13	6.17
J0900+5205	2021 Jan 02	SpeX SXD	1.18	359.6 × 8	HD 83869	9.730 × 4	6.36	6.35
J0911+1432	2021 Jan 02	SpeX SXD	1.02	359.6 × 10	HD 80613	9.730 × 4	6.55	6.55
J1315+3232	2021 Jan 02	SpeX SXD	1.05	359.6 × 6	HD 121781	9.730 × 4	9.04	8.94
J0515+0613	2021 Feb 01	SpeX SXD	1.05	359.6 × 8	HD 40814	9.730 × 4	9.11	9.04
J0542+0041	2021 Feb 01	SpeX SXD	1.14	359.6 × 8	HD 45357	9.730 × 4	6.71	6.68
J0832+3538	2021 Feb 21	SpeX Prism	1.04	119.5 × 6	HD 82191	4.634 × 6	6.70	6.62
J0850–0318	2021 Feb 21	SpeX Prism	1.09	179.8 × 12	HD 83535	4.634 × 6	7.34	7.21
J0941+3315A	2021 Feb 21	SpeX SXD	1.03	299.8 × 6	HD 89239	9.730 × 6	6.50	6.52
J1158+3817	2021 Feb 21	SpeX SXD	1.07	299.8 × 8	HD 109615	9.730 × 4	7.25	7.28
J1243+6001	2021 Feb 01	SpeX Prism	1.57	179.8 × 28	HD 116405	9.730 × 20	8.27	8.32
J1313+1404	2021 Feb 21	SpeX SXD	1.01	299.8 × 10	HD 121880	9.730 × 4	7.65	7.58
J1420+3235	2021 Feb 21	SpeX SXD	1.02	299.8 × 4	HD 127067	29.65 × 4	7.10	7.11
J1514+3547	2021 Feb 21	SpeX SXD	1.04	299.8 × 8	HD 128039	19.92 × 4	9.50	9.28
J1544–0435	2021 Apr 08	SpeX Prism	1.10	119.5 × 8	HD 148573	9.730 × 8	9.50	9.28
J1637+1813	2021 Apr 08	SpeX Prism	1.01	119.5 × 8	HD 156653	9.730 × 8	6.00	5.99
J1646–2115	2021 Apr 08	SpeX Prism	1.33	119.5 × 8	HD 157734	9.730 × 8	9.18	8.97
J1737+4705	2021 Apr 08	SpeX SXD	1.13	299.8 × 12	HD 174366	9.730 × 12	6.76	6.71
J1847–3419	2021 June 03	SpeX SXD	1.72	299.8 × 8	HD 182985	19.92 × 6	7.58	7.46
J1938+4321	2021 June 03	SpeX SXD	1.11	299.8 × 6	HD 193594	19.92 × 6	7.80	7.78
J2019+2256	2021 June 03	SpeX Prism	1.04	149.7 × 6	HD 201671	0.463 × 8	6.67	6.65

^a – *B* and *V* magnitudes are taken from the Tycho-2 catalogue of Høg et al. (2000).

observed when observing conditions were too poor to allow for UCD observations (e.g. too much cloud). Most of the observations of non-UCD targets were made using the prism configuration of the IRTF SpeX instrument, and only one of the non-UCDs was observed using the ARCoIRIS instrument at Blanco in Chile. Details of the observations made of the non-UCDs can be seen in Table B2. As with the UCDs, the non-UCDs spectra were reduced with SPExTOOL.

B2 Spectral Classification

B2.1 Spectroscopic Classification using SPLAT

SPLAT can only classify the spectra of UCDs, so any non-UCDs cannot be classified with high confidence. Classification using SPLAT is carried out for sake of consistency and to give an indication of the strength of using SPLAT to classify objects outside the realm of

UCDs. Again, both the Kirkpatrick method (Kirkpatrick et al. 2010) and the whole spectrum are used for classification (Table B1).

B2.2 Photometric Classification

As with the UCDs, the photometric classification method outlined by Skrzypek et al. 2015 can be used to determine photometric spectral types. Making use of a template derived using the same photometric bands as for the UCDs (but instead for K and M-type non-UCDs, rather than UCDs), the non-UCDs can be classified photometrically. Table B1 shows the photometric spectral classifications for the non-UCDs. Since SPLAT can only accurately classify UCDs, the photometric classifications are adopted for the non-UCDs.

B2.3 Comparison of Spectroscopic and Photometric Spectral Types

Comparing the spectroscopic and photometric spectral types can give an indication of the strength of SPLAT for classifying non-UCDs. Overall, we can see that the non-UCD spectral types given by SPLAT tend to agree for within ± 2.0 subtypes the objects with M-type photometric classifications; however, since M0 is the earliest spectral type that SPLAT can classify, the non-UCDs with K-type photometric classifications have vastly different spectroscopic classifications given by SPLAT.

B3 Spectral Analysis

B3.1 Spectral Plots

Fig. B1 shows the stacked spectral plots for the non-UCDs. Since these observations were made when conditions were too poor for the UCDs of interest to be observed, most of the objects were observed with the SpeX Prism configuration. Objects marked with a dagger † in Fig. B1 are those observed with SpeX Prism, those marked with a double dagger ‡ are observed with SpeX SXD, and those marked with an asterisk * are observed with ARCoIRIS. As would be expected with observations of brighter objects, these spectra have better signal-to-noise than those of the UCDs even though the observing conditions were poor, resulting in clearer spectral plots. The shapes of the spectra follow the expected progression of spectral types K through M, and any spectra with features which appear unusual (such as those seen in J1103+3558) are due to differences in resolution of the instruments used to obtain the spectra.

B4 Colour-Magnitude Diagrams

As is the case for the UCDs, we can plot CMDs for the non-UCDs (Fig. B2). It is clear from these plots that none of the non-UCDs have unusual colours relative to their brightness, although there is no clear relation between spectral type and position on the CMD. Two of the non-UCDs (J1128+4933 and J1154+3708) are obviously giant stars, lying far above the main sequence on the giant branch of the CMD.

APPENDIX C: CREATING THE TEMPLATE FOR PHOTOMETRIC CLASSIFICATION

We created a template of 2MASS J , H and K_s , and CatWISE2020 $W1$ and $W2$ magnitudes using the lists of UCDs from Gagné & Best (2014a) and Gagné & Best (2014b). Plotting the magnitudes for each of the UCDs in these lists against their spectral types and

fitting a polynomial to each magnitude-spectral type relation allows use to create our magnitude template (Table C1). The χ^2 values for each object are in the same way as outlined by Skrzypek et al. (2015), and the spectral type corresponding to the smallest χ^2 value is determined to be the best-fitting photometric spectral type.

APPENDIX D: FULL SAMPLE DATA

Table D1 shows the collated data for the full sample of UCDs presented in this work. A machine-readable version of this table is available in its entirety from CDS.

This paper has been typeset from a $\text{\TeX}/\text{\LaTeX}$ file prepared by the author.

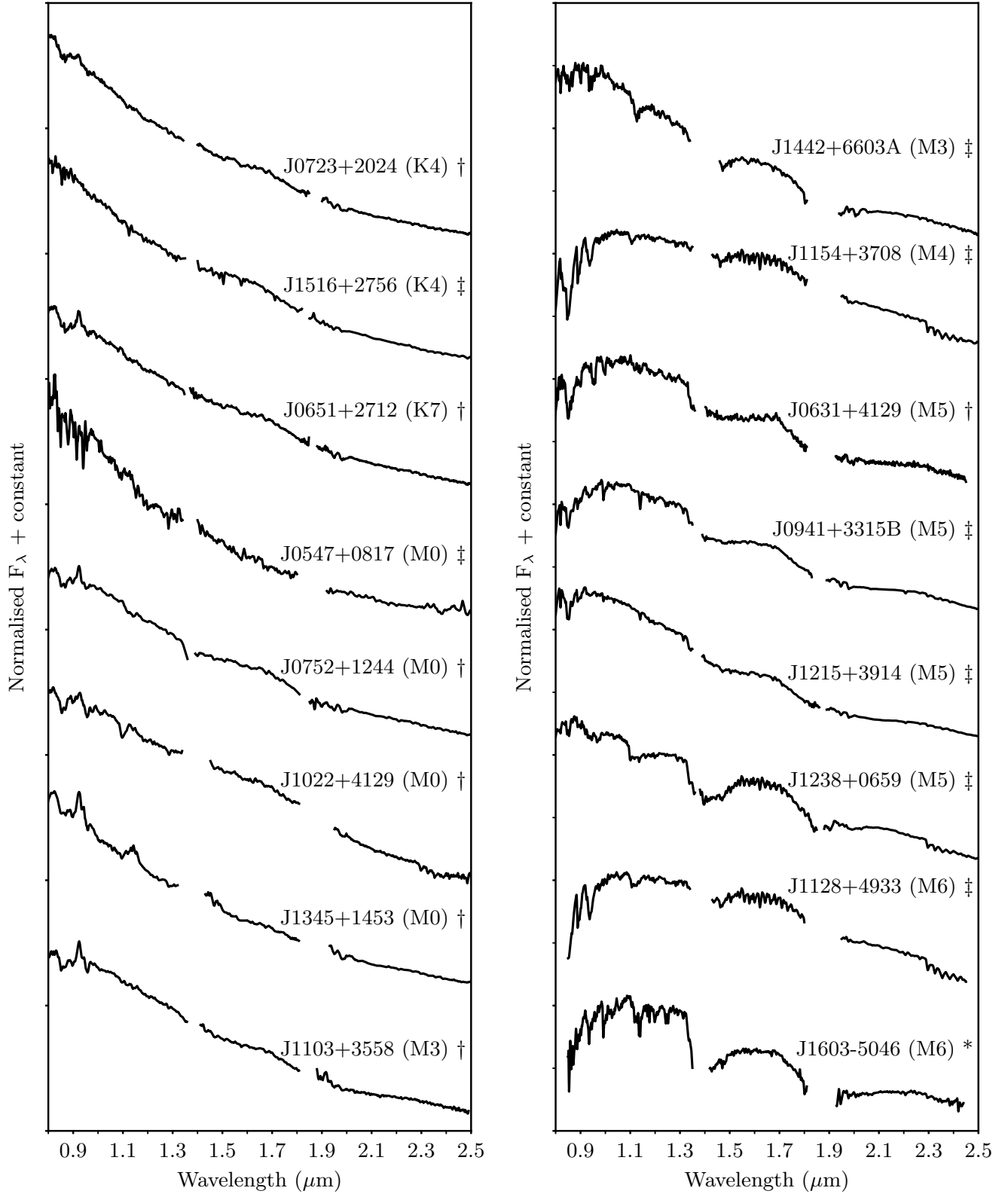


Figure B1. Stacked spectral plot of the non-UCDs observed, sorted by spectral type – left: K3.5–K4.5, right: K8–M6.5. Each spectrum is normalised at $1.27 \mu\text{m}$ and vertically offset by equal flux increments. Noisy areas around the H_2O bands at $\sim 1.3 \mu\text{m}$ and $\sim 1.9 \mu\text{m}$ have been removed to make plots clearer. Objects marked with a dagger † are those observed with SpeX Prism, those marked with a double dagger ‡ are observed with SpeX SXD, and those marked with an asterisk * are observed with ARCoIRIS.

Table B1. Basic data for each of the non-UCD objects in this paper. Spectroscopic classifications (SpT) of the objects are as given by SPLAT, and photometric spectral types (PhT) are also shown. Where applicable, published classifications for each object are also shown. Objects marked with a dagger † are those observed with SpeX Prism, those marked with a double dagger ‡ are observed with SpeX SXD, and those marked with an asterisk * are observed with ARCoIRIS.

Object Short Name	SIMBAD Name	SpT (this work)	PhT (this work)	Published NIR Type	SIMBAD Spectral Type	T _{eff} (K)
J0547+0817	<i>Gaia</i> DR3 3335240017439310464	M0	M0	–	–	3400 ± 270
J0631+4129	LP 205–44	M5	M5	M6 V ^[1]	M5 ^[2]	3500 ± 230
J0651+2712	PM J06518+2712	M0	K7	–	K7e D ^[3]	3500 ± 260
J0723+2024	BD+20 1790	M0	K4	–	K5e D ^[4]	3500 ± 135
J0752+1244	PM J07529+1244	M1	M0	–	M0 ^[5]	3500 ± 315
J0941+3315B	LP 260–43	M5	M5	–	M5 ^[6]	3600 ± 290
J1022+4129	* mu. UMa	M2	M0	–	M0III B ^[7]	3500 ± 110
J1103+3558	HD 95735	M3	M3	–	M2+V B ^[7,a]	3500 ± 95
J1128+4933	V* HP UMa	M7	M5	–	M6 D ^[8]	1700 ± 250
J1154+3708	BD+37 2228	M7	M4	–	M4:III D ^[9]	3500 ± 125
J1215+3914	LP 216–82	M3	M5	–	–	1500 ± 30
J1238+0659	V* R Vir	M4	M5	–	M3.5–7e B ^[10]	3500 ± 190
J1345+1453	HD 119850	M0	M0	–	M2V B ^[7]	3500 ± 145
J1442+6603A	G 239–25	M1	M3	–	M3V C ^[8]	3500 ± 260
J1516+2756	<i>Gaia</i> DR2 1271645228286891008	M0	K4	–	–	3500 ± 25
J1603–5046	<i>Gaia</i> DR3 5981801923255812608	M7	M6	–	–	1500 ± 20

References. ^[1] – Newton et al. (2014) ^[2] – Reid et al. (1995) ^[3] – Bowler et al. (2019) ^[4] – Reid et al. (2004)
^[5] – Lépine & Gaidos (2011) ^[6] – Mason et al. (2001) ^[7] – Keenan & McNeil (1989) ^[8] – Stephenson (1986)
^[9] – Skiff (2008) ^[10] – Keenan et al. (1974)

Notes. ^[a] – The + symbol is used by Keenan & McNeil (1989) to indicate a quarter sub-type (i.e. M2+ is indicative of a spectral type of M2.25).

Table B2. Observation log for the non-UCD observations, showing details of gratings and exposure times for each observation made. The observation date and average airmass of each object are also noted.

Object Short Name	Observation Date (UTC)	Instrument	Average Airmass	Exp Time DIT (s) × NDIT	Telluric Standard	Standard Exp Time DIT (s) × NDIT
J1603–5046	2018 Apr 03	ARCoIRIS	1.07	300 × 4	HD 146802	10 × 4
J1442+6603A	2018 June 16	SpeX SXD	1.63	59.8 × 4	HD 128039	59.77 × 6
J1128+4933	2018 June 17	SpeX SXD	1.22	4.634 × 28	HD 100417	19.92 × 8
J1154+3708	2018 June 17	SpeX SXD	1.08	4.634 × 10	HD 100417	19.92 × 8
J1238+0659	2018 June 17	SpeX SXD	1.07	299.8 × 8	HD 100417	19.92 × 8
J0547+0817	2021 Feb 01	SpeX SXD	1.28	359.6 × 10	HD 46710	9.730 × 4
J0631+4129	2021 Feb 21	SpeX Prism	1.08	9.730 × 6	HD 45105	9.730 × 6
J0651+2712	2021 Feb 21	SpeX Prism	1.01	9.730 × 8	HD 46553	4.634 × 6
J0723+2024	2021 Feb 21	SpeX Prism	1.01	9.730 × 6	HD 62510	9.730 × 8
J0752+1244	2021 Feb 21	SpeX Prism	1.01	9.730 × 8	HD 67959	4.634 × 6
J0941+3315B	2021 Feb 21	SpeX SXD	1.03	299.8 × 6	HD 89239	9.730 × 6
J1215+3914	2021 Feb 21	SpeX SXD	1.06	299.8 × 4	HD 116246	9.730 × 8
J1516+2756	2021 Feb 21	SpeX SXD	1.02	299.8 × 2	HD 127067	29.65 × 4
J1103+3558	2021 May 06	SpeX Prism	1.14	29.7 × 4	HD 103287	29.65 × 4
J1022+4129	2021 June 06	SpeX Prism	1.08	119.5 × 4	HD 103287	29.65 × 4
J1345+1453	2021 June 06	SpeX Prism	1.01	59.8 × 12	HD 130109	29.65 × 8

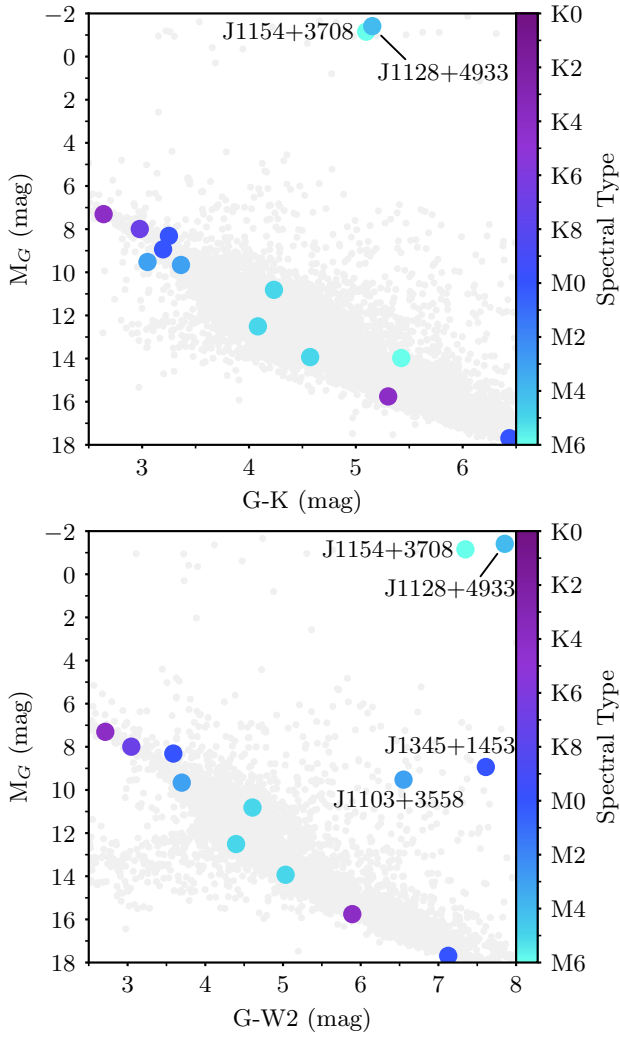


Figure B2. Top: CMD of M_G versus $G-Ks$ for the objects. Bottom: CMD of M_G versus $G-W2$ for the objects. The colour corresponds to the spectral type of the object: purple objects are earlier types and blue objects are later types. Median uncertainties are too small to plot. Grey points are objects from the GUCDS Master list, showing the expected distribution of UCDs.

Table C1. Template magnitudes used for photometric spectral classification of the UCDs.

Spectral Type	<i>J</i> (mag)	<i>H</i> (mag)	<i>K_s</i> (mag)	<i>W1</i> (mag)	<i>W2</i> (mag)
M6	15.74	14.96	14.48	14.16	13.90
M7	15.76	14.96	14.47	14.13	13.87
M8	15.77	14.97	14.46	14.10	13.84
M9	15.80	14.98	14.46	14.08	13.81
L0	15.82	14.99	14.46	14.07	13.80
L1	15.85	15.01	14.48	14.07	13.78
L2	15.88	15.04	14.49	14.08	13.78
L3	15.91	15.07	14.51	14.10	13.78
L4	15.95	15.10	14.54	14.12	13.78
L5	15.99	15.14	14.57	14.16	13.79
L6	16.03	15.19	14.61	14.20	13.80
L7	16.07	15.24	14.66	14.25	13.83
L8	16.12	15.29	14.71	14.31	13.85
L9	16.17	15.35	14.76	14.39	13.88
T0	16.22	15.42	14.82	14.47	13.92
T1	16.27	15.49	14.89	14.55	13.96
T2	16.33	15.56	14.96	14.65	14.01
T3	16.39	15.64	15.04	14.76	14.06
T4	16.46	15.72	15.12	14.87	14.12
T5	16.52	15.81	15.21	15.00	14.18
T6	16.59	15.91	15.31	15.13	14.25
T7	16.66	16.01	15.41	15.27	14.33
T8	16.74	16.11	15.51	15.42	14.41
T9	16.81	16.22	15.62	15.58	14.49

Table D1. Collated data for all UCDS presented in this work with the first object as an example.

Parameter	Unit	Comment	Example
short_name	–	Object Short Name	J0508+3319
source_id	–	<i>Gaia</i> DR3 Source ID	181724125038647040
ra	deg	Right ascension (ICRS, epoch 2016.0)	77.228
ra_error	mas	Uncertainty	–
dec	deg	Declination (ICRS, epoch 2016.0)	33.32
dec_error	mas	Uncertainty	–
simbad	–	SIMBAD object name	2MASS J05085506+3319272
parallax	mas	<i>Gaia</i> DR3 parallax	53.026
parallax_error	mas	Uncertainty	0.46
distance	pc	Parallax distance from <i>Gaia</i> DR3 parallax	18.9
distance_error	pc	Uncertainty	0.2
spec_distance	pc	Spectrophotometric distance	22.0
spec_distance_error	pc	Uncertainty	1.4
pmra	mas yr ⁻¹	<i>Gaia</i> DR3 proper motion in RA	-215.533
pmra_error	mas yr ⁻¹	Uncertainty	0.634594
pmdec	mas yr ⁻¹	<i>Gaia</i> DR3 proper motion in dec	-617.068
pmdec_error	mas yr ⁻¹	Uncertainty	0.427902
spt	–	Spectroscopic spectral classification	L2
spt_error	–	Uncertainty	0.5
spt_published	–	Spectroscopic spectral classification from literature	L2
spt_refname	–	ADS bibcode for SpT	2016ApJS...224...36K
pht	–	Photometric spectral classification	L1
pht_error	–	Uncertainty	2.5
pht_published	–	Photometric spectral classification from literature	–
pht_refname	–	ADS bibcode for PhT	–
vtan	km s ⁻¹	Tangential velocity	58.4276
vtan_error	km s ⁻¹	Uncertainty	0.5122
rv	km s ⁻¹	Radial velocity	53.0
rv_error	km s ⁻¹	Uncertainty	13.6
rv_published	km s ⁻¹	Radial velocity from literature	–
rv_refname	–	ADS bibcode for radial velocity	–
u	km s ⁻¹	Space velocity U-component	-81.2
v	km s ⁻¹	Space velocity V-component	-21.8
w	km s ⁻¹	Space velocity W-component	-53.9
teff	K	Effective temperature	2000
teff_error	K	Uncertainty	60
ruwe	–	<i>Gaia</i> DR3 re-normalised unit weight error value	1.0803
companion	–	<i>Gaia</i> DR3 source ID of wide companion object	–
banyan	–	BANYAN Σ young moving group	–
banyan_prob	–	Probability of group membership	–
gravity	–	Surface gravity classification	FLD-G
notes	–	Young, thick disc, binary	Thick disc
jmag_2mass	mag	2MASS J-band magnitude	14.217
jmag_2mass_error	mag	Uncertainty	0.032
hmag_2mass	mag	2MASS H-band magnitude	13.242
hmag_2mass_error	mag	Uncertainty	0.037
kmag_2mass	mag	2MASS K-band magnitude	12.623
kmag_2mass_error	mag	Uncertainty	0.028
w1mag_wise	mag	CatWISE2020 W1-band magnitude	12.133
w1mag_wise_error	mag	Uncertainty	0.015
w2mag_wise	mag	CatWISE2020 W2-band magnitude	11.899
w2mag_wise_error	mag	Uncertainty	0.014
gmag_gaia	mag	<i>Gaia</i> DR3 G-band magnitude	19.141
gmag_gaia_error	mag	Uncertainty	0.003
mg	mag	<i>Gaia</i> DR3 G-band absolute magnitude	17.763
mg_error	mag	Uncertainty	0.019